Delia Maria Fugger, BSc

Transport in low dimensional topological open quantum systems

MASTER'S THESIS

to achieve the university degree of

Diplom-Ingenieurin

Master's degree programme: Technical Physics

submitted to

Graz University of Technology

Supervisor

Univ.-Prof. Dr.rer.nat. Enrico Arrigoni

Institute of Theoretical and Computational Physics

Graz, January 2016

AFFIDAVIT

I declare that I have authored this thesis independently, that I have not used other than the declared sources/resources, and that I have explicitly indicated all material which has been quoted either literally or by content from the sources used. The text document uploaded to TUGRAZonline is identical to the present master‘s thesis dissertation.

Date

Signature

Abstract

In this thesis I study the transport properties of non-interacting topological quantum systems, based on the Su-Schrieffer-Heeger Model and the Kitaev Model, out of equilibrium.
These two, the former describing an insulator and the latter a superconductor, are the simplest models, where a topological phase is realized. The Kitaev Model is especially interesting, because it hosts quasiparticle excitations that are Majorana fermions.
The transport properties are evaluated with an auxiliary master equation approach. Therefore the system of interest is connected to two electron reservoirs, either of them modeled by another small quantum system embedded in a Markovian environment. A bias voltage is applied between them driving a current through the system.
In this thesis techniques to determine the dynamics and the non-equilibrium steady state of such a composed system are extended and partly developed anew, based on the preceding work of our working group. Especially the inclusion of superconductivity is an original contribution from this thesis.
The derived techniques are finally applied to a single Su-Schrieffer-Heeger wire, a two-dimensional array of such wires, a Kitaev wire and a wire described by a time-dependent extension of the Kitaev Model. In contrast to the ordinary Kitaev Model, the time-extended one is self-consistently derived from an interacting model without further simplifications and therefore maintains the originally valid conservation laws.

Kurzfassung

In dieser Masterarbeit untersuche ich die Transporteigenschaften von nicht wechselwirkenden topologischen Quantensystemen, basierend auf dem Su-Schrieffer-Heeger Modell und dem Kitaev Modell, im Nichtgleichgewicht.
Diese beiden Modelle, ersteres ein Isolator, letzteres ein Supraleiter, beschreiben die einfachsten Systeme, in denen eine topologische Phase realisiert werden kann. Das Kitaev Modell ist besonders interessant, da dort Majorana Fermionen als Quasiteilchen-Anregungen auftreten.
Die Transporteigenschaften dieser Systeme werden mit Hilfe eines Mastergleichungs-Ansatzes ermittelt. Dazu wird das zu untersuchende System an zwei Elektronenreservoirs gekoppelt, die jeweils durch ein weiteres kleines Quantensystem, eingebettet in ein Markov'sches Bad, modelliert werden. Zwischen ihnen wird eine Spannung angelegt, die einen Strom durch das System treibt.
Im Zuge dieser Masterarbeit werden Methoden zur Bestimmung der Zeitentwicklung und des stationären Zustandes eines solchen zusammengesetzten Systems erweitert und zum Teil neu entwickelt, basierend auf vorangegangenen Arbeiten aus unserer Arbeitsgruppe. Besonders die Berücksichtigung supraleitender Terme stellt einen neuen Beitrag dieser Masterarbeit dar.
Diese Methoden werden schließlich auf einen einzelnen Su-Schrieffer-Heeger Draht, ein zweidimensionales Array aus solchen Drähten, einen Kitaev Draht und einen Draht, der durch eine zeitabhängige Erweiterung des Kitaev Modells beschrieben wird, angewandt. Im Gegensatz zum gewöhnlichen Kitaev Modell, wird dieses zeitabhängige Modell selbstkonsistent und ohne weitere Vereinfachungen von einem wechselwirkenden Modell abgeleitet. Daher bleiben die ursprünglichen Erhaltungssätze in diesem Fall gültig.

Acknowledgements

First of all, I want to thank my supervisor Prof. Enrico Arrigoni for supporting me with his physical expertise, for encouragements and his patience.
Furthermore I want to thank Antonius Dorda and Martin Nuss for many fruitful discussions and also Gerhard Dorn, Max Sorantin and Markus Aichhorn for their help on open questions.

Preliminary remarks

Throughout this thesis I have used natural units, the reduced Planck constant $\hbar$, the elementary charge e and the Boltzmann constant k_B are set equal to one.
Regarding the notation, vectors and matrices are set in boldface type, operators - except for creation and annihilation operators - are written with a hat and superoperators with a double hat.

Contents

1 Introduction

Before the discovery of the quantum Hall effect [1], phases of matter were uniquely defined, according to Landau, in terms of the symmetries they spontaneously break. In a liquid-to-solid transition, for instance, the translational symmetry is broken, in a paramagnetic-to-ferromagnetic transition the rotational symmetry.
Then K. von Klitzing et al. found out that a two-dimensional electron gas in a strong perpendicular magnetic field shows a current that is characterized by a quantized conductance [1]. The conductance quantum is completely determined by physical constants, insensitive to local perturbations and even independent of the material probed (as long as the effect is present). This is known as the quantum Hall effect.
This extraordinary behavior cannot be explained by spontaneous symmetry breaking and it became soon clear that Landau's definition needs further refinement. The quantum Hall effect was explained two years after its discovery [2]. It turned out that a topological quantum number can be defined for the bulk of the system, which determines the conductance of its boundaries. This quantum number is associated with a phase and its change is accompanied by a change of phase. Furthermore, in order for the effect to occur, the bulk has to show an energy gap and this gap closes at the transition points.
Having investigated this interesting new state of matter, the research went on with the aim to find other topological phases and to find out, whether materials exist that intrinsically show topological behavior, without the presence of a magnetic field or other external parameters. The first topological insulator was introduced by C.L. Kane and E.J. Mele in 2005 [3], more than two decades after the discovery of the quantum Hall state. Ever since many systems could be identified to have topologically non-trivial properties [4, 5]. Generally, in topological insulators the phases can be labelled by a set of topological quantum numbers. The systems have a bulk energy gap that closes at the transition points between phases and some phases are associated with topologically protected gapless boundary states.
Superconductors also have a gapped energy spectrum and can show a topological phase. In topological superconductors exotic quasiparticle excitations arise at the boundaries, namely spatially isolated Majorana fermions. These have been originally introduced in the context of high-energy physics by E. Majorana [6]. They are especially interesting, because they are non-Abelian anyons [7]. That is, they obey special (anti-)commutation rules, which are neither bosonic nor fermionic. Therefore particle exchanges are non-trivial operations that can change the state of the system fundamentally. Spatially isolated Majorana fermions have been proposed as information carriers for quantum computing, see sec. 3.2.1.
In topological phases of matter the transport properties of the arising boundary states are of particular interest. Within this thesis I investigate systems based on the Su-Schrieffer-Heeger Model and the Kitaev Model out of equilibrium. These two, describing an insulator and a superconductor, respectively, are the simplest models, where a topological phase can be realized. In order to study the systems' transport properties, they are connected to two leads and a bias voltage is applied driving a current. They are, therefore, described as open quantum systems coupled to reservoirs. This thesis presents and partly develops techniques to theoretically deal with such open systems.
Specifically, sec. 2 of this thesis provides an introduction into the treatment of open quantum systems. Most importantly, in sec. 2.2.1 the Lindblad quantum master equation is introduced, which I used, in order to model the open systems' dynamics. In sec. 2.3 the superfermion representation is presented, which enables us to treat an open system similar to a closed one. This section contains a summary of established results, taken from [8] and [9] .

In sec. 3 the basic models studied in this thesis are introduced, the Su-Schrieffer-Heeger Model, sec. 3.1, and the Kitaev Model, sec. 3.2. There is also a part about Majorana fermions and applications, sec. 3.2.1, where their potential for quantum computing is highlighted, and a part about the physical realization of the Kitaev Model, sec. 3.2.2, since it does not occur naturally. The information for this section was also taken from the literature. I did the calculations to show the properties of the bulk and the boundaries anew, in order to present them differently and in some more detail than the used literature.
In sec. 4 the generic solution of the Lindblad equation for a system of non-interacting fermions is presented. In sec. 4.1 the Liouvillian, the generator of this equation, is determined for an ordinary non-interacting system and for a generalized one that includes superconducting (BCS) pairing terms. The generator is further rephrased, in order to simplify the task of solving the Lindblad equation. In sec. 4.2 the time evolution of the system is determined with two different methods, one of them based on the diagonalization of the Liouvillian. In sec. 4.3 the steady state of the system is evaluated, following roughly the ideas in [10]. In this paper similar calculations are performed for an ordinary non-interacting system without BCS pairing. I adapted some of the results, as marked at the respective positions. The rest of the calculations in sec. 4, especially all calculations for the superconducting system, are original contributions from this thesis. The system including BCS pairing is far more complicated to handle and some non-trivial proofs are necessary to determine the dynamics and the steady state via diagonalization. These calculations are partly long and based upon another. For a better reading they were transferred to the Appendix, sec. 7, which also constitutes an original contribution of the present thesis.
Sec. 5 contains the results of the calculations. In sec. 5.2 a model for the leads is presented and a scheme to apply a bias voltage between them, following the articles [9, 10]. In sec. 5.3 the Su-Schrieffer-Heeger Model is studied and in sec. 5.5 the Kitaev Model. Furthermore a two-dimensional extension of the Su-Schrieffer-Heeger Model is examined, sec. 5.4. At the end of this section a time dependent extension of the Kitaev Model is introduced and investigated, sec. 5.6. This part contains probably the most interesting results of the present thesis. I have written all programs to solve the Lindblad equation and produce these results on my own, using Matlab and the provided functions by Matlab.
In sec. 6 the main results are summarized and discussed.

2 Open quantum systems

In this thesis I study the transport properties of topological systems. For this purpose they are coupled to two leads and a bias voltage is applied. The systems are open then. This section provides an introduction into the treatment of open quantum systems. It starts with a brief review about closed systems, sec. 2.1, followed by some general remarks about open systems, sec. 2.2. Then the Lindblad quantum master equation is presented, which can be used to describe the systems' dynamics and which I applied in this thesis. Sec. 2.1 and 2.2 follow closely [8], according information can also be found in many other introductory books. In sec. 2.3 the superfermion representation is introduced, according to [9], which allows to treat an open system analogously to a closed one. It is used to solve the Lindblad quantum master equation in this thesis.

2.1 Review on closed systems

Pure states: A closed quantum system in a pure state can be described in terms of its state vector $|\psi(t)\rangle$, whose dynamics is governed by the Schrödinger equation,

$$i\,\frac{d}{dt}\,|\psi(t)\rangle = \hat{H}\,|\psi(t)\rangle \ , \tag{1}$$

where $\hat{H}$ denotes the hamiltonian of the system. The solution to this equation is a unitary propagation of the state vector in time, according to

$$|\psi(t)\rangle = \hat{U}(t,t_0)\,|\psi(t_0)\rangle \ . \tag{2}$$

$\hat{U}(t,t_0)$ is called time evolution operator. It maps the system from its initial state at time t_0 to its final state at time t and is defined as

$$\begin{aligned} \hat{U}(t,t_0) \ &= \hat{T}\exp\left[-i\int_{t_0}^{t} \mathrm{d}\tau\,\hat{H}(\tau)\right] \\ &\overset{\hat{H}\neq\hat{H}(\tau)}{=} \exp\left[-i\,\hat{H}\,(t-t_0)\right] \ . \end{aligned} \tag{3}$$

$\hat{T}$ is the time ordering operator. It rearranges products of operators standing to its right such that their time arguments increase from right to left. If the hamiltonian has no explicit time dependence, the second line of eq. (3) is valid. Since the hamiltonian is hermitian, $\hat{H} = \hat{H}^\dagger$, the time evolution operator is unitary, $\hat{U}^\dagger\hat{U} = \hat{U}\hat{U}^\dagger = \mathbb{1}$.
If the time evolution $|\psi(t)\rangle$ is known, expectation values of system operators $\hat{O}$ can be calculated, according to

$$\langle\hat{O}(t)\rangle = \langle\psi(t)\,|\,\hat{O}\,|\,\psi(t)\rangle \ . \tag{4}$$

Mixed states: In the more general case that the system is initially in a mixed state, described by its density operator $\hat{\rho}(t_0)$, the Liouville - von Neumann equation is valid,

$$i\,\frac{d}{dt}\,\hat{\rho}(t) = [\hat{H},\,\hat{\rho}(t)]\ , \tag{5}$$

where $[\hat{H}, \hat{\rho}]$ denotes the commutator $\hat{H}\hat{\rho} - \hat{\rho}\hat{H}$. Its solution is calculated with the same propagator as the pure state solution, given in eq. (3),

$$\hat{\rho}(t) = \hat{U}(t, t_0)\, \hat{\rho}(t_0)\, \hat{U}^{\dagger}(t, t_0)\ . \tag{6}$$

The Liouville - von Neumann equation can also be expressed as

$$i\,\frac{d}{dt}\,\hat{\rho}(t) = \hat{\hat{L}}\,\hat{\rho}(t)\ . \tag{7}$$

$\hat{\hat{L}}$ is called Liouvillian or Liouville superoperator. It is defined by its action as $\hat{\hat{L}}\hat{\rho} = [\hat{H}, \hat{\rho}]$. The term superoperator arises, because it acts on an operator, instead of a state vector, and the result of this action is another operator. The solution to eq. (7) is determined as

$$\hat{\rho}(t) = \hat{\hat{U}}(t, t_0)\,\hat{\rho}(t_0)\ , \tag{8}$$

with the time evolution superoperator $\hat{\hat{U}}$,

$$\begin{aligned} \hat{\hat{U}}(t, t_0) \ &= \hat{\hat{T}}\exp\left[-i\int_{t_0}^{t} \mathrm{d}\tau\, \hat{\hat{L}}(\tau)\right] \\ &\overset{\hat{\hat{L}}\neq\hat{\hat{L}}(\tau)}{=} \exp\left[-i\,\hat{\hat{L}}\,(t - t_0)\right]\ . \end{aligned} \tag{9}$$

Its application to the density operator, $\hat{\hat{U}}\,\hat{\rho}$, is equivalent to $\hat{U}\,\hat{\rho}\,\hat{U}^{\dagger}$, which can be seen by comparison of eq. (8) with (6). As its ordinary counterpart, the time evolution superoperator is unitary, $\hat{\hat{U}}^{\dagger}\hat{\hat{U}} = \hat{\hat{U}}\hat{\hat{U}}^{\dagger} = \mathbb{1}$, since the Liouvillian of a closed system is hermitian, $\hat{\hat{L}} = \hat{\hat{L}}^{\dagger}$.
The set of equations (7) - (9) formally look the same as the equations (1) - (3), except for the fact that the former deal with superoperators instead of ordinary operators, acting on operators instead of state vectors.
Expectation values of system operators $\hat{O}$ in dependence of time are determined by

$$\langle \hat{O}(t) \rangle = \mathrm{tr}\,\left\{\hat{\rho}(t)\hat{O}\right\}\ . \tag{10}$$

2.2 Open systems

An open quantum system is a quantum system that is coupled to its surrounding environment. Depending on the nature of the coupling, the environment exerts influence on the system's dynamics. Under certain mathematical conditions it is possible to obtain the dynamics of an open quantum system from a master equation. This is a first order differential equation for the reduced density operator of the system. Within this equation the density operator changes due to the action of other system operators, with coefficients determined by the coupling to the environment.
A master equation can be thought of as being derived from the evolution equation of a universal closed system, involving the system of interest and its environment, by taking the partial trace over the environment's degrees of freedom. This procedure can also be applied to the solution of the universal evolution equation, yielding the solution to the master equation, as sketched in the diagram (11), adapted from [8].

In (11) $\hat{\rho}_u$, $\hat{\rho}$ and $\hat{\rho}_e$ are the density operators of the universe, the system and its environment, respectively. It has been assumed that the initial state of the universe factorizes and that the state of the environment is independent of time. The latter is plausible, if the environment is much larger than the system and thus its state only marginally affected by the coupling.

$$\begin{array}{ccc} \hat{\rho}_u(t_0) = \hat{\rho}(t_0) \otimes \hat{\rho}_e & \xrightarrow{\text{unitary evolution}} & \hat{\rho}_u(t) = \hat{\hat{U}}_u(t, t_0)\,[\hat{\rho}(t_0) \otimes \hat{\rho}_e] \\ \Big\downarrow \mathrm{tr}_e & & \Big\downarrow \mathrm{tr}_e \\ \hat{\rho}(t_0) & \xrightarrow[\text{map}]{} & \hat{\rho}(t) = \hat{\hat{U}}(t, t_0)\,\hat{\rho}(t_0) \end{array} \tag{11}$$

The superoperators $\hat{\hat{U}}_u$ and $\hat{\hat{U}}$ describe the propagation of the universe and the system. They yield the solutions to the universal evolution equation and the master equation, respectively. Since the universe is closed, eq. (5) - (10) apply and it evolves unitarily in time. This does not hold for the system, as highlighted in sec. 2.2.1. In general a derivation like this cannot be exercised in practice. Therefore a master equation is usually an approximation.

2.2.1 The Lindblad quantum master equation

Within this thesis I work with the Lindblad quantum master equation. It has the following structure,

$$i\,\frac{d}{dt}\,\hat{\rho}(t) = [\hat{H}, \hat{\rho}(t)] + i \sum_{ij} \gamma_{ij} \left[2\,\hat{M}_i\,\hat{\rho}(t)\,\hat{M}_j^\dagger - \left\{ \hat{M}_j^\dagger \hat{M}_i\,,\, \hat{\rho}(t) \right\} \right] , \tag{12}$$

$\hat{\rho}$ is the reduced density operator of the system, describing its quantum state. $\hat{H}$ is a hermitian operator that acts as effective hamiltonian. It includes the free hamiltonian of the system, if it were closed, and potentially additional terms, due to the coupling to the environment. The operators $\hat{M}_i$ are called Lindblad operators. They are also system operators, but in general not hermitian. Their actual manifestation depends on the environment and the nature of the coupling to it. This also holds for the coefficient matrix $\boldsymbol{\gamma}$, which is hermitian and positive semidefinite. The expression $\{\hat{M}_j^\dagger \hat{M}_i\,,\, \hat{\rho}\} = \hat{M}_j^\dagger \hat{M}_i\,\hat{\rho} + \hat{\rho}\,\hat{M}_j^\dagger \hat{M}_i$ means the anticommutator. In summary, the quantities in eq. (12) have the following properties,

$$\hat{H} = \hat{H}^\dagger\,, \tag{13}$$

$$\boldsymbol{\gamma} = \boldsymbol{\gamma}^\dagger\,, \tag{14}$$

$$\boldsymbol{v}^\dagger \boldsymbol{\gamma} \boldsymbol{v} \geq 0 \quad \text{for all vectors } \boldsymbol{v}\,. \tag{15}$$

The Lindblad master equation is the most general master equation that may be obtained featuring the properties that it is local in time, has constant coefficients and preserves the interpretation of $\hat{\rho}$ as a density operator. The last condition means that $\hat{\rho}$ keeps its defining qualities as a density operator during the time evolution, a proper initialization provided. These qualities are hermiticity, normalization and positive semidefiniteness,

$$\hat{\rho} = \hat{\rho}^\dagger\,, \tag{16}$$

$$\mathrm{tr}\{\hat{\rho}\} = 1\,, \tag{17}$$

$$\langle\psi|\,\hat{\rho}\,|\psi\rangle \geq 0 \quad \text{for all vectors } |\psi\rangle\,. \tag{18}$$

The first condition implies that the future state of the system $\hat{\rho}(t + dt)$ is solely dependent on its present state $\hat{\rho}(t)$ and other quantities in the master equation. There is no additional information encoded in the system's past, hence there is no memory effect.
The Lindblad master equation can be rewritten in terms of a Liouville superoperator, analogue to the Liouville - von Neumann equation (5), and also resulting in eq. (7). Its solution is then given by the set of equations (8) to (10), but with a different Liouvillian,

$$\hat{\hat{L}} = \hat{\hat{L}}_H + \hat{\hat{L}}_D \,, \tag{19}$$

$$\hat{\hat{L}}_H \, \hat{\rho}(t) = [\hat{H}, \, \hat{\rho}(t)] \,, \tag{20}$$

$$\hat{\hat{L}}_D \, \hat{\rho}(t) = i \sum_{ij} \gamma_{ij} \left[2 \, \hat{M}_i \hat{\rho}(t) \, \hat{M}_j^\dagger - \left\{ \hat{M}_j^\dagger \hat{M}_i \, , \, \hat{\rho}(t) \right\} \right] \,. \tag{21}$$

$\hat{\hat{L}}$ is divided into two parts, depending on its action. The first one, eq. (20), results from the hamiltonian and is marked by the subscript H. It has the same structure as the Liouvillian of a closed system. Therefore it contributes a unitary propagation to the system's dynamics. The second part, eq. (21), has no closed system - analogue. It is not hermitian and therefore generates a non - unitary propagation. As a consequence, the time evolution superoperator, eq. (9), which is calculated from the total Liouvillian, eq. (19), is not unitary. Hence, this part of the Liouvillian accounts for the dissipation in the system and is marked by the subscript D. In summary,

$$\hat{\hat{L}} \neq \hat{\hat{L}}^\dagger \tag{22}$$

$$\hat{\hat{U}}^{-1} \neq \hat{\hat{U}}^\dagger \tag{23}$$

in open systems, whereas in closed systems equalities are valid.

2.3 Superfermion representation

In order to solve the Lindblad quantum master equation, it is beneficial to fully exploit the structural analogies between its superoperator formulation (7), with the Liouvillian (19) - (21), and the Schrödinger equation (1). To this end, eq. (7) is rephrased in an augmented state space. The calculation follows the article [9].

Rephrasing the Lindblad equation: In addition to the Hilbert space of the system, which can be defined by a complete set of orthonormal state vectors $|n\rangle$, a second, identical Hilbert space is introduced, analogously defined by state vectors $|\tilde{n}\rangle$,

$$\sum_n |n\rangle\langle n| = \mathbb{1} \,, \qquad \langle n|m\rangle = \delta_{nm} \,, \tag{24}$$

$$\sum_n |\tilde{n}\rangle\langle \tilde{n}| = \tilde{\mathbb{1}} \,, \qquad \langle \tilde{n}|\tilde{m}\rangle = \delta_{nm} \,. \tag{25}$$

The product space of the original and the additional state spaces can be defined by the vectors $|n\rangle \otimes |\tilde{m}\rangle$. It is furthermore useful to introduce the so - called left vacuum vector $|I\rangle$,

$$|I\rangle = \sum_n |n\rangle \otimes |\tilde{n}\rangle \,. \tag{26}$$

The density operator of the system is defined on the original state space and thus can be represented in terms of the state vectors $|n\rangle$,

$$\hat{\rho}(t) = \sum_{nm} \rho_{nm}(t) \, |n\rangle\langle m| \ , \qquad \rho_{nm}(t) = \langle n| \, \hat{\rho}(t) \, |m\rangle \ . \tag{27}$$

By applying the density operator to the left vacuum, it can be rewritten as a state vector in the augmented state space, according to

$$|\rho(t)\rangle = \hat{\rho}(t) \, |I\rangle \tag{28}$$

$$= \sum_{nm} \rho_{nm}(t) \, |n\rangle \otimes |\tilde{m}\rangle \ . \tag{29}$$

The vector $|\rho(t)\rangle$ is called nonequilibrium wave function. If the whole differential equation (7) is applied to $|I\rangle$, the result is a Schrödinger - like equation for the nonequilibrium wave function,

$$i\frac{d}{dt} \, |\rho(t)\rangle = \hat{L} \, |\rho(t)\rangle \ . \tag{30}$$

$\hat{L}$ is an ordinary operator in the augmented state space, achieved by $\left[\hat{\hat{L}}\hat{\rho}\right] |I\rangle = \hat{L} \, |\rho(t)\rangle$. It is just another representation of the Liouvillian corresponding to the Lindblad equation and therefore not hermitian.
Given the time evolution, expectation values of system operators are calculated within this framework as the following matrix element,

$$\langle \hat{O}(t) \rangle = \langle I \, | \, \hat{O} \, | \rho(t) \rangle \ . \tag{31}$$

The starting point for the considerations above, eq. (7), is a differential equation for an operator changed by a superoperator, whereas the result, eq. (30), describes the change of a state vector, due to an ordinary operator, the same as the Schrödinger equation (1) does, but in an augmented state space and with a non-hermitian generator. This has benefits for the numerical treatment. In a particular basis both generators, $\hat{H}$ and $\hat{L}$, are matrices and can be treated with similar methods.

Eigenstates of the Liouvillian: From the normalization of the density operator (17) follows that $\langle I|\rho(t)\rangle = 1$ is valid at all times. If $\langle I|$ is applied to eq. (30) from the left, it furthermore follows for all times that

$$\langle I| \, \hat{L} = 0 \ . \tag{32}$$

This means that $\langle I|$ is a left eigenvector of $\hat{L}$ to the eigenvalue 0.
If the system is allowed to evolve for some time, it may overcome its transient behavior and reach a steady state, where its density operator does not depend on time anymore. In this case eq. (30) yields

$$\hat{L} \, |\rho_\infty\rangle = 0 \ . \tag{33}$$

$|\rho_\infty\rangle$ denotes the nonequilibrium wave function in the steady state. It is formally reached with $t \to \infty$ and therefore marked by the corresponding subscript. $|\rho_\infty\rangle$ is a right eigenvector of $\hat{L}$ to the eigenvalue 0. So the problem of determining the steady state reduces to the problem of finding this eigenvector of the Liouvillian.

Fermionic multiparticle systems: The systems I study within this thesis are fermionic multiparticle systems. Having to deal with multiparticle systems, the Hilbert space is a Fock space and it is convenient to work in the particle number representation. The state vectors $|n\rangle$ and $|\tilde{n}\rangle$ then correspond to a certain occupation configuration,

$$\begin{aligned} |n\rangle &= |n_1 n_2 \dots n_N\rangle \,, \\ |\tilde{n}\rangle &= |n_1 \widetilde{n_2 \dots n_N}\rangle \,. \end{aligned} \tag{34}$$

n_j denotes the number of particles in the quantum state j, e.g. the j-th site of a lattice. The creation and annihilation operators that add or destroy a particle in state j are called $c_j^\dagger$ and c_j, respectively.

$$\begin{aligned} c_j^\dagger c_j \, |n_1 n_2 \dots n_N\rangle &= n_j \, |n_1 n_2 \dots n_N\rangle \\ \tilde{c}_j^\dagger \tilde{c}_j \, |n_1 \widetilde{n_2 \dots n_N}\rangle &= n_j \, |n_1 \widetilde{n_2 \dots n_N}\rangle \end{aligned} \tag{35}$$

Since these operators are fermionic, they obey the familiar anticommutation relations,

$$\begin{aligned} &\{c_i \,, c_j^\dagger\} = \{\tilde{c}_i \,, \tilde{c}_j^\dagger\} = \delta_{ij} \,, \\ &\{c_i \,, c_j\} = \{c_i^\dagger, c_j^\dagger\} = \{\tilde{c}_i \,, \tilde{c}_j\} = \{\tilde{c}_i^\dagger, \tilde{c}_j^\dagger\} = 0 \,. \end{aligned} \tag{36}$$

Additionally, the anticommutator of operators acting in different Fock spaces is zero. Working with fermions, it is convenient to add a phase to the left vacuum vector. Such a phase does not change the expectation values (31), because it is also contained in $|\rho\rangle = \hat{\rho}\,|I\rangle$. $|I\rangle$ is redefined as

$$\begin{aligned} |I\rangle &= \sum_n \quad (-i)^{S_n} \, |n\rangle \otimes |\tilde{n}\rangle \,, \\ &= \sum_{n_1 n_2 \dots n_N} (-i)^{n_1 + n_2 + \dots + n_N} \, |n_1 n_2 \dots n_N\rangle \otimes |n_1 \widetilde{n_2 \dots n_N}\rangle \,, \end{aligned} \tag{37}$$

where $S_n = n_1 + n_2 + \dots + n_N$ is the total number of particles in the multiparticle state $|n\rangle$. From this representation so-called the tilde conjugation rules can be derived,

$$\begin{aligned} c_j \, |I\rangle &= -i \, \tilde{c}_j^\dagger \, |I\rangle \,, \\ c_j^\dagger \, |I\rangle &= -i \, \tilde{c}_j \, |I\rangle \,. \end{aligned} \tag{38}$$

They represent a useful tool in calculating expectation values, since they allow for a switch between operators in the original and the tilde - state space. By rephrasing the tilde conjugation rules, the left vacuum annihilators, $A_j^\dagger$ and $B_j^\dagger$, can be defined,

$$\begin{aligned} A_j^\dagger &= c_j^\dagger - i\tilde{c}_j \,, \qquad & \langle I| \, A_j^\dagger &= 0 \,, \\ B_j^\dagger &= c_j - i\tilde{c}_j^\dagger \,, \qquad & \langle I| \, B_j^\dagger &= 0 \,. \end{aligned} \tag{39}$$

They obey analogous anticommutation relations to eq. (36),

$$\begin{aligned} &\{A_i \,, A_j^\dagger\} = \{B_i \,, B_j^\dagger\} = \delta_{ij} \\ &\{A_i^{(\dagger)}, A_j^{(\dagger)}\} = \{B_i^{(\dagger)}, B_j^{(\dagger)}\} = \{A_i^{(\dagger)}, B_j^{(\dagger)}\} = 0 \end{aligned} \tag{40}$$

(†) means that the relations hold for operators with and without † likewise.

3 Models

This section presents the basic models studied in this thesis, the Su-Schrieffer-Heeger Model, sec. 3.1, and the Kitaev Model, sec. 3.2. Each subsection starts with a description of the model hamiltonian, followed by a summary of the topological properties. Then the calculations are presented showing these properties. In case of the Kitaev Model, there is also a small part about Majorana fermions and applications, sec. 3.2.1, and one about the physical realization of the model, sec. 3.2.2.

3.1 Su-Schrieffer-Heeger Model

Model: The Su-Schrieffer-Heeger Model describes a one-dimensional topological insulator. It can be used as a simple model for polyacetylene. The alternating single and double bonds are described by an alternating small and big hopping strength, [11]. The hamiltonian for this model reads

$$\hat{H} = \sum_{n=1}^{N} (t+\delta)\, c_{An}^{\dagger} c_{Bn} + \sum_{n=1}^{N-1} (t-\delta)\, c_{An+1}^{\dagger} c_{Bn} + h.c. \tag{41}$$

The operators $c_{\alpha,n}^{\dagger}$ and $c_{\alpha,n}$ create and destroy an electron on site n of the sublattice $\alpha \in \{A, B\}$. All electrons are assumed to have the same spin, redundantizing an extra index. Each unit cell in the system hosts two lattice sites, one of type A and B, respectively. $t+\delta$ denotes the hopping strength between sites within a unit cell and $t-\delta$ is the hopping strength between unit cells. [12, 13]

Properties: The Su-Schrieffer-Heeger Model exhibits a topological phase transition at $|t+\delta| = |t-\delta|$. In the phase $|t+\delta| < |t-\delta|$ the edge sites are weakly bonded and the system forms states at zero energy, which are localized at the edges and decay to zero into the bulk. This phase is the topological phase. If the edge bonds are strong ones, $|t+\delta| > |t-\delta|$, the system is in the trivial phase, where no edge states are present. On both sides of the phase transition the bulk has an energy gap. The gap closes at the transition point $|t+\delta| = |t-\delta|$. The two phases are illustrated in fig. 1. [12, 13]

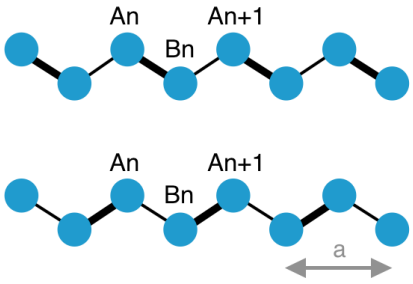

Figure 1: Phases in the Su-Schrieffer-Heeger Model. Upper panel: Trivial phase, $|t+\delta| > |t-\delta|$, strongly bonded edge sites. Lower panel: Topological phase, $|t+\delta| < |t-\delta|$, weakly bonded edge sites, zero - energy edge states arise. a is the size of a unit cell. The illustration has been adapted from [12].

In the next paragraph the bulk properties are shown, the existence of an energy gap and its closing at $|t+\delta| = |t-\delta|$, by imposing periodic boundary conditions. It is followed by a paragraph about open boundaries, where the existence of edge states is demonstrated.

Calculations for the bulk: Following [12], the hamiltonian eq. (41) is periodized by extending the second sum to N and demanding $c_{N+1} = c_1$. Then a discrete Fourier transformation can be applied, according to

$$a_k = \frac{1}{\sqrt{N}} \sum_n e^{-ikna} c_{An} \,, \qquad b_k = \frac{1}{\sqrt{N}} \sum_n e^{-ikna} c_{Bn} \,, \tag{42}$$

and passing the hamiltonian to momentum space,

$$\hat{H} = (t+\delta) \sum_{k\in(-\pi,\pi)} \left(a_k^\dagger b_k + b_k^\dagger a_k\right) + (t-\delta) \sum_{k\in(-\pi,\pi)} \left(e^{-ik} a_k^\dagger b_k + e^{ik} b_k^\dagger a_k\right) . \tag{43}$$

In eq. (43) the lattice constant a has been absorbed into k which is now bounded by $(-\pi, \pi)$. By introducing two component operators $\boldsymbol{\psi}_k$, the hamiltonian can be rewritten as follows,

$$\hat{H} = \sum_k \boldsymbol{\psi}_k^\dagger \boldsymbol{H}_k \boldsymbol{\psi}_k \,, \quad \boldsymbol{H}_k = \begin{pmatrix} 0 & (t+\delta) + (t-\delta)\, e^{-ik} \\ (t+\delta) + (t-\delta)\, e^{ik} & 0 \end{pmatrix} , \quad \boldsymbol{\psi}_k = \begin{pmatrix} a_k \\ b_k \end{pmatrix} . \tag{44}$$

Diagonalizing the coefficient matrix $\boldsymbol{H}_k$ yields the energies

$$E_\pm(k) = \pm \sqrt{2} \sqrt{t^2 + \delta^2 + (t^2 - \delta^2) \cos k} \,. \tag{45}$$

The energy spectrum is symmetric. There are two bands, $E_+(k)$ and $E_-(k)$, separated by an energy gap,

$$\Delta_I = E_+ - E_- = 2E_+ \,. \tag{46}$$

A detailed investigation of eq. (45) yields that the size of the gap at its minima is

$$\begin{aligned} \Delta_{I,min} &= 2\big||t+\delta| - |t-\delta|\big| \,, \\ &= 4 \min\left(|t|, |\delta|\right) . \end{aligned} \tag{47}$$

It depends linearly on the difference in the absolute hopping strengths and closes for $|t+\delta| = |t-\delta|$, which is fulfilled only for $t = 0$ or $\delta = 0$. Fig. 2 shows an example for the energy bands directly

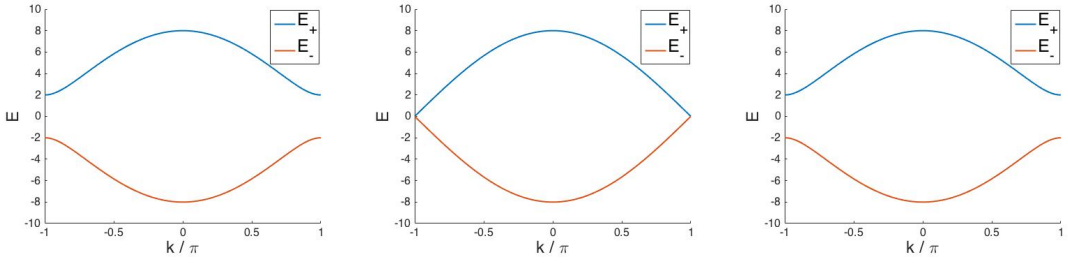

(a) Trivial phase, $t = 4, \delta = 1$. (b) Transition point, $t = 4, \delta = 0$. (c) Topological phase, $t = 4, \delta = -1$.

Figure 2: Energy bands in the Su-Schrieffer-Heeger Model, according to eq. (45). The subfigures show examples for the two phases and the transition point. The size of the energy gap at its minimum is $4|\delta|$.

at and on either side of the gap closing. The bulk properties are the same in both parameter regions, in contrast to the properties of the boundaries, if they are open, which is demonstrated in the following.

Calculations for open boundaries: In case of open boundaries, edge states are present for $|t+\delta| < |t-\delta|$ and missing for $|t+\delta| > |t-\delta|$. In order show this, the special cases $\delta = \pm t$ are examined. Then the adiabatic theorem can be applied to generalize the results to the respective parameter regions, see the next paragraph. [14]

1. $\delta = t \neq 0$

This set of parameters belongs to the trivial phase. Inserting them into the hamiltonian (41) yields

$$\hat{H} = 2t \sum_{n=1}^{N} c_{An}^{\dagger} c_{Bn} + h.c. \tag{48}$$

The unit cells are decoupled from each other, each site is only connected to a single other one. Therefore the hamiltonian is easily diagonalized,

$$\hat{H} = 2t \sum_{n=1}^{N} \sum_{\sigma=\pm 1} \sigma \, d_{\sigma n}^{\dagger} d_{\sigma n} \, , \qquad d_{\sigma n} = \frac{1}{\sqrt{2}} \left(c_{An} + \sigma c_{Bn} \right) . \tag{49}$$

It can be verified that the d - operators are also fermionic. Adding a d - fermion to the system causes an energy change of $\pm 2t$. Therefore the spectrum is gapped, as for periodic boundary conditions, eq. (46). There are no zero - energy edge states.

2. $\delta = -t \neq 0$

For these parameters the system is in the topological phase. The hamiltonian (41) reads

$$\hat{H} = 2t \sum_{n=1}^{N-1} c_{A,n+1}^{\dagger} c_{B,n} + h.c. \tag{50}$$

The sites are connected in pairs, again. In this case the cut is made within the unit cells and not between them. Diagonalizing the hamiltonian yields

$$\hat{H} = 2t \sum_{n=1}^{N-1} \sum_{\sigma=\pm 1} \sigma \, d_{\sigma n}^{\dagger} d_{\sigma n} \, , \qquad d_{\sigma n} = \frac{1}{\sqrt{2}} \left(c_{An+1} + \sigma c_{Bn} \right) . \tag{51}$$

The creation of a d - fermion again changes the energy by $\pm 2t$. Therefore a gap persists also in this case. The gap refers only to the bulk, because the edge sites $A1$ and BN are absent from the hamiltonian (51). Two additional d - fermions can be constructed from them,

$$d_{\sigma N} = \frac{1}{\sqrt{2}} \left(c_{A1} + \sigma c_{BN} \right) . \tag{52}$$

Occupying one of the c or d - states in eq. (52) costs zero energy, since they are missing in the hamiltonian. Eq. (51) can be extended, according to

$$\hat{H} = 2t \sum_{n=1}^{N-1} \sum_{\sigma=\pm 1} \sigma \, d_{\sigma n}^{\dagger} d_{\sigma n} + 0 \sum_{\sigma=\pm 1} d_{\sigma N}^{\dagger} d_{\sigma N} \, . \tag{53}$$

The c_{A1} and c_{BN} - states are the zero - energy edge states. Due to their presence, the ground state of the system is four - fold degenerate. Both edge states can either be occupied or empty without changing the energy of the system.

Application of the adiabatic theorem: The existence of edge states is a property found in certain topological phases. Instead of testing the whole parameter space for this property, the adiabatic theorem can be applied. If the result has been determined for a special case, the whole region in parameter space that can be reached by adiabatically changing the hamiltonian without closing the energy gap and preserving locality also shows this property. The parameter region satisfying this condition belongs to the same phase.
In case of the Su-Schrieffer-Heeger Model and also the Kitaev Model, sec. 3.2, the closing of the bulk gap splits the parameter space in two. Therefore it is sufficient to investigate two special sets of parameters, respectively. They are chosen in a way that makes the calculations especially easy. For both models the requirements of the adiabatic theorem to extend the results to the whole parameter space can be fulfilled, [14]. For general parameters in the topological phase the edge states are not perfectly localized at the ends of the chain but decay exponentially to zero into the bulk. They remain at zero energy as long as their overlap is negligible, otherwise the states split. See [15] for the Su-Schrieffer-Heeger Model, [16] for the Kitaev Model.

3.2 Kitaev Model

Model: The Kitaev Model is a toy model for a one-dimensional spinless p-wave superconductor. It was first introduced by A.Y. Kitaev in 2001 [17]. The hamiltonian describing this model reads

$$\hat{H} = -\mu \sum_{n=1}^{N} c_n^\dagger c_n - \sum_{n=1}^{N-1} \left(t c_n^\dagger c_{n+1} + \Delta c_n c_{n+1} + h.c. \right) . \tag{54}$$

The operators $c_n^\dagger$ and c_n create or annihilate an electron on lattice site n, respectively. The spin index has been dropped, because all electrons have the same spin. μ is the chemical potential, t the nearest neighbor hopping strength and Δ denotes the p-wave pairing amplitude. These parameters are the same for all lattice sites.

Properties: The Kitaev Model shows a topological phase transition at $|\mu| = 2|t|$. For $|\mu| < 2|t|$ it is in the topological phase, where it forms edge states at zero energy that decay into the bulk. These states are spatially isolated Majorana fermions. The phase is furthermore associated with weakly bonded Cooper pairs of infinite size. For $|\mu| > 2|t|$ the system is in the trivial phase, where no edge states arise. In this phase the electrons form strongly bonded, molecule - like Cooper pairs. In both phases the energy spectrum of the bulk has a gap. The gap closes only at the transition point $|\mu| = 2|t|$. [16]
The next paragraph deals with bulk properties, the spectral gap and its closing at $|\mu| = 2|t|$. It is followed by a paragraph about open boundaries, where the existence of edge states is shown. Then comes a part about Majorana fermions and applications, sec. 3.2.1, and another one about the physical realization of the Kitaev model, sec. 3.2.2.

Calculations for the bulk: According to [16], the bulk properties of the system are examined by imposing periodic boundary conditions. Then both sums in eq. (54) run to N and the operators obey $c_{N+1} = c_1$. Performing a discrete Fourier transformation yields

$$\hat{H} = \sum_{k \in (-\pi, \pi)} \left[\xi_k c_k^\dagger c_k - \Delta \left(e^{ik} c_{-k} c_k + e^{-ik} c_k^\dagger c_{-k}^\dagger \right) \right] , \qquad c_k = \frac{1}{\sqrt{N}} \sum_{n=1}^{N} e^{-ikn} c_n , \tag{55}$$

where $\xi_k = -2t\cos k - \mu$ denotes the kinetic energy. For $k = 0$ the hamiltonian is already diagonal in the c operators with energy ξ_0, due to the Pauli exclusion principle. This mode is not very interesting and thus disregarded in the following. Since the other k values lie symmetric to zero, the hamiltonian can be expressed with $k > 0$ only,

$$\hat{H} = \sum_{k>0} \boldsymbol{\psi}_k^\dagger \boldsymbol{H}_k \boldsymbol{\psi}_k + \sum_{k>0} \xi_k \mathbb{1} \,, \qquad \boldsymbol{H}_k = \begin{pmatrix} \xi_k & 2i\Delta \sin k \\ -2i\Delta \sin k & -\xi_k \end{pmatrix} \,, \qquad \boldsymbol{\psi}_k = \begin{pmatrix} c_k \\ c_{-k}^\dagger \end{pmatrix} . \tag{56}$$

This has the advantage of omitting redundancies in the operator basis. The two component operators $\boldsymbol{\psi}_k$ are called Nambu spinors. Diagonalizing the coefficient matrix $\boldsymbol{H}_k$ yields the energies

$$E_\pm(k) = \pm\sqrt{\xi_k^2 + 4\Delta^2 \sin^2 k} \,. \tag{57}$$

The energy spectrum is symmetric, as was the spectrum of the Su-Schrieffer-Heeger model. There is, in general, also a gap between the positive and negative energy branch,

$$\Delta_{sc} = E_+ - E_- = 2E_+ \,. \tag{58}$$

For $\Delta \neq 0$ the gap can only close, if both summands in eq. (57) are zero. This requires $\sin k = 0$, which means either $k = 0$ or $k = \pi$. Summarizing both cases, a closing of the superconducting gap can be observed only at $|\mu| = 2|t|$.

Calculations for open boundaries: Following [17], [16], in order to study the system with open boundaries, eq. (54), the c_n are expressed as the sum of two hermitian operators $\gamma_{\alpha n} = \gamma_{\alpha n}^\dagger$,

$$c_n = \frac{1}{2}\left(\gamma_{Bn} + i\,\gamma_{An}\right) \,, \qquad \begin{aligned} \gamma_{Bn} &= c_n^\dagger + c_n \,, \\ \gamma_{An} &= i\left(c_n^\dagger - c_n\right) \,. \end{aligned} \tag{59}$$

These operators are called Majorana fermion operators. From the fermionic anticommutation relations of c_n and $c_n^\dagger$ follows

$$\left\{\gamma_{\alpha n}\,, \gamma_{\beta m}\right\} = 2\delta_{\alpha\beta}\delta_{nm} \,. \tag{60}$$

Thus they are not fermionic by themselves. They have very interesting properties, whose discussion is delayed to sec. 3.2.1. In terms of the Majorana operators the hamiltonian (54) reads

$$\hat{H} = i\,\mu \sum_{n=1}^{N} \gamma_{An}\gamma_{Bn} - \frac{i}{2}\sum_{n=1}^{N-1}\left[(\Delta - t)\,\gamma_{An}\gamma_{Bn+1} + (\Delta + t)\,\gamma_{Bn}\gamma_{An+1}\right] - \frac{1}{2}\,\mu N \,. \tag{61}$$

In the following two special cases are investigated, one on either side of the gap closing, $|\mu| \lessgtr 2|t|$. The existence of edge states is evaluated, respectively. Then the adiabatic theorem can be applied to generalize the results, as in case of the Su-Schrieffer-Heeger model.

1. $\mu \neq 0$ and $\Delta = t = 0$

For these parameters the system is in the trivial phase. The hamiltonian (54) is already diagonal in the c operators,

$$\hat{H} = -\mu \sum_{n=1}^{N} c_n^\dagger c_n \,. \tag{62}$$

Adding an electron to the system changes the energy by μ. Therefore the spectrum is gapped again. No edge states arise in this case. The ground state of the system is unique and corresponds

to the c - vacuum, $|0_c\rangle$. In the Majorana representation (61) the hamiltonian reads, apart from constants,

$$\hat{H} = i\mu \sum_{n=1}^{N} \gamma_{An}\gamma_{Bn} \ . \tag{63}$$

It couples Majorana operators corresponding to the same lattice site. This case is pictured in the upper panel of fig. 3.

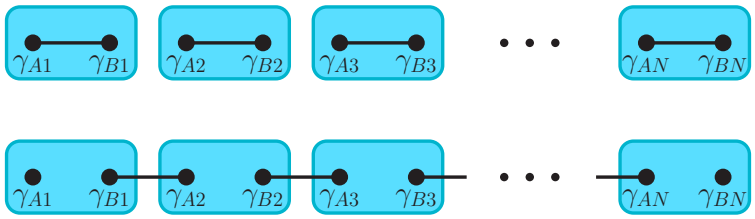

Figure 3: Coupling of Majorana fermions in two special cases, representing the behavior of the Kitaev Model in its two phases. Upper panel: trivial phase with $\mu \neq 0$, $\Delta = t = 0$. Majorana fermions at the same lattice site are coupled. Lower panel: topological phase with $\mu = 0$, $\Delta = t \neq 0$. Coupling of Majorana fermions at adjacent sites. The illustration has been adapted from [18].

2. $\mu = 0$ and $\Delta = t \neq 0$

These parameters drive the system into the topological phase. Inserting them into the hamiltonian (61) and disregarding constants yields

$$\hat{H} = -i\,t \sum_{n=1}^{N-1} \gamma_{Bn}\gamma_{An+1} \ . \tag{64}$$

In this case Majorana operators at adjacent lattice sites are coupled to each other, as illustrated in the lower panel of fig. 3. They can be combined to new operators d_n,

$$d_n = \frac{1}{2}\left(\gamma_{Bn} - i\,\gamma_{An+1}\right) \ , \qquad \begin{aligned} \gamma_{Bn} &= d_n + d_n^\dagger \ , \\ \gamma_{An+1} &= i\left(d_n - d_n^\dagger\right) \ , \end{aligned} \tag{65}$$

which again obey the fermionic anticommutation relations. The new operators diagonalize the hamiltonian (64). Apart from constants, the result is

$$\hat{H} = 2t \sum_{n=1}^{N-1} d_n^\dagger d_n \ . \tag{66}$$

Introducing a d - fermion into the system causes an energy change of $2t$. Therefore a bulk gap persists. The Majorana operators at the edges, γ_{A1} and γ_{BN}, though, are absent from the hamiltonian. They can be combined to a highly non - local fermionic operator,

$$d_N = \frac{1}{2}\left(\gamma_{BN} - i\,\gamma_{A1}\right) \ . \tag{67}$$

Since d_N does not arise in the hamiltonian, the occupation of this state costs zero energy. The underlying Majorana operators refer to the edge states. They also lie at zero energy, but their

occupation is not defined, see sec. 3.2.1. The hamiltonian can be extended by d_N, according to

$$\hat{H} = 2t \sum_{n=1}^{N-1} d_n^\dagger d_n + 0\, d_N^\dagger d_N \,. \tag{68}$$

Due to the zero - energy edge states, the ground state of the system is twofold degenerate. One ground state is the d vacuum $|0_d\rangle$, satisfying $d_N |0_d\rangle = d_n |0_d\rangle = 0 \; \forall n$. The other ground state is given by $d_N^\dagger |0_d\rangle$. They have opposite parity, as the number of fermions they host differs by one.

3.2.1 Majorana fermions and applications

Majorana fermions are particles, which are their own antiparticles [19]. They have been introduced into theoretical physics by E. Majorana in 1937 [6]. Their existence as elementary particles or as quasiparticle exitations has not yet been definitely proven [20] .
Being their own antiparticles, Majorana fermions are created by operators that are hermitian. Two of them can be combined to form a single fermion operator, according to eq. (59). They are not fermions by themselves, because they don't obey the fermionic anticommutation relations, but instead fulfill eq. (60). Therefore $\gamma_{\alpha n}^2 = 1$ is valid, which means that there is no Pauli exclusion principle.
It can be shown that Majorana fermions are non-Abelian anyons [7]. Under exchange of particles the wavefunction does not only pick up a phase, as it is the case with ordinary anyons, fermions and bosons, but the state can change fundamentally. Two exchange operations generally do not commute, therefore the term non-Abelian.
Due to $\gamma_{\alpha n}^2 = 1$ and the hermiticity of these operators, a Majorana fermion state has no well - defined occupation. The relation $\gamma_{\alpha n}^\dagger \gamma_{\alpha n} = 1 = \gamma_{\alpha n} \gamma_{\alpha n}^\dagger$ is always fulfilled. In this sense, the state is always occupied and empty at the same time. It is only possible to measure the occupation of the fermionic state, formed by Majoranas, see also [16, 20].
In the Kitaev model and also in other models for topological superconductors Majorana fermions occur as quasiparticle exitations. If the Kitaev chain is in the topological phase, spatially separated Majorana fermions combine to regular fermions at zero energy. In principle they could be localized arbitrarily far apart from each other [17].
The last two properties make them especially interesting for quantum computing. A qubit could be spanned by the occupation number states of zero-energy fermions, each formed by two spatially isolated Majorana fermions, and it could be changed by exchange of Majorana fermions. In order to perform nontrivial operations, at least four Majorana fermions or two zero energy fermions are required for one qubit. Such exchange processes, called braiding operations, are not sufficient for universal quantum computing, but they could be used in combination with other operation schemes. The advantage of using these special Majorana fermions is that they are localized far from each other and thus form a fermionic state that is robust against local perturbations and separated from the other states by the superconducting gap [17, 20].

3.2.2 Physical realization of the Kitaev model

Superconductors that exhibit a p-wave pairing are extremely rare in nature, see [16]. No naturally occurring system is known that can faithfully be modeled by the Kitaev hamiltonian (54), but it is still possible to engineer such systems.

A common setup to engineer the Kitaev Model involves a semiconducting wire with a strong spin-orbit coupling, a superconducting substrate with s-wave symmetry and a magnetic field, as sketched in fig. 4, see [20, 21, 22].
The engineering method is based on the proximity effect: The wire is coupled to the substrate allowing electrons to tunnel between the two systems. They also feel a pairing potential within the wire, due to the proximity to the bulk superconductor [23, 24, 25]. The pairing symmetry is usually inherited from the superconductor. Thus, if no further modifications are made, it is s-wave in this case. In the following it is highlighted, how the spin-orbit coupling and the magnetic field can be exploited to induce an effective p-wave pairing.

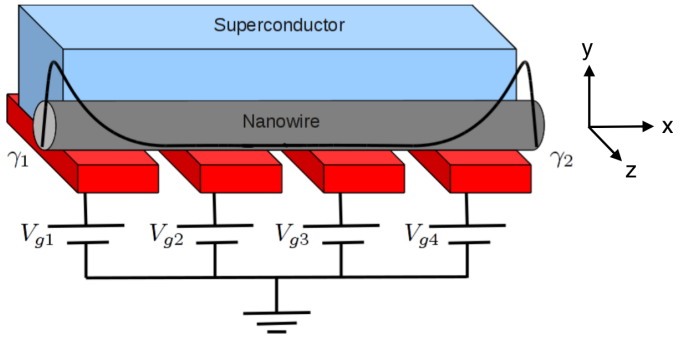

Figure 4: Setup for engineering the Kitaev Model. A nanowire (InAs or InSb) with strong spin-orbit coupling is connected to an s-wave substrate (Nb or Al) and an external magnetic field is applied (missing in the sketch). Effective p-wave pairing can be induced in the wire by the proximity effect, although the substrate has s-wave symmetry. With gate electrodes the chemical potential in the wire can be adjusted, driving it into the topological phase, where Majorana edge states arise. The black curve sketches the decay of the wave functions of the edge states into the bulk. This illustration has been taken from [20] and coordinates have been added.

The initial point of the considerations is a one-dimensional noninteracting wire without further couplings (neither spin-orbit nor proximity) and without magnetic field. One-dimensional means in this case that it has a macroscopic length and therefore the size quantization along its axis is negligible and it is very thin causing the 1D subbands to be nicely separated. The bands have a parabolic form and always two of them, corresponding to the two different spin projections, lie upon another.
If, in addition, spin-orbit coupling is present, the two parabolas are shifted in momentum, depending on the spin polarization in the direction of the spin-orbit field. This is illustrated in fig. 5(a). The different spin orientations are indicated by red arrows. It can be seen that the bands are separated, but there are still two solutions with opposite spin for each energy. Therefore this setup is not yet sufficient to create an effectively spinless regime.
The spin degeneracy can be lifted by application of an external magnetic field with a component perpendicular to the spin-orbit field, see fig. 5(b). A weak magnetic field favors an alignment of spins in parallel or antiparallel to the direction of the field and assigns different energies to electrons depending on their principal alignment. Therefore a gap opens that separates the bands by this measure. If the chemical potential is placed within the gap, which can be accomplished with a number of gate electrodes along the wire, see fig. 4, only the lower band is occupied. The only states playing a role in the behavior of the system lie around the chemical potential. They all have the same principal spin direction in this case, which makes the system effectively spinless.

Due to the spin-orbit field, the spins are not perfectly aligned, but depend on the momentum along the wire, as indicated by the red arrows in fig. 5(b). If the magnetic field is increased, as illustrated in fig. 5(c), the spins are more strongly forced to align, their momentum dependence fades away and the gap widens. The latter is a benefit, because it provides more room for placing the chemical potential within the gap. The momentum dependence of the spin, in contrast, is crucial to induce p-wave superconductivity with an s-wave superconductor, as explained in the following.

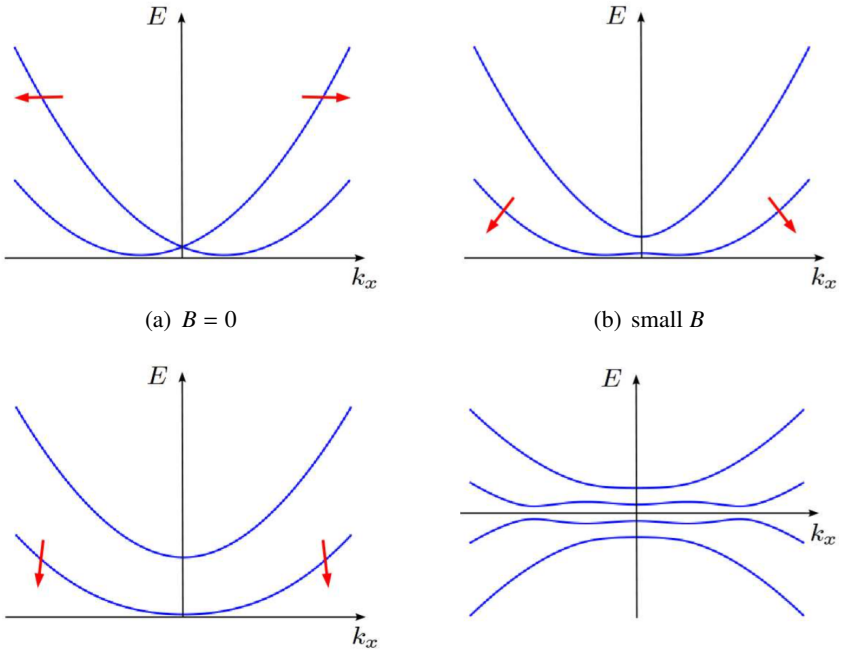

(a) $B = 0$ (b) small B

(c) large B (d) large B, induced pairing Δ

Figure 5: Band structure of the wire for different magnetic fields without, fig. (a), (b), (c), and with proximity-induced pairing, fig. (d). The red arrows indicate the spin direction perpendicular to the wire axis. The spin-orbit coupling is necessary, if the p-wave superconductivity is to be induced with an s-wave substrate, because it pairs opposite spin projections. All figures are taken from [20].

It has been previously stated that the wire inherits the pairing symmetry from the superconductor. If it had a p-wave symmetry the spin-orbit coupling would be redundant and the pairing potential would simply couple neighboring wire electrons with the same spin, separated from the other spin kind by the magnetic field. Since the substrate is an s-wave superconductor, only electrons showing spin components that are antiparallel are coupled to each other. Such components are provided by the spin-orbit coupling, because it breaks the polarization axis of the spins, which is present in a magnetic field, and makes them momentum dependent. Since the principal spin direction is still the same for all electrons, it turns out that the system can be treated as an effective p-wave superconductor.

Fig. 5(d) shows the band structure, when the proximity coupling is turned on. There are four solutions to each value of k_x, but only two of them are linearly independent. Due to the particle-hole symmetry, the positive energy bands are mirrored with respect to $E = 0$ and thus appear twice in the band structure. Otherwise the curves look similar to the ones obtained without proximity coupling, see fig. 5(b) and 5(c).

If the proximity-induced pairing amplitude in the wire is increased from zero and the other parameters are fixed, the gap gets smaller until it closes. Before this happens the system is in the

topological phase, after the closing of the gap it is in the trivial phase. The hamiltonian can be mapped onto the Kitaev hamiltonian in both phases by distinct transformations.
The benefit of this engineering method is that all ingredients are easily available and well studied. As semiconducting wires with a large spin-orbit coupling InAs or InSb, for example, have been tried by experimentalists. There are a number of systems that show s-wave superconductivity and represent suitable candidates for the substrate. For the wire materials just proposed Nb or Al have been adopted so far.
This paragraph follows mainly the review article [20] and the figures have been taken from this source, but I have abstained from using formulas here. Some more details can be found in [20]. [16] also holds an overview of the topic providing even more details. This article is better suited for the already well-versed reader. In [16] other realization methods are described, as well. Both articles list a number of papers with experiments.
The Kitaev Model can also be engineered with a half-metallic ferromagnetic wire, where only one spin kind is conducting. Since the spins are perfectly aligned in this system, a different method to induce superconductivity is necessary in this case. For details see [16].
Another very interesting proposal to realize Majorana fermions involves a graphene - superconductor junction, in this method spin-orbit coupling is not necessary [26].

4 Solution of the Lindblad equation

Before the Lindblad equation can be solved for the model systems, the Liouvillians are determined in sec 4.1. The calculations are carried out in superfermion representation, see sec. 2.3, where the Lindblad equation has the same structure as the Schrödinger equation and can be treated alike. One possibility to determine the systems' dynamics is via diagonalization of the Liouvillian. This method can be found in sec. 4.2 together with an alternative solution scheme. If the Liouvillian is already diagonalized and independent of time and the state of the system, the steady state can be determined directly, without evaluating the time evolution explicitely, as presented in sec. 4.3. The whole section 4 is based on my own work. The rough idea for the steady state - calculation in sec. 4.3 has been adapted from [10].

4.1 The Liouvillian

In sec. 4.1.1 the Liouvillian is calculated in the superfermion representation. In sec. 4.1.2 it is transferred to a matrix structure, in order to diagonalize it later. As an intermediate step a unitary transformation is applied, leading to a simpler matrix representation, see sec. 4.1.3. This serves to simplify the diagonalization task, finally carried out in sec. 4.1.4, and to gain important insights about the eigenvectors and eigenvalues for further analytical calculations. These insights are used for the direct evaluation of the steady state and the dynamics via diagonalization. Sec. 4.1.2 - 4.1.4 can be skipped, if the alternative calculation scheme is applied.

4.1.1 Superfermion representation

Hamiltonian: In the models studied within this thesis two different types of hamiltonians arise. The normal non-interacting hamiltonian $\hat{H}_n$ couples creation and annihilation operators pairwise, whereas the anomalous hamiltonian $\hat{H}_a$ originating from BCS pairing combines two creators or two annihilators, respectively. A generalized non-interacting hamiltonian $\hat{H}$ contains both contributions,

$$\begin{aligned} \hat{H} &= \hat{H}_n + \hat{H}_a \,, \\ \hat{H}_n &= \sum_{\mu\nu} c_\mu^\dagger h_{\mu\nu} c_\nu \,, \\ \hat{H}_a &= \sum_{\mu\nu} \left(c_\mu a_{\mu\nu} c_\nu + c_\mu^\dagger a_{\nu\mu}^* c_\nu^\dagger \right) \,. \end{aligned} \tag{69}$$

The coefficients can be arranged in NxN matrices, where N is the number of sites in the system. The hermiticity of the hamiltonian is inherited by the coefficient matrix $\boldsymbol{h}$. From the anticommutation relations (36) furthermore follows that $\boldsymbol{a}$ is skew symmetric,

$$\begin{aligned} \boldsymbol{h} &= \boldsymbol{h}^\dagger \,, \\ \boldsymbol{a} &= -\boldsymbol{a}^\intercal \,. \end{aligned} \tag{70}$$

The anomalous hamiltonian does not commute with the operator of the total number of particles in the system, $\hat{S}$, defined in eq. (72), in contrast to its normal counterpart,

$$\begin{aligned} [\hat{S}, \hat{H}_n] &= 0 \,, \\ [\hat{S}, \hat{H}_a] &= -2 \sum_{\mu\nu} \left(c_\mu a_{\mu\nu} c_\nu - c_\mu^\dagger a_{\nu\mu}^* c_\nu^\dagger \right) \neq 0 \,. \end{aligned} \tag{71}$$

As a consequence, the number of particles in a generalized non-interacting system is not conserved, $\frac{d}{dt}\langle\hat{S}\rangle \neq 0$, if the anomalous coefficient matrix is $\boldsymbol{a} = const. \neq 0$, with

$$\hat{S} = \sum_i c_i^\dagger c_i \,, \qquad i\frac{d}{dt}\langle\hat{S}\rangle = \langle[\hat{S},\hat{H}]\rangle \ . \tag{72}$$

Dissipator: The vector of Lindblad operators $\hat{\boldsymbol{M}}$ and the coefficient matrix $\boldsymbol{\gamma}$, describing the dissipative part in the Lindblad equation (12), are chosen as

$$\hat{\boldsymbol{M}} = \begin{pmatrix} \boldsymbol{c} \\ \boldsymbol{c}^\dagger \end{pmatrix} , \qquad \boldsymbol{\gamma} = \begin{pmatrix} \boldsymbol{\Gamma}^{(-)} & \boldsymbol{\Upsilon}^{(-)} \\ \boldsymbol{\Upsilon}^{(+)} & \boldsymbol{\Gamma}^{(+)} \end{pmatrix} . \tag{73}$$

$\boldsymbol{c}^{(\dagger)}$ is a Nx1 vector of annihilation (creation) operators, $\boldsymbol{\Gamma}^{(\pm)}$ and $\boldsymbol{\Upsilon}^{(\pm)}$ are NxN matrices, describing normal and anomalous couplings, respectively, see eq. (77). In order to comply with the properties of $\boldsymbol{\gamma}$, eq. (14) and (15), they have to obey

$$\boldsymbol{\Gamma}^{(-)} = \boldsymbol{\Gamma}^{(-)\dagger} \,, \qquad \boldsymbol{x}^\dagger\boldsymbol{\Gamma}^{(-)}\boldsymbol{x} \geq 0 \qquad \forall \boldsymbol{x} \,, \tag{74}$$

$$\boldsymbol{\Gamma}^{(+)} = \boldsymbol{\Gamma}^{(+)\dagger} \,, \qquad \boldsymbol{y}^\dagger\boldsymbol{\Gamma}^{(+)}\boldsymbol{y} \geq 0 \qquad \forall \boldsymbol{y} \,, \tag{75}$$

$$\boldsymbol{\Upsilon}^{(+)} = \boldsymbol{\Upsilon}^{(-)\dagger} \,. \tag{76}$$

The positive semidefiniteness of $\boldsymbol{\Gamma}^{(\pm)}$ follows from eq. (15) by taking $\boldsymbol{\upsilon} = (\boldsymbol{x}^\intercal, \boldsymbol{0})^\intercal$ and $\boldsymbol{\upsilon} = (\boldsymbol{0}, \boldsymbol{y}^\intercal)^\intercal$, respectively, where $\boldsymbol{x}$, $\boldsymbol{y}$ and $\boldsymbol{0}$ are Nx1 vectors. That $\boldsymbol{\Upsilon}^{(\pm)}$ preserves eq. (15) has to be ensured independently. Inserting eq. (73) into the Liouvillian (21) yields

$$\begin{aligned} \hat{\hat{L}}_D &= \hat{\hat{L}}_{D_n} + \hat{\hat{L}}_{D_a} \,, \\ \hat{\hat{L}}_{D_n}\,\hat{\rho} &= i\sum_{\mu\nu}\Big[\,\Gamma^{(-)}_{\mu\nu}\,(\,2c_\mu\,\hat{\rho}\,c_\nu^\dagger - \{\hat{\rho}, c_\nu^\dagger c_\mu\}\,) + \Gamma^{(+)}_{\mu\nu}\,(\,2c_\mu^\dagger\,\hat{\rho}\,c_\nu - \{\hat{\rho}, c_\nu c_\mu^\dagger\}\,)\,\Big] \,, \\ \hat{\hat{L}}_{D_a}\,\hat{\rho} &= i\sum_{\mu\nu}\Big[\,\Upsilon^{(-)}_{\mu\nu}\,(\,2c_\mu\,\hat{\rho}\,c_\nu - \{\hat{\rho}, c_\nu c_\mu\}\,) + \Upsilon^{(+)}_{\mu\nu}\,(\,2c_\mu^\dagger\,\hat{\rho}\,c_\nu^\dagger - \{\hat{\rho}, c_\nu^\dagger c_\mu^\dagger\}\,)\,\Big] \,. \end{aligned} \tag{77}$$

$\hat{\hat{L}}_{D_n}$ and $\hat{\hat{L}}_{D_a}$ denote the normal and anomalous contributions to the dissipator.

Liouvillian: The hamiltonian (69) is first inserted in eq. (20) and then in (19) together with the dissipator (77). The resulting Liouville superoperator is applied to $\hat{\rho}$ and then to the left vacuum (37). By exploiting the anticommutation relations (36), the tilde conjugation rules (38), the fact that the density operator is defined on the non-tilde state space and the definition of the nonequilibrium wave function (28), the Liouvillian $\hat{L}$ in superfermion representation, defined by eq. (30), can be determined.

$$\begin{aligned} \hat{L} = \sum_{\mu\nu}\Big[\; & h_{\mu\nu}(c_\mu^\dagger c_\nu + \tilde{d}_\mu^\dagger\tilde{d}_\nu - \delta_{\mu\nu}\mathbb{1}) && = \hat{L}_{H_n} \\ & + a_{\mu\nu}\,(c_\mu c_\nu + \tilde{d}_\mu\tilde{d}_\nu) + a^*_{\nu\mu}\,(c_\mu^\dagger c_\nu^\dagger + \tilde{d}_\mu^\dagger\tilde{d}_\nu^\dagger) && = \hat{L}_{H_a} \\ & + i\,\Omega_{\mu\nu}\,(c_\mu^\dagger c_\nu - \tilde{d}_\mu^\dagger\tilde{d}_\nu) + 2\Gamma^{(+)}_{\mu\nu}c_\mu^\dagger\tilde{d}_\nu - 2\Gamma^{(-)}_{\nu\mu}\tilde{d}_\mu^\dagger c_\nu - \delta_{\mu\nu}\Lambda_{\mu\nu}\mathbb{1} && = \hat{L}_{D_n} \\ & + \Upsilon^{(-)}_{\mu\nu}\,(2c_\mu\tilde{d}_\nu + ic_\mu c_\nu - i\tilde{d}_\mu\tilde{d}_\nu) + \Upsilon^{(+)}_{\mu\nu}\,(2c_\mu^\dagger\tilde{d}_\nu^\dagger + ic_\mu^\dagger c_\nu^\dagger - i\tilde{d}_\mu^\dagger\tilde{d}_\nu^\dagger)\Big] && = \hat{L}_{D_a} \end{aligned} \quad \Bigg\} = \hat{L}_D \tag{78}$$

The indices H, D, n, a again denote, whether the contribution to the Liouvillian is due to a hamiltonian or a dissipator and if it originates from a normal or an anomalous coupling. Within this formula new coefficients and operators arise

$$\boldsymbol{\Omega} = \boldsymbol{\Gamma}^{(+)} - \boldsymbol{\Gamma}^{(-)\intercal} \,, \tag{79}$$

$$\boldsymbol{\Lambda} = \boldsymbol{\Gamma}^{(+)} + \boldsymbol{\Gamma}^{(-)\intercal} \,, \tag{80}$$

$$\tilde{d}_\mu = \tilde{c}_\mu^\dagger \,. \tag{81}$$

The $\tilde{d}$ operators obey the same anticommutation relations as the original $\tilde{c}$ operators, eq. (36),

$$\begin{aligned} \{\tilde{d}_i \,, \tilde{d}_j^\dagger\} &= \delta_{ij} \,, \\ \{\tilde{d}_i^{(\dagger)}, \tilde{d}_j^{(\dagger)}\} = \{\tilde{d}_i^{(\dagger)}, c_j^{(\dagger)}\} &= 0 \,. \end{aligned} \tag{82}$$

The particle-hole transformation (81) ensures that normal (anomalous) superoperators give only rise to normal (anomalous) operators in superspace, which means that this property survives the map into superspace.

4.1.2 Matrix representation I

Within this subsection a matrix representation of the Liouvillian is determined. A distinction of cases is made between problems described by a Liouvillian with and without anomalous terms, respectively. In principle, they could be treated alike by considering only the generalized system and setting all anomalous coefficients to zero in the end, if the other case were in demand. In practice, it has proven useful to treat the normal system separately.

Normal system: In case of a normal system, $\boldsymbol{a} = \boldsymbol{\Upsilon}^{(\pm)} = \mathbf{0}$ in eq. (78) and the Liouvillian reduces to

$$\hat{L} = \hat{L}_{H_n} + \hat{L}_{D_n} \,. \tag{83}$$

By exploiting the anticommutation relations (36) and (82), $\hat{L}$ is brought into the following form,

$$\hat{L} = \boldsymbol{b}^\dagger \boldsymbol{L}' \boldsymbol{b} + C\mathbb{1} \,, \tag{84}$$

with the $2N$ x $2N$ matrix $\boldsymbol{L}'$, the $2N$ x 1 vector of operators $\boldsymbol{b}$ and the constant C,

$$\boldsymbol{L}' = \begin{pmatrix} \boldsymbol{h} + i\,\boldsymbol{\Omega} & 2\boldsymbol{\Gamma}^{(+)} \\ -2\boldsymbol{\Gamma}^{(-)\intercal} & \boldsymbol{h} - i\,\boldsymbol{\Omega} \end{pmatrix} \,, \qquad \boldsymbol{b} = \begin{pmatrix} \boldsymbol{c} \\ \tilde{\boldsymbol{d}} \end{pmatrix} \,, \qquad C = -\,\mathrm{tr}\,\{\boldsymbol{h} + i\,\boldsymbol{\Lambda}\} \,. \tag{85}$$

Since the basis operators are independent of each other, the matrix representation $\boldsymbol{L}'$ is unique.

Generalized system: If $\boldsymbol{a} \neq 0$ or $\boldsymbol{\Upsilon}^{(\pm)} \neq 0$ in eq. (78), the system has to be treated as a generalized system and $\hat{L}$ reads

$$\hat{L} = \hat{L}_{H_n} + \hat{L}_{H_a} + \hat{L}_{D_n} + \hat{L}_{D_a} \,. \tag{86}$$

The operator basis in eq. (85) is not sufficient to represent the Liouvillian as

$$\hat{L} = \boldsymbol{b}^\dagger \boldsymbol{L}' \boldsymbol{b} + C\mathbb{1} \,. \tag{87}$$

To include anomalous couplings, it has to be extended by the hermitian conjugated operators. In this case $\boldsymbol{L}'$ is a $4N$ x $4N$ matrix, $\boldsymbol{b}$ a $4N$ x 1 vector and C again a constant,

$$\boldsymbol{L}' = \begin{pmatrix} \frac{1}{2}(\boldsymbol{h} + i\boldsymbol{\Omega}) & \boldsymbol{a}^\dagger + i\boldsymbol{\Upsilon}^{(+)} & \boldsymbol{\Gamma}^{(+)} & \boldsymbol{\Upsilon}^{(+)} \\ \boldsymbol{a} + i\boldsymbol{\Upsilon}^{(-)} & -\frac{1}{2}(\boldsymbol{h} + i\boldsymbol{\Omega})^\intercal & \boldsymbol{\Upsilon}^{(-)} & \boldsymbol{\Gamma}^{(-)} \\ -\left(\boldsymbol{\Gamma}^{(-)}\right)^\intercal & -\left(\boldsymbol{\Upsilon}^{(+)}\right)^\intercal & \frac{1}{2}(\boldsymbol{h} - i\boldsymbol{\Omega}) & \boldsymbol{a}^\dagger - i\boldsymbol{\Upsilon}^{(+)} \\ -\left(\boldsymbol{\Upsilon}^{(-)}\right)^\intercal & -\left(\boldsymbol{\Gamma}^{(+)}\right)^\intercal & \boldsymbol{a} - i\boldsymbol{\Upsilon}^{(-)} & -\frac{1}{2}(\boldsymbol{h} - i\boldsymbol{\Omega})^\intercal \end{pmatrix}, \quad \boldsymbol{b} = \begin{pmatrix} \boldsymbol{c} \\ \boldsymbol{c}^\dagger \\ \tilde{\boldsymbol{d}} \\ \tilde{\boldsymbol{d}}^\dagger \end{pmatrix}, \quad C = -i \text{ tr } \{\boldsymbol{\Lambda}\}. \tag{88}$$

The matrix $\boldsymbol{L}'$ is not unique anymore. The coefficient α of a particular coupling $c_i^\dagger c_j$ in $\hat{L}$ can be arbitrarily split up and assigned to the two elements in $\boldsymbol{L}'$ connecting these operators via eq. (87),

$$L'_{ij}\, c_i^\dagger c_j + L'_{j+N,\, i+N}\, c_j c_i^\dagger = \underbrace{\left(L'_{ij} - L'_{j+N,\, i+N}\right)}_{=\alpha} c_i^\dagger c_j + const. \tag{89}$$

In eq. (88) the coefficients of $\hat{L}$ have been evenly distributed onto dependent matrix blocks. By considering the evolution equation for the b operators in the Heisenberg picture, it can be learned that this is the correct way of representation.

4.1.3 Matrix representation II

In this subsection the previously obtained matrix representation, eq. (85) or (88), is simplified by carrying out a unitary transformation. With this intermediate step the Liouvillian can be diagonalized more efficiently. The new representation allows to gain insights into the structure of its eigenvectors and eigenvalues, which are crucial for determining the time evolution and the steady state of the system by diagonalization. Eq. (84) is rewritten as

$$\begin{aligned} \hat{L} &= \boldsymbol{b}^\dagger \boldsymbol{L}' \boldsymbol{b} + C\mathbb{1} \\ &= \boldsymbol{e}^\dagger \boldsymbol{L}'' \boldsymbol{e} + C\mathbb{1}\,. \end{aligned} \tag{90}$$

The transformation is described by the unitary matrix $\boldsymbol{R}$,

$$\boldsymbol{R} = \frac{1}{\sqrt{2}} \begin{pmatrix} \mathbb{1} & i\,\mathbb{1} \\ \mathbb{1} & -i\,\mathbb{1} \end{pmatrix}, \tag{91}$$

$$\boldsymbol{L}'' = \boldsymbol{R}\boldsymbol{L}'\boldsymbol{R}^\dagger\,, \qquad \boldsymbol{e} = \boldsymbol{R}\boldsymbol{b}\,. \tag{92}$$

$\mathbb{1}$ is the N x N or the $2N$ x $2N$ identity matrix, depending on which of the systems, the normal or the generalized one, is regarded. In order to investigate, how the transformation acts in detail, the two systems are again treated separately.

Normal system: In case of a normal system, eq. (85), $\boldsymbol{L}''$ and $\boldsymbol{e}$ are given by

$$\boldsymbol{L}'' = \begin{pmatrix} \boldsymbol{h} - i\boldsymbol{\Lambda} & 2i\boldsymbol{\Omega} \\ \boldsymbol{0} & \boldsymbol{h} + i\boldsymbol{\Lambda} \end{pmatrix}, \qquad \boldsymbol{e} = \begin{pmatrix} \boldsymbol{A} \\ \boldsymbol{B}^\dagger \end{pmatrix}. \tag{93}$$

$A_j^\dagger$ and $B_j^\dagger$ are the left vacuum annihilators, eq.(39). Obviously, the new matrix $\boldsymbol{L}''$ has a block upper triangular structure.

Generalized system: Applying the transformation (92) to the generalized system, eq. (88), yields

$$\boldsymbol{L}'' = \begin{pmatrix} \frac{1}{2}(\boldsymbol{h} - i\boldsymbol{\Lambda}) & (\boldsymbol{a} + i\mathbf{X})^\dagger & i\boldsymbol{\Omega} & i(2\mathbf{Z} + \mathbf{X})^\dagger \\ \boldsymbol{a} - i\mathbf{X} & -\frac{1}{2}(\boldsymbol{h} + i\boldsymbol{\Lambda})^\intercal & i(2\mathbf{Z} + \mathbf{X}) & -i\boldsymbol{\Omega}^\intercal \\ \mathbf{0} & i\mathbf{X}^\dagger & \frac{1}{2}(\boldsymbol{h} + i\boldsymbol{\Lambda}) & (\boldsymbol{a} - i\mathbf{X})^\dagger \\ i\mathbf{X} & \mathbf{0} & (\boldsymbol{a} + i\mathbf{X}) & -\frac{1}{2}(\boldsymbol{h} - i\boldsymbol{\Lambda})^\intercal \end{pmatrix}, \qquad \boldsymbol{e} = \begin{pmatrix} \boldsymbol{A} \\ \boldsymbol{B} \\ \boldsymbol{B}^\dagger \\ \boldsymbol{A}^\dagger \end{pmatrix}. \tag{94}$$

$\boldsymbol{e}$ can again be expressed in terms of the left vacuum annihilators. New matrices $\mathbf{X}$ and $\mathbf{Z}$ have been introduced,

$$\begin{aligned} \mathbf{X} &= \frac{1}{2}\left(\boldsymbol{\Upsilon}^{(-)} + \boldsymbol{\Upsilon}^{(-)\intercal}\right), \\ \mathbf{Z} &= \frac{1}{2}\left(\boldsymbol{\Upsilon}^{(-)} - \boldsymbol{\Upsilon}^{(-)\intercal}\right). \end{aligned} \tag{95}$$

If $\boldsymbol{\Upsilon}^{(\pm)} = -\boldsymbol{\Upsilon}^{(\pm)\intercal}$, which means $\mathbf{X} = \mathbf{0}$, is fulfilled, $\boldsymbol{L}''$ becomes a block upper triangular matrix also in case of a generalized system,

$$\boldsymbol{L}'' = \begin{pmatrix} \frac{1}{2}(\boldsymbol{h} - i\boldsymbol{\Lambda}) & \boldsymbol{a}^\dagger & i\boldsymbol{\Omega} & 2i\boldsymbol{\Upsilon}^{(+)} \\ \boldsymbol{a} & -\frac{1}{2}(\boldsymbol{h} + i\boldsymbol{\Lambda})^\intercal & 2i\boldsymbol{\Upsilon}^{(-)} & -i\boldsymbol{\Omega}^\intercal \\ \mathbf{0} & \mathbf{0} & \frac{1}{2}(\boldsymbol{h} + i\boldsymbol{\Lambda}) & \boldsymbol{a}^\dagger \\ \mathbf{0} & \mathbf{0} & \boldsymbol{a} & -\frac{1}{2}(\boldsymbol{h} - i\boldsymbol{\Lambda})^\intercal \end{pmatrix}. \tag{96}$$

This is assumed in the following calculations.

4.1.4 Diagonalization

As previously stated, one possibility to solve the Lindblad equation leads across the diagonalization of the generating Liouvillian. This method corresponds to the solution of the Schrödinger equation in a closed system by diagonalizing the hamiltonian. Starting from eq. (90), the Liouvillian is expressed as

$$\begin{aligned} \hat{L} &= \boldsymbol{e}^\dagger \boldsymbol{L}'' \boldsymbol{e} + C\mathbb{1} \\ &= \bar{\boldsymbol{f}}\, \boldsymbol{D}\, \boldsymbol{f} + C\mathbb{1}. \end{aligned} \tag{97}$$

The transformation is described by a non-unitary matrix $\boldsymbol{U}$ with $\boldsymbol{V} \equiv \boldsymbol{U}^{-1} \neq \boldsymbol{U}^\dagger$, because the Liouvillian is not hermitian and this property is inherited by the coefficient matrices $\boldsymbol{L}'$ and $\boldsymbol{L}''$,

$$\begin{aligned} \boldsymbol{D} &= \boldsymbol{V}\boldsymbol{L}''\boldsymbol{U}, \\ \boldsymbol{f} &= \boldsymbol{V}\,\boldsymbol{e}, \\ \bar{\boldsymbol{f}} &= \boldsymbol{e}^\dagger \boldsymbol{U}. \end{aligned} \tag{98}$$

The matrix $\boldsymbol{U}$ maps $\boldsymbol{L}''$ onto the diagonal matrix $\boldsymbol{D}$, which has the eigenvalues λ_i of $\boldsymbol{L}''$ as entries,

$$D_{ij} = \lambda_i\, \delta_{ij}. \tag{99}$$

Since $\boldsymbol{U}$ is not unitary, the eigenmode operators f_i and $\bar{f}_i$ are not related to each other by hermitian conjugation, in contrast to the operators resulting from a unitary transformation,

$$f_i^\dagger \neq \bar{f}_i. \tag{100}$$

In case of a normal system, they still obey the fermionic anticommutation relations, see eq. (114), in case of a generalized one they don't, see eq. (117), but they satisfy the K - relations, eq. (157). With eq. (99) the Liouvillian is expressed as

$$\hat{L} = \sum_i \lambda_i \bar{f}_i f_i + C\mathbb{1} \,. \tag{101}$$

Realization in practice: This paragraph shows, how the diagonalization can be carried out in practice. For a normal as well as a generalized system the matrix $\boldsymbol{L''}$ has a block upper triangular form and the following structure,

$$\boldsymbol{L''} = \begin{pmatrix} \boldsymbol{\alpha} & \beta \\ \boldsymbol{0} & \boldsymbol{\alpha}^\dagger \end{pmatrix} . \tag{102}$$

$\boldsymbol{\alpha}$ and $\boldsymbol{\beta}$ serve as placeholders for the block matrices in eq. (93) and (96). In the following the consequences of this structure for $\boldsymbol{U}$ and $\boldsymbol{V}$ are determined. The eigenvalue equation for $\boldsymbol{L''}$ reads

$$\boldsymbol{L''}\boldsymbol{\upsilon} = \lambda\,\boldsymbol{\upsilon} \,, \tag{103}$$

where λ is an eigenvalue of $\boldsymbol{L''}$ and $\boldsymbol{\upsilon}$ the corresponding eigenvector. Inserting $\boldsymbol{\upsilon}^\intercal = (\boldsymbol{x}^\intercal, \boldsymbol{y}^\intercal)$ in eq. (103) yields the following set of equations,

$$\boldsymbol{\alpha x} + \boldsymbol{\beta y} = \lambda\,\boldsymbol{x} \,, \tag{104}$$

$$\boldsymbol{\alpha}^\dagger \boldsymbol{y} = \lambda\,\boldsymbol{y} \,. \tag{105}$$

It has two different types of solutions. By exploiting that the eigenvalues of a matrix and its adjoint are complex conjugated to each other, the solutions read

1. $\boldsymbol{\upsilon}_1 = \begin{pmatrix} \boldsymbol{x}_{\boldsymbol{\alpha}} \\ \boldsymbol{0} \end{pmatrix}$, $\lambda = \lambda^{(\alpha)}$: $\boldsymbol{x}_{\boldsymbol{\alpha}}$ is an eigenvector of $\boldsymbol{\alpha}$ to the eigenvalue $\lambda^{(\alpha)}$

2. $\boldsymbol{\upsilon}_2 = \begin{pmatrix} \boldsymbol{x}_{\boldsymbol{y}_{\boldsymbol{\alpha}^\dagger}} \\ \boldsymbol{y}_{\boldsymbol{\alpha}^\dagger} \end{pmatrix}$, $\lambda = \lambda^{(\alpha)*}$: $\boldsymbol{y}_{\boldsymbol{\alpha}^\dagger}$ is an eigenvector of $\boldsymbol{\alpha}^\dagger$ to the eigenvalue $\lambda^{(\alpha)*}$, $\boldsymbol{x}_{\boldsymbol{y}_{\boldsymbol{\alpha}^\dagger}}$ is calculated from (104) as $\boldsymbol{x}_{\boldsymbol{y}_{\boldsymbol{\alpha}^\dagger}} = (\lambda^{(\alpha)*}\,\mathbb{1} - \boldsymbol{\alpha})^{-1}\boldsymbol{\beta}\,\boldsymbol{y}_{\boldsymbol{\alpha}^\dagger}$

The columns of the diagonalizing matrix contain the eigenvectors of the matrix to diagonalize. If the eigenvectors of $\boldsymbol{\alpha}$ form the columns of the matrix $\boldsymbol{u}$, the columns of $\boldsymbol{u}^{-1^\dagger}$ contain the eigenvectors of $\boldsymbol{\alpha}^\dagger$,

$$\boldsymbol{\alpha} \;=\; \boldsymbol{u}\,\boldsymbol{D}^{(\alpha)}\boldsymbol{u}^{-1} \,, \tag{106}$$

$$\boldsymbol{\alpha}^\dagger \;=\; \boldsymbol{u}^{-1^\dagger}\boldsymbol{D}^{(\alpha)\dagger}\boldsymbol{u}^\dagger \,. \tag{107}$$

The second equation follows from the first one by hermitian conjugation. The diagonal matrix containing the eigenvalues $\lambda^{(\alpha)}$ has been called $\boldsymbol{D}^{(\alpha)}$. According to the previous considerations, $\boldsymbol{U}$ and $\boldsymbol{D}$ have the following structure,

$$\boldsymbol{U} = \begin{pmatrix} \boldsymbol{u} & \boldsymbol{u}^{(c)} \\ \boldsymbol{0} & \boldsymbol{u}^{-1^\dagger} \end{pmatrix} , \qquad \boldsymbol{D} = \begin{pmatrix} \boldsymbol{D}^{(\alpha)} & \boldsymbol{0} \\ \boldsymbol{0} & \boldsymbol{D}^{(\alpha)\dagger} \end{pmatrix} . \tag{108}$$

The columns of $\boldsymbol{u}^{(c)}$ contain the calculated vectors $\boldsymbol{x}_{\boldsymbol{y}_{\boldsymbol{\alpha}^\dagger}}$ for each $\lambda^{(\alpha)*}$, as presented in point 2. The overall eigenvalue equation (103) can also be written as

$$\boldsymbol{L''}\boldsymbol{U} = \boldsymbol{U}\boldsymbol{D} \,. \tag{109}$$

Inserting eq. (102) and (108) yields in addition to the eigenvalue equations (106) and (107) the following equation,

$$\boldsymbol{\alpha}\boldsymbol{u}^{(c)} + \boldsymbol{\beta}\boldsymbol{u}^{-1\dagger} = \boldsymbol{u}^{(c)}\boldsymbol{D}^{(\alpha)\dagger} \,. \tag{110}$$

In order to determine $\boldsymbol{U}$, it is sufficient to diagonalize only $\boldsymbol{\alpha}$, yielding $\boldsymbol{u}$ and $\boldsymbol{D}^{(\alpha)}$. The other matrix blocks can be calculated from the result. Assuming a general form for the inverse $\boldsymbol{V}$,

$$\boldsymbol{V} = \begin{pmatrix} \boldsymbol{v}_1 & \boldsymbol{v}_2 \\ \boldsymbol{v}_3 & \boldsymbol{v}_4 \end{pmatrix} ,$$

the blocks are achieved with $\boldsymbol{UV} = \mathbb{1}$ ($= \boldsymbol{VU}$) from eq. (108) by comparison of coefficients. It turns out that $\boldsymbol{V}$ can be calculated by inverting only the block matrix $\boldsymbol{u}$,

$$\boldsymbol{V} = \begin{pmatrix} \boldsymbol{u}^{-1} & -\boldsymbol{u}^{-1}\boldsymbol{u}^{(c)}\boldsymbol{u}^{\dagger} \\ \boldsymbol{0} & \boldsymbol{u}^{\dagger} \end{pmatrix} . \tag{111}$$

The block upper triangular form of $\boldsymbol{L}''$results in a block upper triangular form of the diagonalizing matrix $\boldsymbol{U}$ and its inverse $\boldsymbol{V}$. In practice, it is not necessary to diagonalize or invert the full matrix, but it is sufficient to handle block matrices of half the size.

Normal system: From the definition of the operators $\bar{f}$ and f, eq. (98), follows directly by inserting eq. (93), (108) and (111).

$$f_n = \begin{cases} \displaystyle\sum_{k=1}^{N} \left[\left(\boldsymbol{u}^{-1}\right)_{n,k} A_k - \left(\boldsymbol{u}^{-1}\boldsymbol{u}^{(c)}\boldsymbol{u}^{\dagger}\right)_{n,k} B_k^{\dagger} \right] & \text{for } n \in [1, N] \\ \displaystyle\sum_{k=1}^{N} \left(\boldsymbol{u}^{\dagger}\right)_{n-N,k} B_k^{\dagger} & \text{for } n \in [N+1, 2N] \end{cases} \tag{112}$$

$$\bar{f}_n = \begin{cases} \displaystyle\sum_{k=1}^{N} u_{k,n} A_k^{\dagger} & \text{for } n \in [1, N] \\ \displaystyle\sum_{k=1}^{N} \left[u^{(c)}_{k,n-N} A_k^{\dagger} + \left(\boldsymbol{u}^{-1\dagger}\right)_{k,n-N} B_k \right] & \text{for } n \in [N+1, 2N] \end{cases} \tag{113}$$

By exploiting eq. (40) it can be learned that the eigenmode operators also obey the fermionic anticommutation relations,

$$\begin{aligned} \left\{\bar{f}_n, f_m\right\} &= \delta_{nm} \,, \\ \left\{f_n, f_m\right\} &= \left\{\bar{f}_n, \bar{f}_m\right\} = 0 \,, \end{aligned} \tag{114}$$

although they are not hermitian conjugate to each other.

Generalized system: The eigenmode operators for the generalized system are calculated from eq. (98) with (94), (96), (108) and (111). The result is:

$$f_n = \begin{cases} \sum_{k=1}^{N}\Big[\left(\boldsymbol{u}^{-1}\right)_{n,k} A_k + \left(\boldsymbol{u}^{-1}\right)_{n,k+N} B_k & \text{for } n \in [1,2N] \\ \quad - \left(\boldsymbol{u}^{-1}\boldsymbol{u}^{(c)}\boldsymbol{u}^{\dagger}\right)_{n,k+N} A_k^{\dagger} - \left(\boldsymbol{u}^{-1}\boldsymbol{u}^{(c)}\boldsymbol{u}^{\dagger}\right)_{n,k} B_k^{\dagger}\Big] & \\ \sum_{k=1}^{N}\Big[\left(\boldsymbol{u}^{\dagger}\right)_{n-2N,k+N} A_k^{\dagger} + \left(\boldsymbol{u}^{\dagger}\right)_{n-2N,k} B_k^{\dagger}\Big] & \text{for } n \in [2N+1,4N] \end{cases} \tag{115}$$

$$\bar{f}_n = \begin{cases} \sum_{k=1}^{N}\Big[u_{k,n} A_k^{\dagger} + u_{k+N,n} B_k^{\dagger}\Big] & \text{for } n \in [1,2N] \\ \sum_{k=1}^{N}\Big[\left(\boldsymbol{u}^{-1^{\dagger}}\right)_{k+N,n-2N} A_k + \left(\boldsymbol{u}^{-1^{\dagger}}\right)_{k,n-2N} B_k & \text{for } n \in [2N+1,4N] \\ \quad + u^{(c)}_{k,n-2N} A_k^{\dagger} + u^{(c)}_{k+N,n-2N} B_k^{\dagger}\Big] & \end{cases} \tag{116}$$

By using again eq. (40) their anticommutation relations are determined.

$$\left\{\bar{f}_n\,, f_m\right\} = \delta_{nm}$$

$$K_{nm} := \{f_n\,, f_m\} =$$

$$= \begin{cases} -\sum_{k=1}^{N}\Big[\left(\boldsymbol{u}^{-1}\right)_{n,k}\left(\boldsymbol{u}^{-1}\boldsymbol{u}^{(c)}\boldsymbol{u}^{\dagger}\right)_{m,k+N} + \left(\boldsymbol{u}^{-1}\right)_{n,k+N}\left(\boldsymbol{u}^{-1}\boldsymbol{u}^{(c)}\boldsymbol{u}^{\dagger}\right)_{m,k} & \text{for } n,m \in [1,2N] \\ \quad + \left(\boldsymbol{u}^{-1}\boldsymbol{u}^{(c)}\boldsymbol{u}^{\dagger}\right)_{n,k}\left(\boldsymbol{u}^{-1}\right)_{m,k+N} + \left(\boldsymbol{u}^{-1}\boldsymbol{u}^{(c)}\boldsymbol{u}^{\dagger}\right)_{n,k+N}\left(\boldsymbol{u}^{-1}\right)_{m,k}\Big] & \\ \sum_{k=1}^{N}\Big[\left(\boldsymbol{u}^{-1}\right)_{n,k}\left(\boldsymbol{u}^{\dagger}\right)_{m-2N,k+N} + \left(\boldsymbol{u}^{-1}\right)_{n,k+N}\left(\boldsymbol{u}^{\dagger}\right)_{m-2N,k}\Big] & \text{for } n \in [1,2N]\,, \\ & \quad m \in [2N+1,4N] \\ 0 & \text{for } n,m \in [2N+1,4N] \end{cases}$$

$$\overline{K}_{nm} := \left\{\bar{f}_n\,, \bar{f}_m\right\} =$$

$$= \begin{cases} 0 & \text{for } n,m \in [1,2N] \\ \sum_{k=1}^{N}\Big[u_{k,n}\left(\boldsymbol{u}^{-1^{\dagger}}\right)_{k+N,m-2N} + u_{k+N,n}\left(\boldsymbol{u}^{-1^{\dagger}}\right)_{k,m-2N}\Big] & \text{for } n \in [1,2N]\,, \\ & \quad m \in [2N+1,4N] \\ \sum_{k=1}^{N}\Big[u^{(c)}_{k,n-2N}\left(\boldsymbol{u}^{-1^{\dagger}}\right)_{k+N,m-2N} + u^{(c)}_{k+N,n-2N}\left(\boldsymbol{u}^{-1^{\dagger}}\right)_{k,m-2N} & \text{for } n,m \in [2N+1,4N] \\ \quad + \left(\boldsymbol{u}^{-1^{\dagger}}\right)_{k,n-2N} u^{(c)}_{k+N,m-2N} + \left(\boldsymbol{u}^{-1^{\dagger}}\right)_{k+N,n-2N} u^{(c)}_{k,m-2N}\Big] & \end{cases} \tag{117}$$

$\{\bar{f}_n\,, f_m\}$ is the same for the normal system, the other anticommutators are not identical to zero and therefore differ from the fermionic anticommutation relations and the results achieved for the normal system. This hardens the analytical part of the calculations, fortunately it can be shown that they obey, what I called, K - relations, eq. (157).
These relations are used to evaluate sums over the anticommutators $\boldsymbol{K}$ and $\overline{\boldsymbol{K}}$, as they arise in the calculation of the time evolution and the steady state via diagonalization. They are explicitly used in sec. 7.3 only, to calculate commutators of the f - operators with the Liouvillian. The factor κ that arises in the time evolution, eq. (125) and (126), is determined with their help and also the proof in sec. 7.5 that contributes to identify the steady state in sec. 4.3.

4.2 Time evolution

In this subsection the Lindblad equation (30) is solved for the Liouvillian from sec. 4.1 and the time evolution of the system is determined. I do not solve the differential equation directly for the nonequilibrium wave function, but calculate the time dependent expectation values of system operators instead,

$$\begin{aligned} i\tfrac{d}{dt}\langle\hat{O}(t)\rangle &= \langle I|\,\hat{O}\; i\tfrac{d}{dt}|\rho(t)\rangle \\ &= \langle I|\,\hat{O}\hat{L}\,|\rho(t)\rangle \\ &= \langle I|\left[\hat{O},\hat{L}\right]|\rho(t)\rangle\ . \end{aligned} \tag{118}$$

Eq. (118) follows from eq. (31) by taking the derivative with respect to time, inserting the Lindblad equation (30) and then exploiting the property (32). In case of a generalized noninteracting system I am especially interested in the following expectation values,

$$\begin{aligned} \rho_{\mu\nu} &= \langle c_\mu^\dagger c_\nu\rangle\ , \\ \eta_{\mu\nu} &= \langle c_\mu c_\nu\rangle\ , \\ \xi_{\mu\nu} &= \langle c_\mu^\dagger c_\nu^\dagger\rangle\ . \end{aligned} \tag{119}$$

In case of a normal system $\boldsymbol{\rho}$ is sufficient. These expectation values can be used to calculate the retarded Green's function and thus the spectral function of the system. Eq. (140) displays the result in the steady state. Furthermore the occupation numbers and bond currents can be determined from $\boldsymbol{\rho}$, according to eq. (145) and (146). In sec. 4.2.1 and 4.2.2 two schemes are presented to solve eq. (118) for the relevant operators in eq. (119).

4.2.1 Solution by diagonalization

The first solution scheme for eq. (118) is based on the diagonalization of the Liouvillian, which yields the representation (101). By chosing for all possible pairs of indices (r, s),

$$\hat{O} = b_r^\dagger b_s\ , \tag{120}$$

with $\boldsymbol{b}$ from eq. (85) or (88), all relevant operators in eq. (119) are considered. In order to evaluate the commutator with the Liouvillian, they are also expressed in terms of eigenmode operators,

$$\begin{aligned} \boldsymbol{b} &= \boldsymbol{R}^\dagger \boldsymbol{U}\boldsymbol{f}\ , \\ \boldsymbol{b}^\dagger &= \bar{\boldsymbol{f}}\,\boldsymbol{V}\boldsymbol{R}\ . \end{aligned} \tag{121}$$

Eq. (121) follows by combining eq. (92) with (98). Inserting the respective components into eq. (120) yields the following transformation, together with its inverse.

$$b_r^\dagger b_s = \sum_{mnpq} \left(\boldsymbol{R}^\dagger\right)_{sq} U_{qm}\, \bar{f}_n\, f_m V_{np}\, R_{pr} \tag{122}$$

$$\bar{f}_n f_m = \sum_{hjkl} V_{mh}\, R_{hj}\, b_k^\dagger\, b_j \left(\boldsymbol{R}^\dagger\right)_{kl} U_{ln} \tag{123}$$

The calculation of the commutator in eq. (118) therefore reduces to the calculation of $[\bar{f}_n\, f_m\,, \hat{L}]$. For the normal system this is easily evaluated, using the simple anticommutation relations (114).

For the generalized system these relations are far more complicated, see eq. (117). The commutator can be evaluated with the help of the K - relations (157), see sec. 7.3. Exploiting eq. (177) yields

$$\left[\bar{f}_n f_m\,, L\right] = \kappa\,(\lambda_m - \lambda_n)\,\bar{f}_n f_m\ . \tag{124}$$

$$\kappa = \begin{cases} 1\,, & \text{normal system} \\ 2\,, & \text{generalized system} \end{cases} \tag{125}$$

Thus the differential equation (118) decouples different pairs of eigenmode operators $\bar{f}_n f_m$. It can be solved for them independently and the solutions can be superposed afterwards to the original operators $b_r^\dagger b_s$.

$$\begin{aligned} i\frac{d}{dt}\,\langle \bar{f}_n f_m\rangle &= \kappa\,(\lambda_m - \lambda_n)\,\langle \bar{f}_n f_m\rangle \\ \langle \bar{f}_n f_m\rangle_t &= e^{-i\kappa(\lambda_m-\lambda_n)\,t}\,\langle \bar{f}_n f_m\rangle_0 \end{aligned} \tag{126}$$

In the second line the differential equation has been integrated from 0 to t. For simplicity the time variable is written as a subscript. Inserting the result in eq. (122) yields

$$\langle b_r^\dagger b_s\rangle_t = \sum_{mnpq} \left(\boldsymbol{R}^\dagger\right)_{sq} U_{qm}\, e^{-i\kappa(\lambda_m-\lambda_n)\,t}\,\langle \bar{f}_n f_m\rangle_0\, V_{np}\, R_{pr}\ . \tag{127}$$

The initial expectation values are also expressed in terms of b operators, using eq. (123).

$$\begin{aligned} \langle b_r^\dagger b_s\rangle_t &= \sum_{mnpq}\sum_{hjkl} \left(\boldsymbol{R}^\dagger\right)_{sq} U_{qm}\, e^{-i\kappa\lambda_m t}\, V_{mh}\, R_{hj}\, \langle b_k^\dagger b_j\rangle_0 \left(\boldsymbol{R}^\dagger\right)_{kl} U_{ln}\, e^{i\kappa\lambda_n t}\, V_{np}\, R_{pr} \\ &= \sum_{jk} \left(\boldsymbol{R}^\dagger \boldsymbol{U}\, e^{-i\kappa \boldsymbol{D} t}\, \boldsymbol{V}\boldsymbol{R}\right)_{sj} \langle b_k^\dagger b_j\rangle_0 \left(\boldsymbol{R}^\dagger \boldsymbol{U}\, e^{i\kappa \boldsymbol{D} t}\, \boldsymbol{V}\boldsymbol{R}\right)_{kr} \\ &= \sum_{jk} \left(\boldsymbol{R}^\dagger\, e^{-i\kappa \boldsymbol{L}'' t}\, \boldsymbol{R}\right)_{sj} \langle b_k^\dagger b_j\rangle_0 \left(\boldsymbol{R}^\dagger\, e^{i\kappa \boldsymbol{L}'' t}\, \boldsymbol{R}\right)_{kr} \\ &= \sum_{jk} \left(\, e^{-i\kappa \boldsymbol{L}' t}\,\right)_{sj} \langle b_k^\dagger b_j\rangle_0 \left(\, e^{i\kappa \boldsymbol{L}' t}\,\right)_{kr} \end{aligned} \tag{128}$$

The last two lines follow from eq. (98) and (92) by power series expansion of the exponential. Note that the solution (128) is only valid, if the Liouvillian does not depend on the state of the system and is independent of time. This has been assumed in the steps (126) - (128). Otherwise an alternative solution method is necessary, as presented in sec. 4.2.2.

4.2.2 Direct solution

Alternatively, the commutator in eq. (118) can be directly evaluated for the operators in eq. (119) without an intermediate diagonalization step. This yields the following set of coupled differential equations:

$$\begin{aligned} \dot{\boldsymbol{\rho}} &= \boldsymbol{\mathcal{H}}^\intercal \boldsymbol{\rho} + \boldsymbol{\mathcal{A}}^\intercal \boldsymbol{\eta} + \boldsymbol{\Gamma}^{(+)\intercal} + \text{h.c.} \\ \dot{\boldsymbol{\eta}} &= \boldsymbol{\mathcal{H}}^\dagger \boldsymbol{\eta} + \boldsymbol{\mathcal{A}}^\dagger \boldsymbol{\rho} + \boldsymbol{C}^\dagger \quad - \text{trs.} \\ \dot{\boldsymbol{\xi}} &= \boldsymbol{\xi}\boldsymbol{\mathcal{H}} \ + \boldsymbol{\rho}\boldsymbol{\mathcal{A}} \ + \boldsymbol{C} \quad - \text{trs.} \end{aligned} \tag{129}$$

'h.c.' again means hermitian conjugate and 'trs.' transposed. From this representation it can be immediately seen that the properties $\boldsymbol{\rho} = \boldsymbol{\rho}^\dagger$, $\boldsymbol{\eta} = -\boldsymbol{\eta}^\intercal$, $\boldsymbol{\xi} = -\boldsymbol{\xi}^\intercal$ and $\boldsymbol{\xi} = \boldsymbol{\eta}^\dagger$ are maintained during the time evolution as required. Due to the last property, the equation for $\boldsymbol{\xi}$ is redundant

and can thus be skipped. Eq. (129) follows from a long but simple calculation, exploiting the fermionic anticommutation relations (36), the tilde conjugation rules (38) and the symmetries of $\boldsymbol{h}$, $\boldsymbol{a}$, $\boldsymbol{\Gamma}^{(\pm)}$ and $\boldsymbol{\Upsilon}^{(\pm)}$, eq. (70) and (74) - (76). These matrices form the coefficients in eq. (129) with the definitions (80) and (95):

$$\begin{aligned} \boldsymbol{\mathcal{H}} &= \quad (i\,\boldsymbol{h} - \boldsymbol{\Lambda}) \\ \boldsymbol{\mathcal{A}} &= 2\,(i\,\boldsymbol{a} - \mathbf{X}) \\ \boldsymbol{C} &= -\,(i\,\boldsymbol{a} + \mathbf{Z}) \end{aligned} \tag{130}$$

If these coefficients are constants, the set of equations can be solved by rearranging the elements into a matrix-vector equation, $\dot{\boldsymbol{v}} = \boldsymbol{M}\boldsymbol{v} + const.$, and diagonalizing the matrix $\boldsymbol{M}$, as in sec. 4.2.1. If the coefficients in eq. (130) depend on time or on the variables $\boldsymbol{\rho}$ or $\boldsymbol{\eta}$, eq. (129) can be solved with a Runge-Kutta scheme, for example.

4.3 Steady state

If the system is left alone to evolve for some time, a steady state may be reached, where the observables do not depend on time anymore. If such a steady state exists, expectation values of eigenmode operators $\langle \bar{f}_n f_m \rangle_t$ are bounded and tend to a constant value for $t \to \infty$. By rephrasing the time evolution (126),

$$\langle \bar{f}_n f_m \rangle_t = e^{-i\kappa\,\Re(\lambda_m - \lambda_n)\,t} e^{\kappa\,\Im(\lambda_m - \lambda_n)\,t}\,\langle \bar{f}_n f_m \rangle_0 \ , \tag{131}$$

it can be learned that these conditions are fulfilled in case of $\lambda_m = \lambda_n$ and a finite or zero initial value $\langle \bar{f}_n f_m \rangle_0$, or if either $\Im\,(\lambda_m - \lambda_n) < 0$ or $\langle \bar{f}_n f_m \rangle_0 = 0$. These three are the only possibilities, as highlighted by the following distinction of cases.

- $\lambda_m - \lambda_n = 0$:
  $\lim\limits_{t\to\infty} \langle \bar{f}_n f_m \rangle_t = \langle \bar{f}_n f_m \rangle_0$

- $\Re(\lambda_m - \lambda_n) = 0$ and $\Im(\lambda_m - \lambda_n) \neq 0$:
  $$\lim_{t\to\infty} \langle \bar{f}_n f_m \rangle_t = \begin{cases} \infty\,, & \Im(\lambda_m - \lambda_n) > 0 \quad \text{and} \quad \langle \bar{f}_n f_m \rangle_0 \neq 0 \\ 0\,, & \Im(\lambda_m - \lambda_n) < 0 \quad \text{or} \quad \langle \bar{f}_n f_m \rangle_0 = 0 \end{cases}$$

- $\Re(\lambda_m - \lambda_n) \neq 0$ and $\Im(\lambda_m - \lambda_n) = 0$:
  $$\lim_{t\to\infty} \langle \bar{f}_n f_m \rangle_t = \begin{cases} \text{not existing}\,, & \langle \bar{f}_n f_m \rangle_0 \neq 0 \\ 0\,, & \langle \bar{f}_n f_m \rangle_0 = 0 \end{cases}$$

- $\Re(\lambda_m - \lambda_n) \neq 0$ and $\Im(\lambda_m - \lambda_n) \neq 0$:
  $$\lim_{t\to\infty} \langle \bar{f}_n f_m \rangle_t = \begin{cases} \infty\,, & \Im(\lambda_m - \lambda_n) > 0 \quad \text{and} \quad \langle \bar{f}_n f_m \rangle_0 \neq 0 \\ 0\,, & \Im(\lambda_m - \lambda_n) < 0 \quad \text{or} \quad \langle \bar{f}_n f_m \rangle_0 = 0 \end{cases}$$

If a steady state exists, expectation values $\langle \bar{f}_n f_m \rangle_t$ corresponding to different eigenvalues, $\lambda_m - \lambda_n \neq 0$, are either identical to zero or they decay to zero with $t \to \infty$. $\langle \bar{f}_n f_m \rangle_t$ and $\langle \bar{f}_m f_n \rangle_t$ cannot both be of the decaying type, because the eigenvalues contribute with opposite signs. If one of them occurs, the other must be identical to zero.
In the steady state only expectation values $\langle \bar{f}_n f_m \rangle_\infty$ corresponding to equal eigenvalues, $\lambda_n = \lambda_m$, are nonzero. If the eigenvalues are nondegenerate, this means that only $\langle \bar{f}_n f_n \rangle_\infty$ are finite and thus contribute to the expectation values of general system operators.

Since in case of an existing steady state, $\lambda_n \neq \lambda_m$ and $\langle \bar{f}_n f_m \rangle_0 \neq 0$ the imaginary part contained in the exponential (131) has to be negative, it is reasonable to carry out a particle-hole transformation, such that all super energies have a negative imaginary part:

$$f'_n = \begin{cases} f_n & \Im\lambda_n < 0 \\ \bar{f}_n & \Im\lambda_n > 0 \end{cases} \qquad \lambda'_n = -\lambda_n \operatorname{sgn}\Im\lambda_n = \begin{cases} \lambda_n & \Im\lambda_n < 0 \\ -\lambda_n & \Im\lambda_n > 0 \end{cases} \tag{132}$$

From eq. (114) and (117) follows immediately $\{\bar{f}'_n, f'_n\} = \mathbb{1}$. Inserting the new operators and super energies, eq. (132), into eq. (101) and using this property yields

$$\hat{L} = \sum_n \lambda'_n \bar{f}'_n f'_n + C'\mathbb{1} \,, \qquad C' = C + \sum_{n|\Im\lambda_n>0} \lambda_n \,. \tag{133}$$

In the following $|0_{f'}\rangle$ denotes the vacuum for the f' operators. Thus it fulfills $f'_n |0_{f'}\rangle = 0$. The time evolution of this state is determined by eq. (30) with the Liouvillian (133),

$$\begin{aligned} i\frac{d}{dt}|0_{f'}\rangle &= C'|0_{f'}\rangle \,, \\ |0_{f'}\rangle_t &= e^{-i\Re C' t} e^{\Im C' t} |0_{f'}\rangle_0 \,. \end{aligned} \tag{134}$$

If a steady state exists, either $C' \equiv 0$ or $\Im C' < 0$ has to be fulfilled. In fact, $C' = 0$ is valid, as demonstrated in sec. 7.4. Therefore the f' vacuum is constant in time. The time evolution of a state with one f' particle is given by

$$\begin{aligned} i\frac{d}{dt}\bar{f}'_n |0_{f'}\rangle &= \kappa \lambda'_n \bar{f}'_n |0_{f'}\rangle \,, \\ \bar{f}'_n |0_{f'}\rangle_t &= e^{-i\kappa\Re\lambda'_n t} e^{\kappa\Im\lambda'_n t} \bar{f}'_n |0_{f'}\rangle_0 \,, \\ &\underset{t\to\infty}{\longrightarrow} 0 \,. \end{aligned} \tag{135}$$

The calculation has been transferred to sec. 7.5. The amplitude of the state decays exponentially to zero with $t \to \infty$, since $\Im\lambda'_n < 0$. This also holds for states with more than one f' particles, see sec. 7.5. Therefore the f' vacuum is the steady state,

$$|\rho_\infty\rangle = |0_{f'}\rangle \,. \tag{136}$$

Expectation values of eigenmode operators in the steady state, $\langle \bar{f}_n f_m \rangle_\infty$, can be calculated with the knowledge that for nondegenerate eigenvalues only diagonal terms, $n = m$, survive and by transforming to the f' operators and exploiting the vacuum property, $f'_n |\rho_\infty\rangle = 0$:

$$\begin{aligned} \langle \bar{f}_n f_m \rangle_\infty &= \delta_{nm} \langle \bar{f}_n f_n \rangle_\infty \\ &= \delta_{nm} \begin{cases} \langle I|\bar{f}'_n f'_n|\rho_\infty\rangle = 0 & \Im\lambda_n < 0 \\ \langle I|f'_n \bar{f}'_n|\rho_\infty\rangle = \langle I|\mathbb{1} - \bar{f}'_n f'_n|\rho_\infty\rangle = 1 & \Im\lambda_n > 0 \end{cases} \\ &= \delta_{nm}\,\Theta\left(\Im(\lambda_n)\right) \\ &\equiv D^{>}_{nm} \end{aligned} \tag{137}$$

In the second line also the anticommutation relation, $\{\bar{f}'_n, f'_n\} = \mathbb{1}$, has been used and $\langle I|\rho\rangle = 1$, see sec. 2.3. According to eq. (137), only those eigenmode operators that correspond to eigenvalues with a positive imaginary part contribute. With eq. (122) follows that expectation values

of quadratic operators $\langle b_r^\dagger b_s \rangle$ in the steady state are determined by

$$\begin{aligned} \langle b_r^\dagger b_s \rangle_\infty &= \sum_{nm} \left(\boldsymbol{R}^\dagger \right)_{sq} U_{qm} \langle \bar{f}_n f_m \rangle_\infty V_{np} R_{pr} \\ &= \left(\boldsymbol{R}^\dagger \boldsymbol{U} \boldsymbol{D}^> \boldsymbol{V} \boldsymbol{R} \right)_{sr} . \end{aligned} \tag{138}$$

The retarded Green's function for the b operators in the steady state is defined as

$$G_{rs}^R(t) = -i\, \Theta(t)\, \langle I \,|\, \{b_r(t), b_s^\dagger\} \,|\, \rho_\infty \rangle , \qquad G_{rs}^R(\omega) = \int dt\, e^{i\omega t} G_{rs}^R(t) . \tag{139}$$

The calculation of $\boldsymbol{G}^R(\omega)$ for the normal noninteracting system is presented in detail in [10] and can be taken from this source. To make it valid also for a generalized system, an additional factor κ, eq. (125), has to be introduced, analogous to the time evolution. The result is

$$\boldsymbol{G}^R(\omega) = \boldsymbol{U} \frac{\boldsymbol{D}^<}{\omega \mathbb{1} - \kappa \boldsymbol{D}} \boldsymbol{V} - \left(\boldsymbol{U} \frac{\boldsymbol{D}^>}{\omega \mathbb{1} - \kappa \boldsymbol{D}} \boldsymbol{V} \right)^\dagger , \tag{140}$$

with the definition

$$D_{nm}^< = \delta_{nm} - D_{nm}^> . \tag{141}$$

The spectral function is calculated from eq. (140), according to

$$\boldsymbol{A}(\omega) = -\frac{1}{\pi} \Im \boldsymbol{G}^R(\omega) . \tag{142}$$

Note that the calculation of the steady state presented in this subsection is only valid, if the coefficients of the Liouville matrix $\boldsymbol{L'}$ ($\boldsymbol{L''}$) are constants and thus depend neither on time nor on the density operator, the same requirements as for the time evolution in sec. 4.2.1.

5 Results

In the first subsection 5.1 the simulation results for a simple model are presented, in order to give an impression of the consequences that a coupling to the environment exerts on a quantum system and to make some general remarks. Sec. 5.2 presents a model for the leads and a way to apply a bias voltage between them. The results are used to represent the leads in the following subsections. Sec. 5.3 shows the simulation results for the Su-Schrieffer-Heeger Model and sec. 5.4 those for a two-dimensional extension of this model. In sec. 5.5 the Kitaev Model is studied and in sec. 5.6 a time dependent extension of the Kitaev Model. The presented results are original contributions from this thesis.

5.1 A first simulation and the impact of the dissipation parameters Γ

For a first study of the impact that the $\mathbf{\Gamma}$ matrices exert on a system, a simple and well known model, the one-dimensional tight binding model is used. This model is the basis for both systems I aim to study in the end: It emerges as a limiting case in the Su-Schrieffer-Heeger Model (41) for $\delta = 0$ and also in the Kitaev Model (54) for $\Delta = 0$. Its hamiltonian reads,

$$\hat{H} = \epsilon \sum_{n=1}^{N} c_n^\dagger c_n + t \sum_{n=1}^{N-1} \left(c_n^\dagger c_{n+1} + h.c. \right) , \tag{143}$$

with nearest neighbor hopping strength t and on-site energy ϵ.
I chose one Lindblad dissipator coupled to the first site of the chain that introduces particles into the system with rate $\Gamma^{(+)}$ and a second dissipator extracting particles at the last site of the chain with rate $\Gamma^{(-)}$. The matrices $\mathbf{\Gamma}^{(\pm)}$ read in this case

$$\mathbf{\Gamma}^{(+)} = \begin{pmatrix} \Gamma^{(+)} & \mathbf{0} \\ \mathbf{0} & \mathbf{0} \end{pmatrix} , \qquad \mathbf{\Gamma}^{(-)} = \begin{pmatrix} \mathbf{0} & \mathbf{0} \\ \mathbf{0} & \Gamma^{(-)} \end{pmatrix} . \tag{144}$$

This simple setup already drives the system out of equilibrium. It is the first approximation of a bias voltage applied. Obviously, the result is a particle current passing through the system from the left to the right. Fig. (6) shows a picture of this setup.

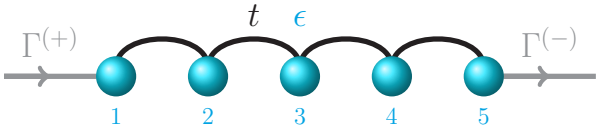

Figure 6: Tight binding Model with a single dissipator at each end. $\Gamma^{(+)}$ and $\Gamma^{(-)}$ are the rates with which electrons are created and destroyed at opposite ends of the chain, driving a particle current through the system from the left to the right.

In order to calculate this current and also the occupation numbers of the sites quantitatively, the coefficient matrix $\boldsymbol{h}$ is determined from eq. (143) and inserted together with $\mathbf{\Gamma}^{(+)}$, $\mathbf{\Gamma}^{(-)}$ from eq. (144) into the Liouville matrix $\boldsymbol{L''}$, eq. (93) with (80) and (81), which is then diagonalized. It is sufficient to do this for the $\boldsymbol{\alpha}$ block only, see eq. (187), and use eq. (106) - (110) to determine the result for the whole matrix $\boldsymbol{L''}$. From eq. (128) and (138) the time evolution and the steady state for the expectation values $\langle b_r^\dagger b_s \rangle$ from eq. (85) can be determined. For the time evolution an

initial state $\langle b_k^\dagger b_j \rangle_0$ is chosen first. More precisely, $\langle c_k^\dagger c_j \rangle_0 = \langle b_k^\dagger b_j \rangle_0 |_{j,k \in [1,N]}$ is chosen, the other expectation values are calculated from this. Then eq. (128) and (138) are applied to obtain the time evolution and the steady state. It is sufficient to evaluate these equations for $r, s \in [1, N]$, again yielding $\langle b_r^\dagger b_s \rangle |_{r,s \in [1,N]} = \langle c_r^\dagger c_s \rangle = \rho_{rs}$, the single particle density matrix. The other indices do not hold additional information. The occupation numbers n_r can be read directly from $\boldsymbol{\rho}$, the current flowing on the bond between sites r and s, coupled by t, has to be calculated,

$$n_r = \langle c_r^\dagger c_r \rangle = \rho_{rr} \,, \tag{145}$$

$$J_{rs} = it \left(\langle c_r^\dagger c_s \rangle - \langle c_s^\dagger c_r \rangle \right) = -2t \, \Im \rho_{rs} \,. \tag{146}$$

Fig. 7 shows simulation results for $N = 5$ sites with the parameters $\epsilon = 0$ and $t = \Gamma^{(+)} = \Gamma^{(-)} = 1$. It has been assumed that initially each site is equally occupied, $\rho_{kj}(0) = N^{-1} \delta_{kj}$.

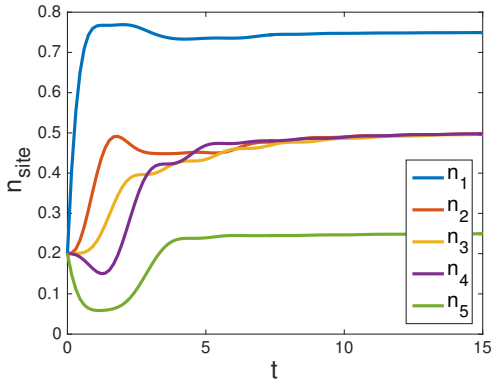

(a) Time evolution of the occupation number $n_r(t)$.

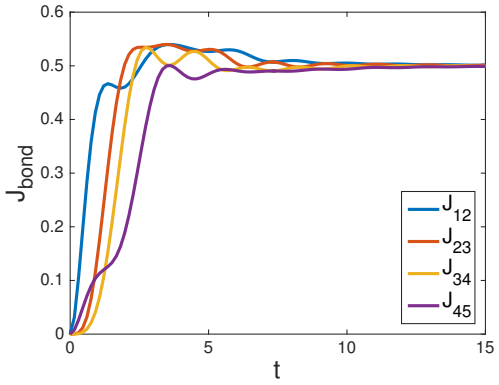

(b) Time evolution of the bond current $J_{rs}(t)$

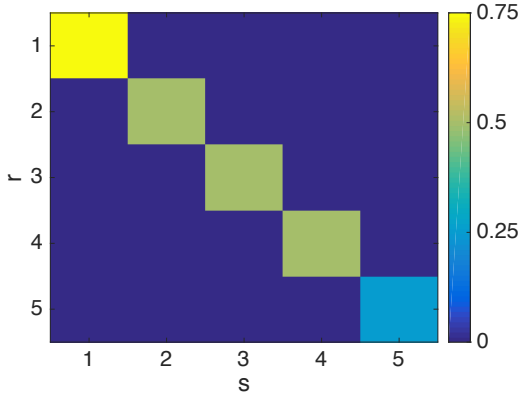

(c) Single particle density matrix in steady state: $\Re \rho_{rs}$

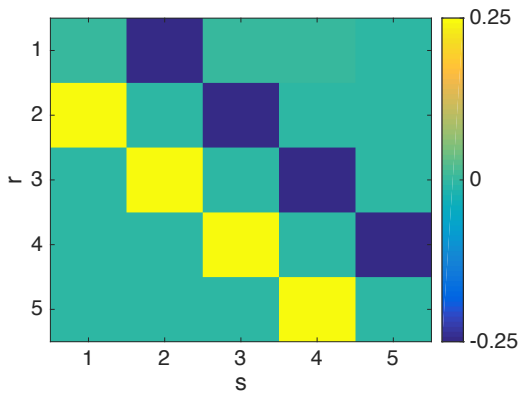

(d) Single particle density matrix in steady state: $\Im \rho_{rs}$. This yields the current $J_{bond} = 0.5$, according to (146).

Figure 7: Simulation results for the tight binding model coupled to two dissipators, according to fig. 6, with $N = 5$ sites, $\epsilon = 0$ and $t = \Gamma^{(+)} = \Gamma^{(-)} = 1$. (a) and (b) show the time evolution of the occupation number and the bond current. (c) and (d) show the real and imaginary part of the single particle density matrix in the steady state. The indices r, s denote system sites, the color indicates the value of $\Re \rho_{rs}$ or $\Im \rho_{rs}$, according to the legend.

In fig. 7(a) and 7(b) the time evolution of the occupation of each site and the bond currents between two sites are plotted. For small times the system shows transient behavior. Site 5 is directly coupled to the dissipator extracting electrons from the system. This happens at a con-

stant rate $\Gamma^{(-)}$. The system is initially in equilibrium with an equal occupation, insufficient to satisfy the demand for electrons after a short time. The particles have to be drawn from the adjacent sites to the left and ultimately from the dissipator coupled to site 1, which is pumping in electrons with rate $\Gamma^{(+)}$. Injected into the system, they are driven by the difference in occupation between adjacent lattice sites and their velocity is bounded by the hopping strength t. They need time to traverse the system. Therefore it takes time for the last site to be resupplied again. For this reason the occupations of the last and also the next to last site, n_5 and n_4, decrease before increasing again. The first two sites, in contrast, are essentially filled from the beginning. The reaction of the interior sites on the Γ - parameters is less distinct, as there is no direct coupling. This can also be observed from the bond currents. For small simulation times the currents flowing at the edge bonds are larger than the interior currents.
After a settling time of $t \simeq 12$ a steady state is reached, where these quantities do not depend on time anymore. The most important result is that in the steady state each bond carries the same current. Thus Kirchhoff's point rule is fulfilled, which was not the case during the transient. Furthermore all interior sites have the same occupation n_k. It differs from the occupation of the edge sites that are coupled directly to the Lindblad dissipators, $n_1 > n_k > n_N$. The results are sustained by the figures 7(c) and 7(d), which show the whole single particle density matrix in the steady state, calculated from eq. (138). The described properties are generally inherent in a tight binding system as shown by fig. 6 for $N \geq 3$ sites, with one exception: If more sites involved, it takes the system more time to overcome the transient and reach the steady state.
The dynamics and the steady state of the system are governed by the eigenvalues of the Liouvillian. Fig. (8) shows the eigenvalues λ_n corresponding to the discussed results, before the particle-hole transformation is applied. The eigenvalues are complex, since the Liouvillian is

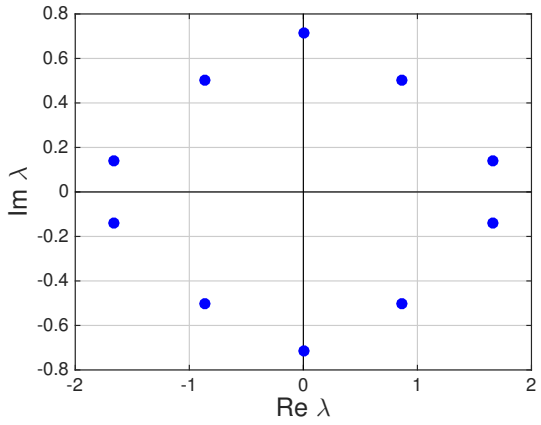

Figure 8: Eigenvalues of the Liouvillian for the tight binding model coupled to two dissipators, according to fig. 6, with $N = 5$ sites, $\epsilon = 0$ and $t = \Gamma^{(+)} = \Gamma^{(-)} = 1$. The figure shows the real and imaginary parts of the eigenvalues λ_n, according to eq. (101), before the particle-hole transformation, eq. (132).

not hermitian. They generally appear in complex conjugated pairs, irrespective of the model studied, see eq. (108). Thus they lie symmetric with respect to the real axis. For this special system they are also symmetric with respect to the imaginary axis. Since the eigenvalues are complex, the corresponding eigenmodes don't only pick up a phase with proceeding time, as in a closed system described by a hermitian Liouvillian with real eigenvalues, but they are also subject to a dampening. Eq. (131) shows that $\Re\lambda_n$ causes a phase change and $\Im\lambda_n$ is responsible for the dampening. From the imaginary part of the eigenvalues it is possible to estimate the simulation time until the steady state is reached with a certain accuracy. After the time $\tau = |\kappa\Im\lambda_n|^{-1}$, with κ from eq. (125), the amplitude of the n-th eigenmode is decayed by a factor e^{-1}, compare

eq. (131). Thus the eigenvalue with the smallest imaginary part determines the necessary simulation time. This time scales with the number of sites N.
Finally, the dependence of the steady state on the parameters $\Gamma^{(+)}$ and $\Gamma^{(-)}$ is studied. Fig. 9(a) shows the occupation numbers and the bond current, if $\Gamma^{(+)}$ and $\Gamma^{(-)}$ increase symmetrically from zero. This figure does not hold any surprises. As expected, the first site is filled with increasing $\Gamma^{(+)}$ and the last site emptied with increasing $\Gamma^{(-)}$. The occupation in between remains constant, since the rates change symmetrically. The current has a maximum at $\Gamma^{(+)} = \Gamma^{(-)} = t$ and vanishes for very small and large rates. The behavior of the system is much more interesting, if $\Gamma^{(+)}$ and $\Gamma^{(-)}$ change independently, as shown in fig. 9(b) and 9(c). If $\Gamma^{(+)}$ is large in comparison to the other parameters, $\Gamma^{(-)}$ and t, site 1 is filled with electrons, as expected. Furthermore the last and the interior sites are emptied, which is not immediately plausible. The reason for this is the loss of coherence: Site 1 is decoupled from the rest of the chain, leaving back a system, where only $\Gamma^{(-)}$ is acting. A similar behavior can be observed for large $\Gamma^{(-)}$. In this case the last site is decoupled from the system, yielding $n_N \to 0$ and $n_1, n_k \to 1$.

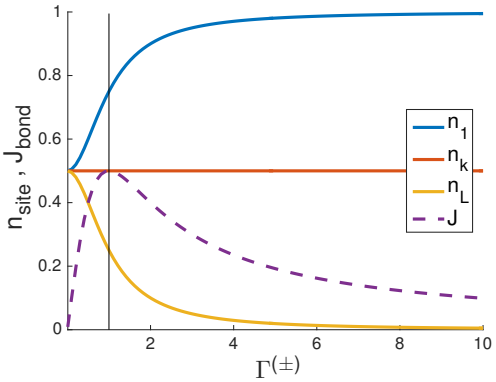

(a) $\Gamma^{(\pm)}$ dependence.

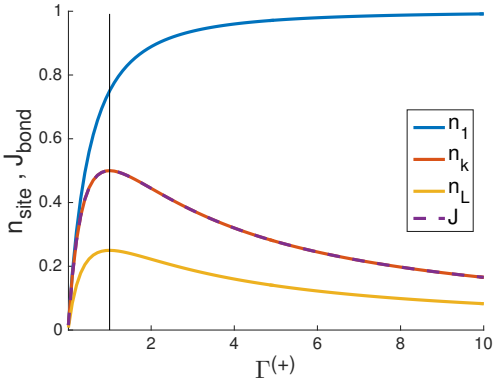

(b) $\Gamma^{(+)}$ dependence.

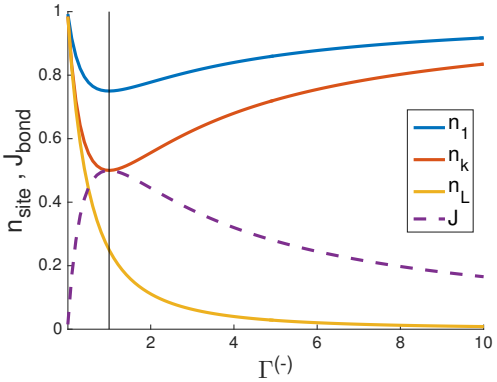

(c) $\Gamma^{(-)}$ dependence.

Figure 9: Steady state occupation numbers and bond current for the tight binding model coupled to two dissipators, according to fig. 6 for $\epsilon = 0$, $t = 1$. The figures show the dependence of these quantities on (a) $\Gamma^{(+)} = \Gamma^{(-)}$, (b) $\Gamma^{(+)}$ for $\Gamma^{(-)} = 1$ and (c) $\Gamma^{(-)}$ for $\Gamma^{(+)} = 1$.

All results in this subsection have been achieved through diagonalization of the Liouville matrix. Alternatively, the time evolution could be determined by solving the set of equations (129) with a Runge-Kutta scheme, see sec. 4.2.2. If the Liouvillian is non-interacting and independent of the system's state and of time, the diagonalization method is more efficient. Dealing with a time dependent problem, the Runge-Kutta scheme is better suited.

5.2 Buffer model for the leads

The final goal of this section is to study the transport properties of several different quantum systems connected to two electronic leads, where a bias voltage is applied. In the previous subsection the system has been biased with a single and constant pump rate $\Gamma^{(\pm)}$ at each end, which is a rather poor approximation. A more realistic situation can be established following the suggestion in [9] and [10], where the leads are modeled by a number of bath sites coupled to a Markovian environment, which is created by a set of Lindblad dissipators. The setup is illustrated in fig. 10.

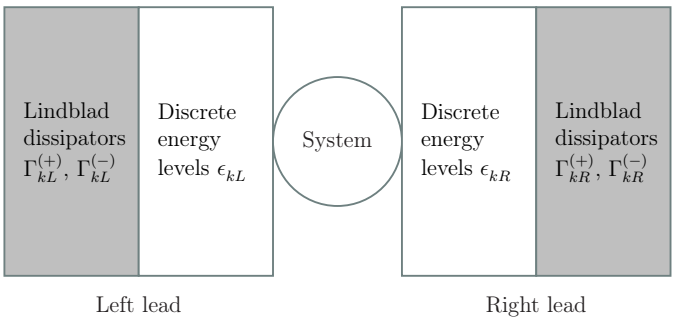

Figure 10: Sketch of a system connected to two leads, adapted from [9]. In this model each lead is partitioned into a number of bath sites that couple directly to the system and a Markovian environment, generated by Lindblad dissipators. The representation can be improved with increasing number of bath sites.

The system of interest and the bath sites together form a central region that is characterized in terms of a hamiltonian. The general structure of this hamiltonian is

$$\hat{H} = \hat{H}_S + \sum_{k,\alpha=L,R} \epsilon_{k\alpha} c^\dagger_{k\alpha} c_{k\alpha} + \sum_{n,k,\alpha=L,R} \left(t_{nk\alpha} c^\dagger_{k\alpha} c_n + h.c. \right) . \tag{147}$$

The first summand describes the system, the second one the bath sites and the last summand their coupling to the system. $c^\dagger_{k\alpha}$ and $c_{k\alpha}$ creates and destroys an electron at site k in lead α. $c^\dagger_n$ and c_n are the creation and annihilation operators in the system. The bath sites have on-site energies $\epsilon_{k\alpha}$ and their coupling to the system is described by the hopping strengths $t_{nk\alpha}$.
Each bath site is furthermore coupled to two Lindblad dissipators that introduce and extract electrons with the rates $\Gamma^{(+)}_{k\alpha}$ and $\Gamma^{(-)}_{k\alpha}$. In order to faithfully describe the leads, these rates must depend on the occupation of the energy levels $\epsilon_{k\alpha}$, since electrons can only be introduced to an empty site and extracted from a filled one. For disconnected leads in thermodynamic equilibrium these occupation numbers are determined by the Fermi function and the rates can be represented as

$$\begin{aligned} \Gamma^{(+)}_{k\alpha} &= \gamma_{k\alpha} f_{k\alpha} , \\ \Gamma^{(-)}_{k\alpha} &= \gamma_{k\alpha} \left(1 - f_{k\alpha} \right) , \end{aligned} \qquad f_{k\alpha} = \left[1 + \exp\left(\frac{\epsilon_{k\alpha} - \mu_\alpha}{T_\alpha} \right) \right]^{-1} . \tag{148}$$

T_α and μ_α are the temperature and the chemical potential in lead α. The parameters $\gamma_{k\alpha}$ are again constant rates. Perfect leads are infinitely large electron reservoirs that nearly stay in equilibrium when coupled to the system. Therefore the Fermi distribution and the rates in eq. (148) are kept in this case. In this setup a current can be driven through the system by shifting the chemical potential and/or the temperature in one lead with respect to the other one.
Prior to this simulation the parameters $\gamma_{k\alpha}$, $\epsilon_{k\alpha}$ and $t_{nk\alpha}$ have to be determined for each lead. It is

assumed that both leads are identical and each bath site couples only to a single adjacent system site. Thus the considerations are confined to the left lead coupled to site 1 of the system and the indices α and n are dropped. The lead is characterized by its retarded hybridization function $\Delta(\omega)$. For the considered "star configuration" it reads

$$\Delta(\omega) = \sum_k t_k^2 \, g_k(\omega) \,, \qquad g_k(\omega) = \frac{1}{\omega - \epsilon_k + i\,\gamma_k} \,. \tag{149}$$

$g_k(\omega)$ is the retarded Green's function of bath site k in the disconnected lead. It has been assumed that the hoppings t_k are real. If they are furthermore identical, $t_k = t'$, the imaginary part of the hybridization function is proportional to the density of states in the lead $D(\omega)$,

$$D(\omega) \propto -\frac{1}{\pi}\Im\Delta(\omega) = \frac{1}{\pi}\sum_k t_k^2 \frac{\gamma_k}{(\omega-\epsilon_k)^2 + \gamma_k^2} \,. \tag{150}$$

Eq. (150) describes a sum of Lorentzians, centered at $\omega = \epsilon_k$, each with a prefactor t_k^2, yielding a peak height of t_k^2/γ_k. The width of the peaks is determined by γ_k.
The purpose of the discussed auxiliary system, consisting of the bath sites and the Lindblad dissipators, is to faithfully represent real physical leads. Given the exact hybridization function of a physical lead $\Delta_{ex}(\omega)$, the parameters t_k, γ_k and ϵ_k are determined through a fit of $\Im\Delta_{ex}(\omega)$ with $\Im\Delta(\omega)$ from eq. (150). Considering all t_k, γ_k, ϵ_k as fit parameters limits the model to a small number of bath sites, in order for the calculation to be feasible in practice. By imposing further constraints on the parameters the number of bath sites may be raised and thus the quality of the representation. In the following it is shown, how this can be done in detail.
For a first study the hoppings are assumed to be identical, $t_k = t'$. Furthermore $\Im\Delta_{ex}(\omega)$ and thus the exact density of states $D_{ex}(\omega)$ are assumed to be constant within the bandwidth $\omega \in [-W, W]$ and zero outside. If the energies ϵ_k are evenly spaced within this bandwidth, it is reasonable

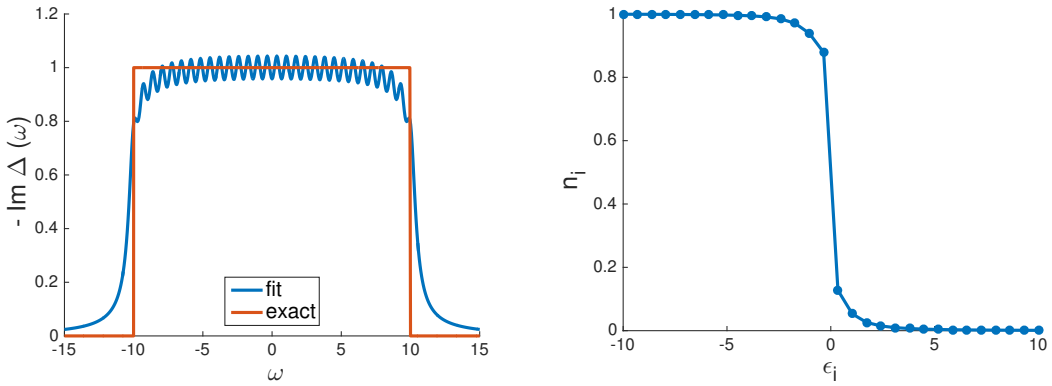

(a) Hybridization function.

(b) Occupation of the bath sites.

Figure 11: Fit results for evenly spaced bath site energies. (a) shows the quality of the representation of the exact hybridization function $\Delta_{ex}(\omega)$ by the modeled one $\Delta(\omega)$, eq. (150), with only two fit parameters, t' and γ'. (b) shows the resulting steady state occupation of the bath sites when the lead is coupled to a single site with on-site energy $\epsilon = \mu = 0$. The choice of parameters is explained in the running text.

to take all $\gamma_k = \gamma'$ identical, too, as they determine the Lorentzians' widths. This leaves two parameters, t' and γ', to determine, e.g. by minimizing the quadratic deviation of $\Im\Delta(\omega)$ from $\Im\Delta_{ex}(\omega)$. Fig. 11(a) shows the fit result for $N_B = 30$ bath sites representing a constant hy-

bridization $\Gamma = -\Im\Delta_{ex}(\omega) = 1$ within the bandwidth $[-10, 10]$. In fig. 11(b) the steady state occupation of the bath sites is plotted, when they are coupled to a single system site with on-site energy $\epsilon = 0$. The chemical potential and the temperature in the lead are chosen as $\mu = 0$ and $T = 0$. In the case of ideal leads, the occupation would reproduce the Fermi function, which is a step function at $T = 0$. As the leads are not perfect, the Fermi function is only approximately reproduced. Around $\epsilon = \mu$ it varies most, thus the plotted scenario shows the worst case. The result can be improved by using more bath sites and/or a tighter ϵ_k - spacing around zero.
The latter can be managed by using logarithmically spaced ϵ_k that accumulate around zero. It is reasonable to assume that the other parameters space in energy distances $\delta\epsilon_k$ of neighboring ϵ_k, according to $t_k = t' \sqrt{\delta\epsilon_k}$ and $\gamma_k = \gamma' \delta\epsilon_k$. This way the height of the individually observed Lorentz peaks in eq. (150) is t'^2/γ' and thus constant for all energy levels. Furthermore the width of the peaks increases the farther they are separated from each other, compensating for the sparse arrangement outside the region around zero. Fig. 12 shows the fit results achieved with

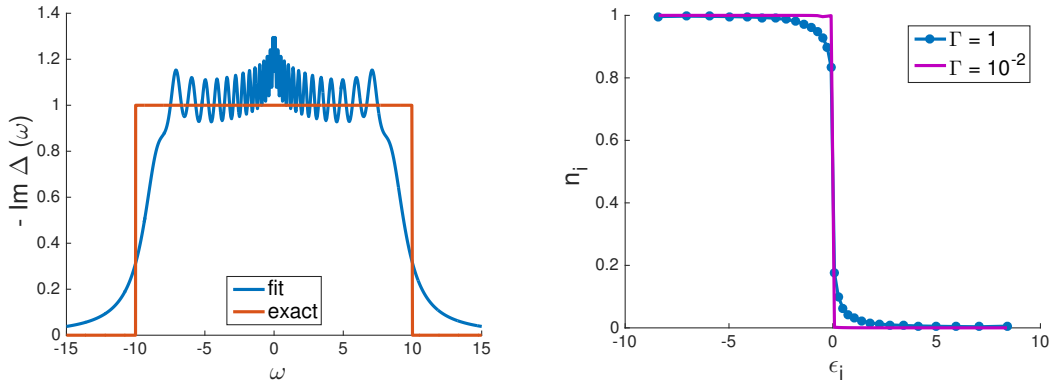

(a) Hybridization function.

(b) Occupation of the bath sites.

Figure 12: Fit results for logarithmically spaced bath site energies. (a) shows again the quality of the representation of the exact hybridization function $\Delta_{ex}(\omega)$ by the modeled one $\Delta(\omega)$, eq. (150), with fit parameters t' and γ'.(b) shows the resulting steady state occupation of the bath sites when the lead is coupled to a single site with $\epsilon = \mu = 0$ for different hybridizations.

this method. The parameters are the same as before, except for ϵ_k, t_k and γ_k. In fig. 12(a) the hybridization function is less well represented as before in fig. 11(a). If the exclusive goal had been the achievement of the best fit result for $\Im\Delta(\omega)$, this method would be not so appropriate. In that case it would be advantageous to take a high energy resolution at the band's edges $\pm W$ to represent them well and larger energy spacings in the center. But the occupation resulting from the fit is also very important. For the occupation the region around μ is crucial and should have the highest point density. By comparison of the blue curve in fig. 12(b) with fig. 11(b), it can be observed that the Fermi function is better reproduced using a logarithmic energy spacing. An even better result can be obtained by additionally reducing the coupling of the lead to the system site which means reducing the hybridization. The purple curve in fig. 12(b) shows the bath's occupation, if the hybridization is reduced by a factor of 100 with respect to the hybridization yielding the blue curve. This transformation, $\Gamma \to \frac{\Gamma}{100}$, is equivalent to $t' \to \frac{t'}{10}$.
Since this thesis is concerned about systems that exhibit edge states at low energies, their behavior at low voltages is especially interesting. Low voltages are associated with a high sensitivity at the leads' Fermi edges. Thus the shortcomings of the second method regarding the representation of the hybridization function will be less weighted and the decision is made in favor of the Fermi function and the logarithmically spaced points.

In the following simulations the modeled leads are coupled to the system, according to eq. (147). Their temperature is kept constant at $T = 0$. A bias voltage V_B is applied by shifting the chemical potential and the on-site energies of the bath sites in one lead with respect to the other one. If not stated otherwise, the effect of the voltage is divided evenly onto both leads, resulting in

$$\begin{pmatrix}\mu_L\\ \epsilon_{kL}\end{pmatrix} \rightarrow \begin{pmatrix}0\\ \epsilon_k\end{pmatrix} + \frac{V_B}{2}\,, \qquad \begin{pmatrix}\mu_R\\ \epsilon_{kR}\end{pmatrix} \rightarrow \begin{pmatrix}0\\ \epsilon_k\end{pmatrix} - \frac{V_B}{2}\,. \tag{151}$$

Other realizations are possible. It is sufficient that the chemical potentials in the leads differ by V_B. If e.g. the right lead is fixed, V_B exerts its influence exclusively on the left lead, yielding

$$\begin{pmatrix}\mu_L\\ \epsilon_{kL}\end{pmatrix} \rightarrow \begin{pmatrix}0\\ \epsilon_k\end{pmatrix} + V_B\,, \qquad \begin{pmatrix}\mu_R\\ \epsilon_{kR}\end{pmatrix} \rightarrow \begin{pmatrix}0\\ \epsilon_k\end{pmatrix}. \tag{152}$$

The bias voltage drives a current through the system. The current on a bond between two system sites coupled by t is calculated with eq. (146). Different realizations of V_B end in different simulation results.

5.3 Su-Schrieffer-Heeger Model

In this subsection the transport properties of the Su-Schrieffer-Heeger Model, eq. (41), are examined in both phases and at the phase transition. The results are presented in terms of the parameters $t_A := t + \delta$ and $t_B := t - \delta$.
The leads are modeled by $N_B = 100$ bath sites with a logarithmic energy spacing representing a constant hybridization $\Gamma = 10^{-2}$ on $[-30, 30]$. They are coupled to opposite edge sites of a wire with $N = 80$ sites. A bias voltage V_B is applied symmetrically, according to eq. (151), driving a current through the system.
The main simulation results in the steady state are presented in fig. 13. The left column shows the current between adjacent system sites in dependence of the bias voltage for $t_B = 1$ and different values of $t_A > 0$, associated with different phases. The right column shows the trace, the sum over all sites, of the local spectral function of the wire corresponding to one of the curves to the left at $V_B = 1$.
In the topological phase, defined by $t_A < t_B$, the current starts to rise at a certain threshold voltage $V_T > 0$, as demonstrated in fig. 13(a). The threshold voltage decreases with increasing t_A and approximates zero for $t_A \lesssim t_B$. This behavior can be understood by studying the spectral function. Fig. 13(b) shows the local spectral function of the wire for $t_A = 0.3$, summed over all sites. The peak centered at $\omega = 0$ corresponds to the edge states that arise in the topological phase. They are localized at the edges of the wire and decay to zero into the bulk. This is demonstrated in fig. 14. Because of this property these states are not able to carry a current along the wire. An electron can move from one site to another one, if the sites are coupled by a finite hopping strength and if the target site hosts a state at the same energy that the electron can occupy. In order to drive a current along the wire, states are necessary that extend over the whole bulk. There are no such states at $\omega \simeq 0$, the next states with a finite weight within the bulk lie at $\omega \simeq \pm 0.71$. Therefore the size of the bulk gap is $\Delta_I \simeq 1.42$. Only electrons with a high enough energy to overcome the bulk gap can cross the wire and contribute to a current. The necessary energy can be acquired from a bias voltage. As the occupation in the leads is nearly a step function and the voltage is applied symmetrically, electrons from one lead can overcome the gap, cross the system and vanish into the other lead for $V_B \geq \Delta_I$. This defines the threshold voltage as $V_T = \Delta_I$. By comparison with fig. 13(a) it can be learned that the current for $t_A = 0.3$

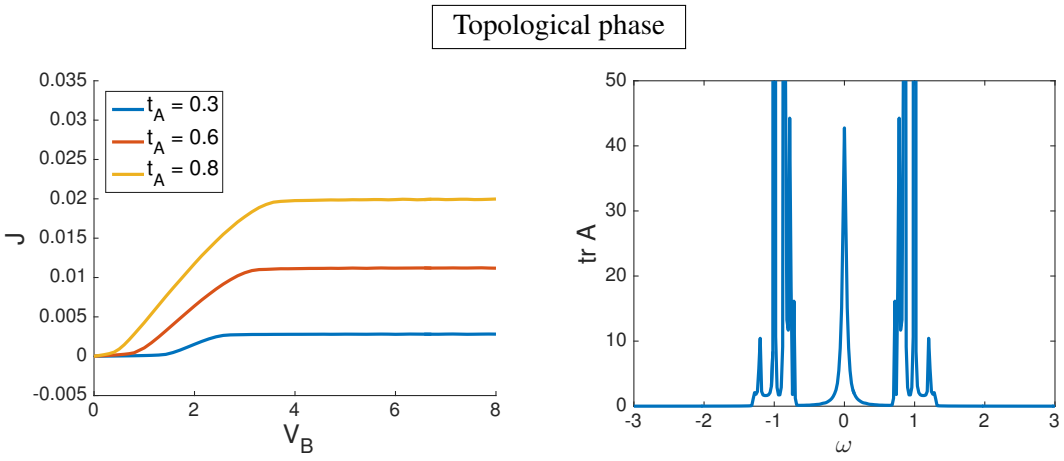

(a) Current voltage characteristic. (b) Spectral function for $t_A = 0.3$.

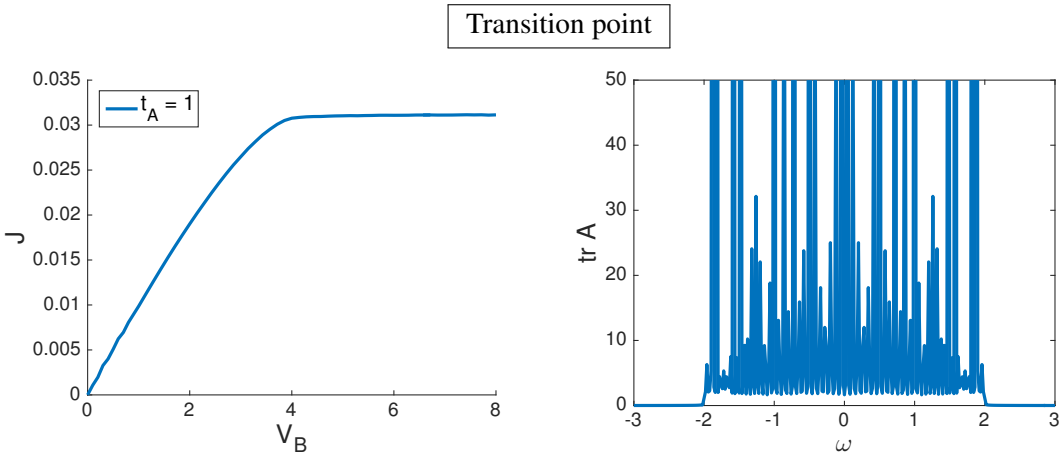

(c) Current voltage characteristic. (d) Spectral function.

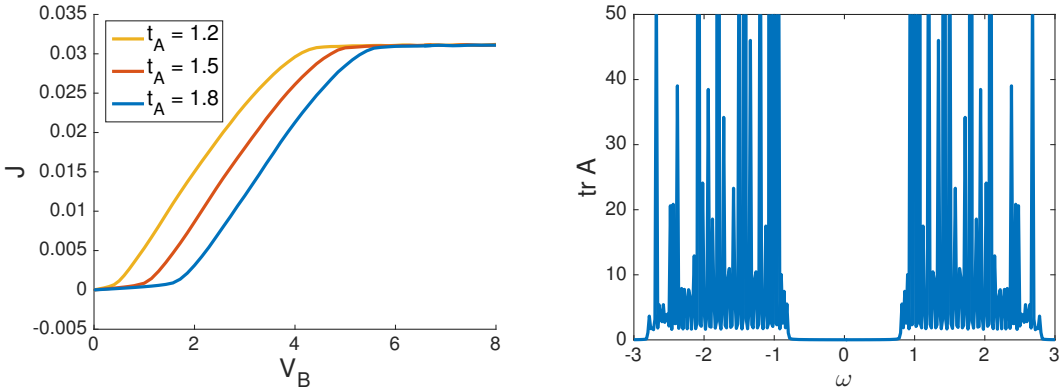

(e) Current voltage characteristic. (f) Spectral function for $t_A = 1.8$.

Figure 13: Phase diagram of the Su-Schrieffer-Heeger Model in the steady state, showing the current voltage characteristics and the spectral functions. The hopping $t_B = 1$ is fixed, the phase transition is made by varying t_A. The spectral functions are plotted at $V_B = 1$, which lies within the bulk gap for the studied parameters in both phases. The figures show the local spectral function of the wire summed over all sites (trace). The peak at $\omega = 0$ in the topological phase (b) is localized at the edges and vanishes in the bulk, which is demonstrated in fig. 14. The other modes extend over the bulk.

indeed starts to flow at $V_T = 1.42 = \Delta_I$. The threshold voltage decreases with increasing t_A in this phase, because the gap gets smaller. This is illustrated in fig. 15, which shows the gap size in dependence of t_A in both phases and at the phase transition. At a certain voltage V_S the current saturates. This can also be explained by having a look at the spectral function. Fig. 13(b) shows that for $|\omega| > 1.32$ no additional states are present. By increasing the bias voltage across this point no additional electrons can be hosted by the wire. Therefore the current is independent of V_B from then. Since the leads' occupation is nearly a step function and the voltage is applied symmetrically, this point is reached for $V_S \simeq 2.64$. This agrees with the saturation voltage that can be directly read from fig. 13(a) in the case of $t_A = 0.3$. V_S increases with increasing t_A, because the spectral function is broadened. The velocity of the electrons moving along the wire is bounded above by $\min(t_A, t_B)$. Therefore the strength of current is determined by the minimal hopping strength. In the topological phase this is t_A and therefore the saturation current also increases with increasing t_A, see fig. 13(a).

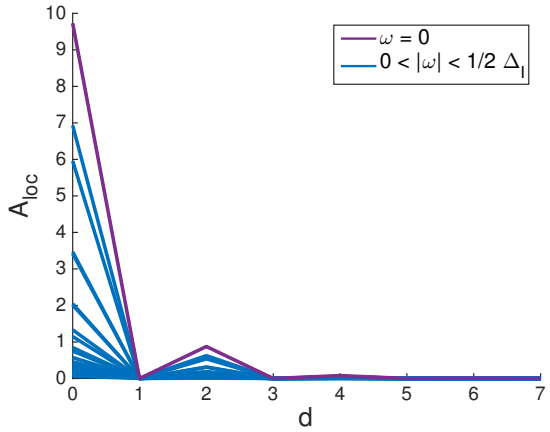

Figure 14: Local spectral function in the vicinity of the edges for different values of ω within the bulk gap at $V_B = 1$. d denotes the distance from the nearest edge site. The parameters $t_A = 0.3$, $t_B = 1$ correspond to the topological phase. Obviously only edge states are present at low energies. They have their maximum weight at $d = 0$ and $\omega = 0$ and decay to zero away from these parameters.

At $t_A = t_B$ a phase transition takes place. Fig. 13(d) shows the trace over the local spectral function of the wire for these parameters. There is no hint of an energy gap in this figure, but the figure lacks a spatial resolution. Further investigation shows that the states, also the low energy ones, extend over the whole wire including the edges. Thus the bulk gap is closed, $\Delta_I = 0$, and the edge states vanished, as demonstrated in equilibrium. Since there is no energy gap, the current in fig. 13(c) rises from zero voltage without a threshold. The current saturates at $V_S \simeq 4$, which corresponds to the extent of the spectral function in fig. 13(d). For these parameters the Su-Schrieffer-Heeger model is reduced to the ordinary tight binding model.
For $t_A > t_B$ the system is in the trivial phase. As can be seen from fig. 13(f) the spectrum is gapped again, but no edge states are present. This has also been demonstrated in equilibrium. For $t_A = 1.8$ the size of the gap is $\Delta_I = 1.64$, in agreement with fig. 13(e) showing a threshold voltage of $V_T = 1.64$. In this phase the threshold voltage increases with t_A, because the energy gap widens away from the transition point, according to fig. 15. The voltage V_S also increases with t_A, as the spectrum broadens. The saturation current is now independent of t_A, because its upper bound is determined by $\min(t_A, t_B) = t_B$ in this phase. Since t_B is fixed, the saturation current is constant.
As previously mentioned, the spectral functions have been calculated at $V_B = 1$. This yields electron energies that lie within the bulk gap for the discussed examples, $t_A = 0.3$ and $t_A = 1.8$,

and is therefore well suited to distinguish between the effects of edge and bulk modes. Further investigation shows that the spectral function does not change qualitatively with the bias voltage. The spectral functions have been used to determine the the bulk's energy gap for different t_A. The result is plotted in fig. 15 and compared with the equilibrium result.

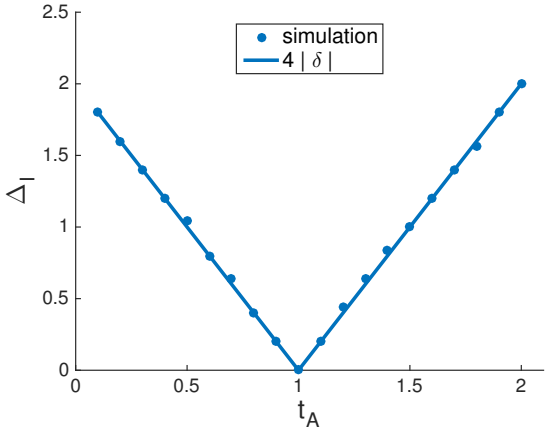

Figure 15: Bulk gap Δ_I in dependence of t_A for $t_B = 1$. The equilibrium result that the gap size equals $4|\delta| = 2|t_A - t_B|$, see eq. (47), is nicely fulfilled in the simulation. The values for Δ_I have been achieved from the corresponding spectral functions at $V_B = 1$, as explained in the running text.

If the number of system sites is raised above 80, the transport properties do not change qualitatively anymore. In fact this is already the case for smaller systems, from $N \gtrsim 40$.

5.4 Two-dimensional extension of the Su-Schrieffer-Heeger Model

In order to investigate the transport properties of the edge states that arise in the topological phase of the Su-Schrieffer-Heeger model, it is extended to two dimensions. Therefore N identical wires are arranged parallel to each other and each site of a wire is coupled to the corresponding sites in the adjacent wires with the hopping strength t_N. The setup is illustrated in fig. 16.

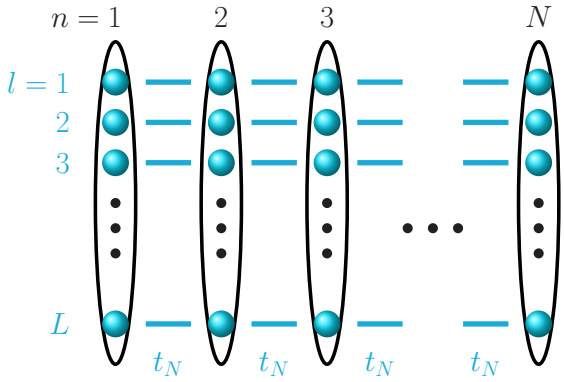

Figure 16: Two-dimensional array of N identical Su-Schrieffer-Heeger wires with length L, coupled to each other by a hopping strength t_N. The wire index is called n and the site index within a wire l. The left lead is connected to the wire $n = 1$ and the right lead to the wire N, such that all bath sites in a lead are connected to each site of the respective wire.

The leads are modeled by $N_B = 30$ bath sites with a logarithmic energy spacing fitting a constant hybridization of $\Gamma = 10^{-2}$ on $[-10, 10]$. The reduction of the number of bath sites in comparison to the one-dimensional case is necessary to limit the computational effort, because the system of interest itself consists of a larger number of sites. To still allow for a good covering of the energy band by the bath sites, the band width is reduced, too. The left lead is coupled to the first wire, the right lead to the last one and all bath sites within a lead are coupled to each site of the corresponding wire. In the one-dimensional case, in contrast, each lead has been coupled only to a single site.
The studied array holds $N = 40$ wires with $L = 40$ sites per wire. The wire index is denoted as $n = (1, \ldots, N)$ and the site index along the wire as $l = (1, \ldots, L)$. The choice of N and L is the result of the following considerations. If the horizontal bonds in fig. 16 are cut, this yields N isolated Su-Schrieffer-Heeger wires, whereas a cut of the vertical bonds yields L isolated ordinary tight-binding wires. The transport properties of both models, when individually studied, do not change qualitatively, when the number of sites is raised above 40. Of course, this can be different, when the additional couplings are turned on and the system is two-dimensional. Therefore it would be advantageous to study a larger system. In the one-dimensional Su-Schrieffer-Heeger model L should be large, in order to prevent the wave functions of edge states, which are located at opposite ends of the wire, from overlapping. Since the current is driven along the ordinary tight-binding chains, N should not be too small, either. The computational effort, unfortunately, prevents from calculating much larger systems with the presented method. A comparison with smaller systems suggests that the quality of the simulation results is not entirely converged in system size for $N = L = 40$.
The individual Su-Schrieffer-Heeger wires are in the topological phase with the parameters $t_A = 0.3$ and $t_B = 1$, since the transport properties of the edge states are of interest. The inter-wire-coupling is chosen to be weaker than the hopping strengths within a wire, in order not to alter the properties experienced in the one-dimensional chain too much, $t_N = 0.2$.
Fig. 17(a) presents the current voltage characteristic for these parameters. The overall current between two wires, resulting from the sum of all currents living on the bonds that connect these wires, is constant in the system. Furthermore it equals the current from the left lead onto the first wire and from the last wire into the right lead. This is a manifestation of Kirchhoff's point rule in two dimensions. The discussed current is called transmission current and it is plotted in fig. 17(a). The transmission current starts to flow from zero voltage, exhibits a quasi-plateau, where the slope is smaller, then rises again and finally saturates.
Fig. 17(b) serves to study the current distribution within the wires. It shows the average of all bond currents that flow between the Su-Schrieffer-Heeger wires at a certain vertical site index l including the in- and outflow, due to the leads, at this l. From fig. 17(b) it can be learned that the current at $V_B = 1$ flows nearly exclusively along the edge sites of the connected Su-Schrieffer-Heeger wires and is zero in the center of the array. This suggests that the current is carried by edge states of neighboring wires that overlap, due to the coupling t_N. At larger voltages a part of the current flows in the center.
Fig. 17(c) shows the trace (sum over all sites) of the local spectral function of the array at $V_B = 1$. Its structure is very different from the one-dimensional analogue presented in fig. 13(b). There is no hint of an energy gap to be recognized from this illustration and no distinct zero energy peak to be seen. Furthermore the trace of the spectral function is not symmetric in ω anymore. The reason for the latter is that the same set of bath sites is now coupled to a whole wire, instead of a single system site, which destroys the particle-hole symmetry.
This kind of representation of the spectral function lacks spatial resolution, but it is still possible to make a rough distinction between peaks that are localized at the edges of the Su-Schrieffer-Heeger wires and those that belong to the bulk. To this end the local spectral function is summed over again, sparing the five outmost tight binding chains at the top and bottom of the array. The

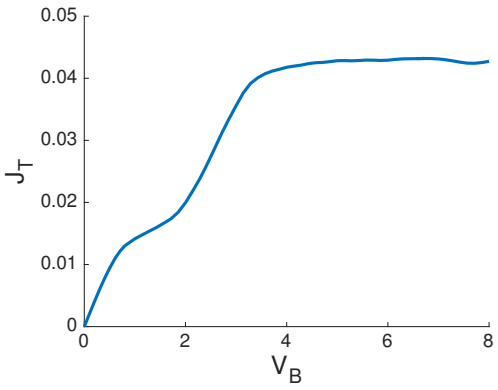

(a) Transmission current vs. bias voltage.

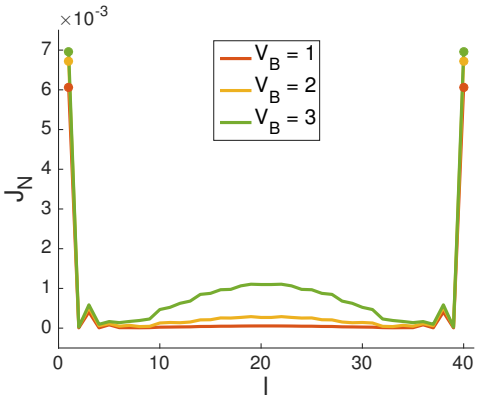

(b) Average current for a given vertical site l.

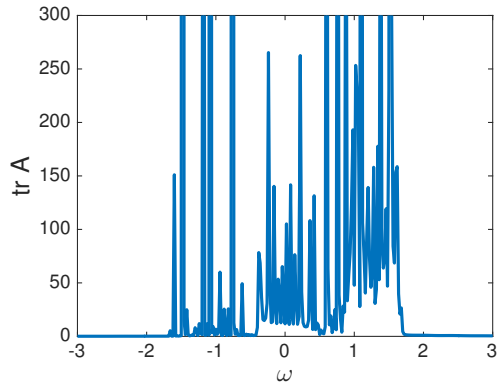

(c) Trace (sum over all sites) of the local spectral function.

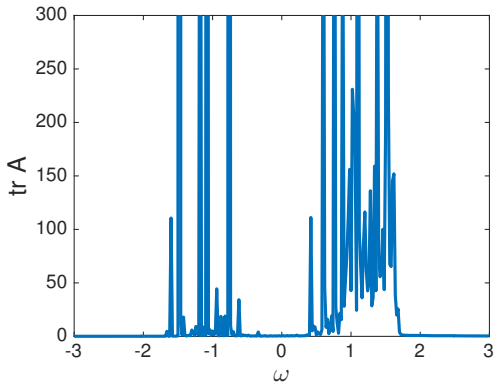

(d) Like (c) excl. edge sites $l = 1, \ldots, 5$, $l = 36, \ldots, 40$.

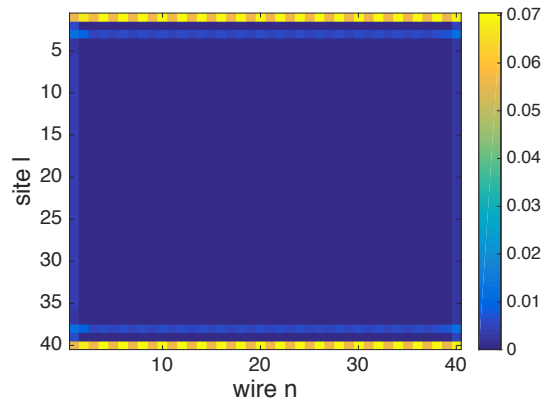

(e) Local spectral function at $\omega = 0$.

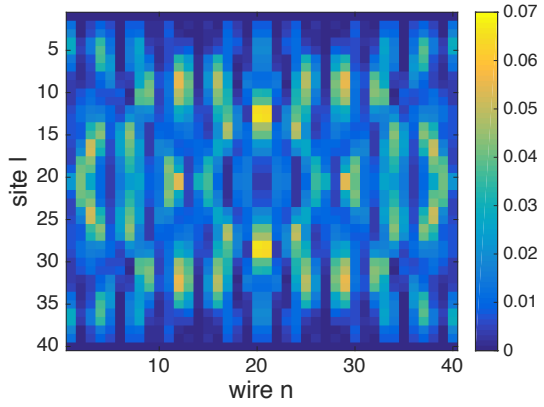

(f) Local spectral function at $\omega = 1$.

Figure 17: Simulation results for the two-dimensional array of Su-Schrieffer-Heeger wires in the topological phase, according to fig. 16 with $N = L = 40$, $t_A = 0.3$, $t_B = 1$, $t_N = 0.2$. The spectral functions (c)-(f) are plotted at $V_B = 1$. At low voltages a current is carried across the system by overlapping edge states of the individual Su-Schrieffer-Heeger wires, see fig. (b) and (e). At higher voltages also bulk states contribute to this current, see fig. (b) and (f). A gap is present in the bulk of the Su-Schrieffer-Heeger wires, as indicated by (d). Therefore the transmission current in (a) runs in the first quasi-plateau, before rising again.

result is plotted in fig. 17(d). From this plot the existence of a bulk gap is clearly evident. It shows that there are no bulk modes for $-0.62 < \omega < 0.4$. The low energy peaks that are present in fig. 17(c) but missing in 17(d) belong to states at the edges of the Su-Schrieffer-Heeger wires. These states do not lie at zero energy as before, but they have a distribution in energy.
In fig. 17(e) the local spectral function is plotted at $\omega = 0$. The figure shows edge states that overlap at the top and bottom of the array, respectively, and decay to zero into the bulk. There are no further low - energy states present, neither isolated edge states nor bulk states. By examining this kind of plots for all ω within the gap, it can be learned that these overlapping edge states survive for $|\omega| < 0.4$. Within this energy interval the local spectral function has always the same structure as in fig. 17(e).
The fact that not all edge states are peaked at $\omega = 0$ as in the one-dimensional case, but extend over the gap and further, is due to their overlap. As soon as the wave functions overlap, their energies split. In the one-dimensional case the edge states are not neighboring but $\sim L = 80$ sites apart from each other and therefore there is no overlap. The energy distribution of the overlapping edge states explains the monotonic increase of the transmission current for $V_B < 0.8$ in fig. 17(a). If these states lied exactly at $\omega = 0$, the current would rise more sharply and then end in a plateau, where it would be independent of V_B, before potentially rising again. The just described plateau corresponds to the low-voltage region with the monotonic increase of the current and does not correspond the quasi-plateau shown in fig. 17(a), which has other reasons, as highlighted in the following.
By investigating the local spectral function in a small energy interval above $\omega = 0.4$, the way it has been done for $\omega = 0$, it can be learned that the edge modes have vanished and horizontally extensive bulk modes follow immediately, see fig. 17(f). This means that the weight of the local spectral function along a horizontal path from the first to the last wire in the array stays finite. It can be that the system forms again a nonzero path along the edges, but this can also happen at some index l in the bulk of the Su-Schrieffer-Heeger wires. Therefore this kind of modes is able to carry a current from one lead across the system to the other lead. For positive ω, there is no energy gap between these modes and the edge modes. For negative ω a gap is present between $-0.75 \lesssim \omega < -0.4$. In this region the system exhibits isolated edge modes and horizontally non-extensive bulk modes. For $\omega < -0.75$ horizontally extensive bulk modes are present. The one-sided and furthermore sparse availability of appropriate states for electrons at $0.8 < V_B < 1.5$ is the reason for the weak rise of the transmission current in this interval, see fig. 17(a). The current increases more strongly for $V_B > 1.5$, because more of these states are present per energy interval. As a consequence, it is expected that a part of the current flows at some l in the center of the Su-Schrieffer-Heeger wires. From fig. 17(b) it can be learned that this is indeed the case, although a large part of the current still flows along the vertical edges. The transmission current saturates at $V_B = 3.4$ in agreement with the spectral function that is nonzero for $|\omega| < 1.7$, see fig. 17(c).
Fig. 17(f) displays the local spectral function at $V_B = 1$ and $\omega = 1$. It confirms that the structure of the spectral function changes for large $|\omega|$. For $|\omega| < 0.4$ it hosts only overlapping edge states, see fig. 17(e). Beyond this interval bulk states appear, which may overlap at the edges of the Su-Schrieffer-Heeger wires, but this is obviously not the case at $\omega = 1$.
By investigating systems with $N = L < 40$, it can be learned that the first plateau in the current voltage characteristic 17(a) becomes more definite with increasing system size. Therefore an even more definite plateau is expected for larger systems. Unfortunately it was not possible to verify this for $N = L = 80$ and $N_B = 100$ bath sites, which would be best suited for a comparison with the one-dimensional models, especially with the Kitaev model, which is treated in the following, sec. 5.5.

5.5 Kitaev Model

In this subsection the transport properties of the Kitaev Model, eq. (54), are examined in both phases and at the phase transition. The results are presented in terms of the parameters $\epsilon = -\mu$, $t \to -t$ and $\Delta \to -\Delta$. They are furthermore compared to the simulation results of the Su-Schrieffer-Heeger Model, presented in sec. 5.3.
The leads are modeled by $N_B = 100$ bath sites with a logarithmic energy spacing, representing a constant hybridization of $\Gamma = 10^{-2}$ on $[-30, 30]$. One lead is coupled to the first site of the wire, the other lead to the last site and a voltage is applied between the leads symmetrically, according to eq. (151). The same leads and the same setup have been used to contact the Su-Schrieffer-Heeger wire previously, see sec. 5.3.
Fig. 19 shows a phase diagram of the system in the steady state, containing the current voltage characteristics and the local spectral functions at $V_B = 1$. The results have been obtained for a wire of $N = 80$ sites with the parameters, $t = 0.5$, $\Delta = 1$ and $\epsilon > 0$. The phase transition is realized by changing ϵ.
For $\epsilon < 2t$ the Kitaev wire is in the topological phase. The upper panel in fig. 19 shows the results for $\epsilon = 0.2$, representing this case. Fig. 19(a) displays the current flowing from the left lead onto the first wire site in dependence of the bias voltage. The current rises sharply from zero voltage, then runs in a first plateau, before rising again and saturating ultimately, as in [27]. Fig. 19(b) presents the trace, the sum over all sites, of the local spectral function in this case. There is an isolated peak at $\omega \simeq 0$ that corresponds to the edge states, according to fig. 18. The other

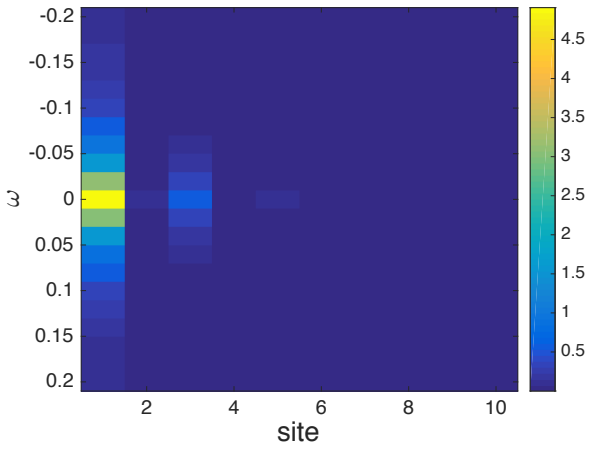

Figure 18: Local spectral function of the Kitaev wire in the topological phase, for $\epsilon = 0.2$, $t = 0.5$, $\Delta = 1$ and $V_B = 1$. The value $A_{site}(\omega)$ is represented as a color and can be obtained with the colormap. The figure shows an edge state peaked at $\omega = 0$. It is bound to a small energy region and decays rapidly into the bulk. No other states are present for $|\omega| < \frac{1}{2}\Delta_{sc}$. The image corresponds to fig. 14 for the Su-Schrieffer-Heeger wire in a different way of representation.

states extend over the bulk, which has an energy gap of $\Delta_{sc} \simeq 1.8$. The spectral function has the same structure as the one of the Su-Schrieffer-Heeger wire in the topological phase, fig. 13(b). The current voltage characteristic, in contrast, is similar to the one of the two-dimensional array of Su-Schrieffer-Heeger wires, fig. 17(a).
As previously explained, only bulk states are able to transfer electrons across the wire. In order to occupy these states, the electrons have to be supplied with energy by a voltage $V_B \geq \Delta_{sc}$. The threshold voltage $V_T = \Delta_{sc}$ is also plotted in fig. 19(a). Obviously it marks the point, where the current rises from the first plateau and not from zero as in the Su-Schrieffer-Heeger model, fig. 13(a).

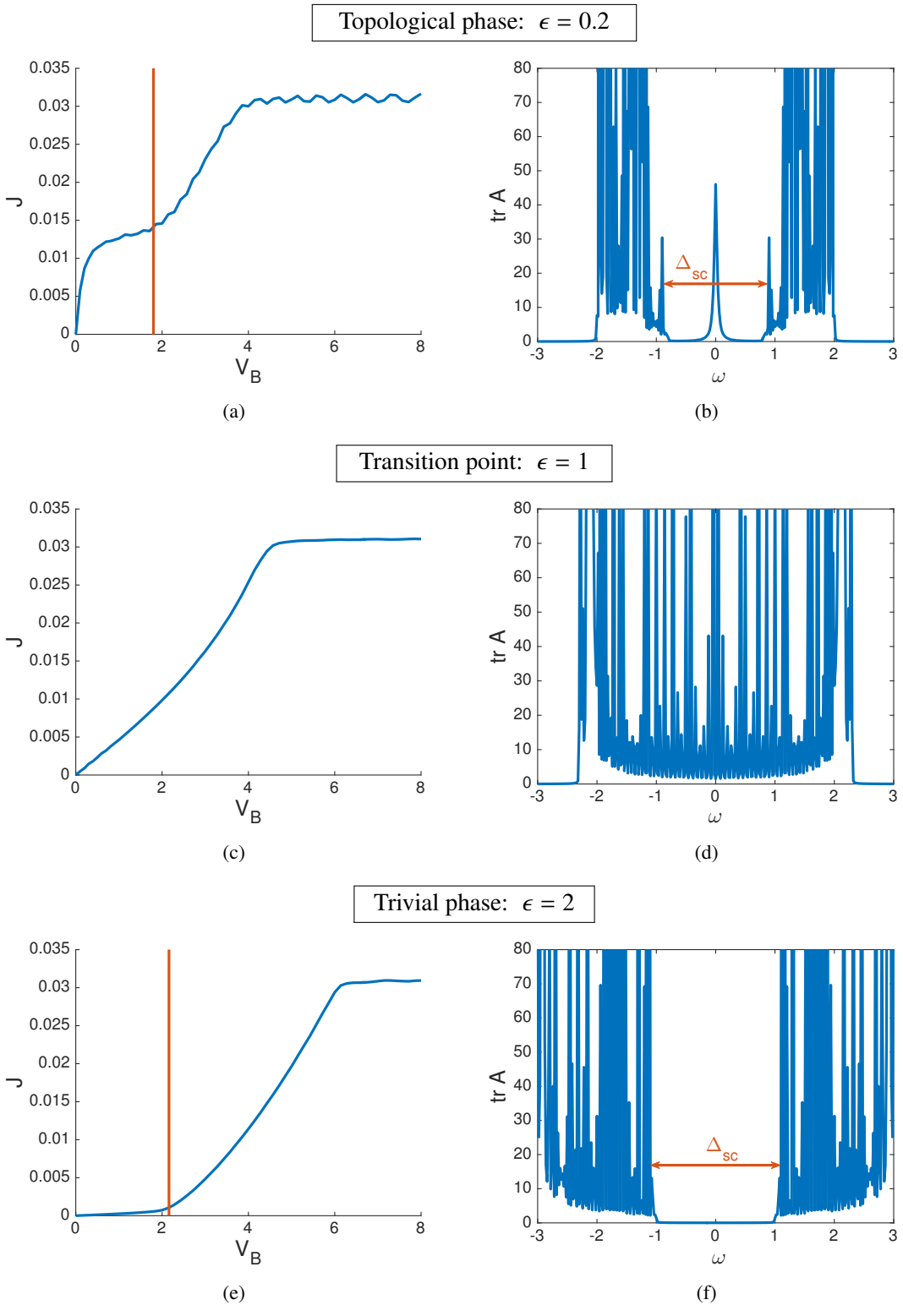

Figure 19: Phase diagram of the Kitaev Model in the steady state. The figure shows the current voltage characteristics, (a), (c), (e), and the trace (sum over all sites) of the local spectral functions at $V_B = 1$, (b), (d), (f), for different ϵ across the topological phase transition. The other parameters are $t = 0.5$ and $\Delta = 1$. The peak at $\omega = 0$ in (b) corresponds to the edge states, as demonstrated in fig. 18. The superconducting gap Δ_{sc} and the threshold voltage, at which electrons manage to overcome the gap, are marked in red.

Therefore the question arises, why a current flows onto the Kitaev wire at voltages smaller than V_T, which is not intuitive, whereas this is not possible in the Su-Schrieffer-Heeger wire, which exhibits an analogous spectral function.
This question can be answered by investigating the currents on the bonds along the wire. Fig. 20 shows the bond currents at $V_B = 1$, which is below the threshold voltage and on the first plateau in fig. 19(a). The entry for the first bond is the sum of all currents flowing from the left lead onto

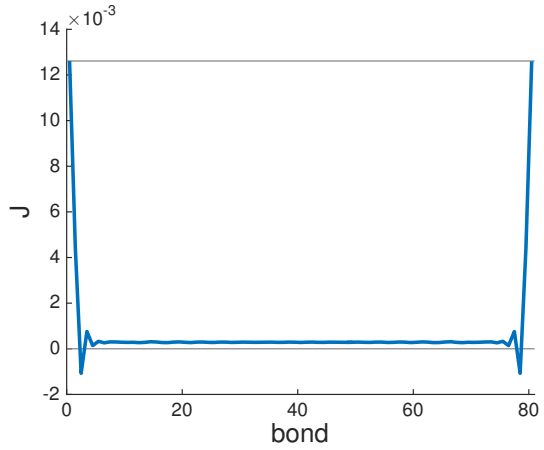

Figure 20: Bond current in the Kitaev wire in the topological phase for $\epsilon = 0.2$, $t = 0.5$, $\Delta = 1$ and $V_B = 1$. The entries for the first and last bond show the currents flowing between the leads and the wire. The entries in between show the currents between wire sites. The current in not conserved along the wire.

the first site of the wire. It is the quantity displayed in the current voltage characteristic 19(a). Obviously the bond currents arise symmetrically with respect to the center of the wire and the inflow equals the outflow, but they are not conserved along the wire. In fact, the amplitude of the current is nearly zero in the bulk. The bond current reminds of the current distribution in the two-dimensional array of Su-Schrieffer-Heeger wires, fig. 17(b).
Since the hamiltonian of the Kitaev Model (54) contains anomalous constant couplings Δ, it does not conserve the number of particles in the system, see eq. (71) or (153). Even without leads an exchange of electrons between the Kitaev wire and its environment takes place. Therefore the model does not describe an isolated wire, but a wire connected to a substrate. This is also the way the model is engineered in practice, see sec. 3.2.2.
With this knowledge the bond current in fig. 20 can be explained. Below the threshold voltage a current flows from the left lead onto the first site of the wire, where an edge state is localized. The electrons cannot move further along the wire, because within the bulk there are no states to occupy. Therefore they vanish into the substrate and reappear at the opposite edge of the wire, before flowing into the right lead. This is the reason for the small bond current at the interior of the wire. There are even bonds, where the current flows in the opposite direction.
The substrate also explains the double-plateau structure of the current voltage characteristic in fig. 19(a). Since the edge state is peaked at zero energy, the current onto the first site rises from $V_B = 0$. It runs in the first plateau, because this state is isolated in energy and no additional states are available for $V_B < V_T$. Once the threshold voltage is crossed, the electrons can occupy bulk states and therefore the current rises again. It saturates ultimately, when no more states can be made available at all, $V_S \simeq 4$.
This behavior does not arise in the Su-Schrieffer-Heeger wire, as the current is conserved in this model. In the sub-gap regime the electrons moving onto the first site cannot go further along the wire and they cannot escape into a substrate; they have to take the same way back. Therefore

there is no net current for $V_B < V_T$, see fig. 13(a). A similar behavior is exhibited by the bond currents in the interior of the Kitaev wire, because the interior sites are supplied with electrons not until V_T. Above V_T the current rises with the voltage until there are no further states.
The current voltage characteristic 19(a) has more in common with the the current voltage characteristic of the two-dimensional array of Su-Schrieffer-Heeger wires, fig. 17(a). Both exhibit a double-plateau structure instead of a single plateau, and the sub-gap current is carried by edge states. In case of the array the current is conserved. The edge states of adjacent wires overlap and are therefore able to carry the current. In case of the Kitaev Model the edge sites (and the rest of the wire) are connected to a substrate. Therefore the current flowing onto the edge sites can vanish into the substrate.
The bond currents in fig. 20 are symmetric with respect to the center of the wire, because the bias voltage is applied symmetrically, eq. (151). If the chemical potential is fixed in one of the leads, this symmetry is lost. Fig. 21 shows the currents in the Kitaev wire, when μ_R is kept constant and the voltage is applied by varying μ_L, according to eq. (152). From the plots and the

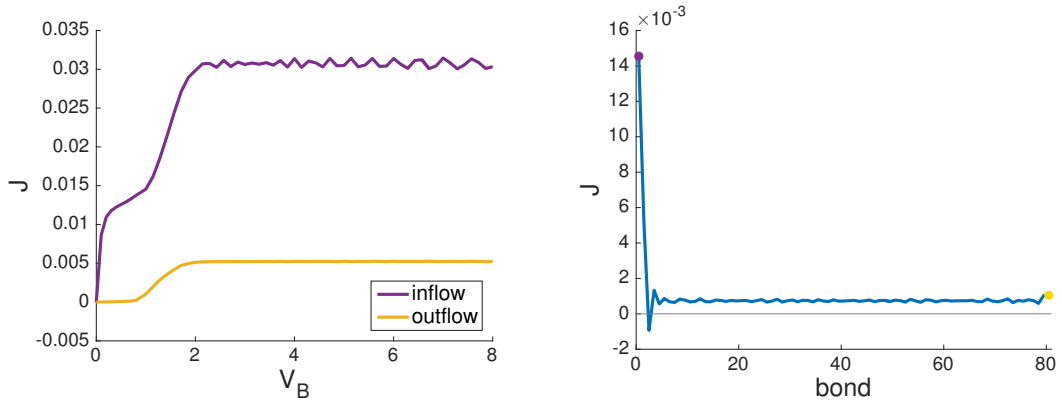

(a) Current voltage characteristics.

(b) Bond current at $V_B = 1$.

Figure 21: Currents in the Kitaev wire in the topological phase for $\epsilon = 0.2$, $t = 0.5$, $\Delta = 1$, when the chemical potential in the right lead is fixed and the voltage is applied according to eq. (152).

equation it can be learned that distinctive events occur at half the voltages as before. The gap is overcome by electrons for $V_B > 0.9 = \frac{1}{2}V_T$ and all states are used up for $V_B > 2 = \frac{1}{2}V_S$. The inflowing current exhibits a double plateau structure, as before in fig. 19(a), and the the height of the plateaus is the same. The inflow and outflow are different now. Since μ_R is kept constant, the right lead does not draw additional electrons from the substrate when the voltage is increased. The outflow starts to rise, as soon as electrons from the left lead arrive, at $\frac{1}{2}V_T$. Thus the gap is experienced by the outflowing current. Furthermore the amplitude of the current is smaller, as electrons vanish into the substrate on their way across the wire.
The oscillations that can be observed in the currents in fig. 19(a) and 21(a) are due to the bath sites. By increasing the number of bath sites or pursuing a better fit strategy, their amplitude can be reduced.
At $\epsilon = 2t$ a phase transition takes place. The superconducting gap is closed in this case and the current rises from $V_B = 0$. The simulation results are displayed in the medium panel of fig. 19. For $\epsilon > 2t$ the system is in the trivial phase. The spectrum is gapped again, but no edge states arise. The results for $\epsilon = 2$ are shown in the lower panel of fig. 19. Since no edge states are present in these cases, the results have the same structure as the corresponding results for the Su-Schrieffer-Heeger wire, fig. 13(c)-(f). Since the figures do not hold any surprises, refer to sec. 5.3 for details.

Analogue to the study of the Su-Schrieffer-Heeger wire the gap size has been determined from the spectral function for different values of ϵ at a constant t. The result is plotted in fig. 22. Obviously the gap scales linearly in $|\epsilon - 2t|$.

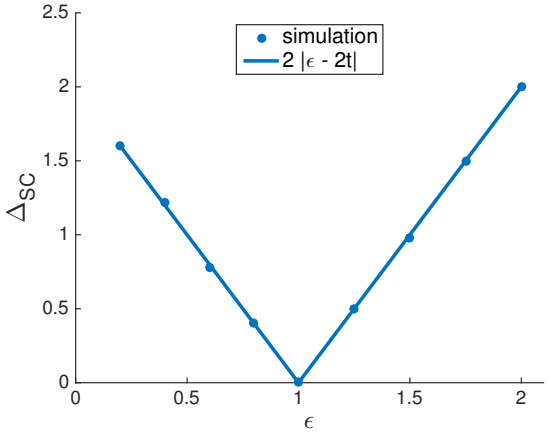

Figure 22: Closing and reopening of the gap Δ_{sc} in dependence of ϵ for $t = 0.5$ and $\Delta = 1$. Apparently the gap size is $2|\epsilon - 2t|$. The values for Δ_{sc} have been achieved from the corresponding spectral functions at $V_B = 1$.

If the same calculations are performed for a larger system, the results are qualitatively the same. In fact, this is already fulfilled for a system with $N \gtrsim 40$.

5.6 Time dependent extension of the Kitaev Model

As stated in the previous subsection, the current along the wire is not conserved in the Kitaev Model, because this model describes a wire connected to a substrate and electrons can tunnel from the wire into the substrate and vice versa. This is expressed by a hamiltonian that does not conserve the total number of particles in the wire. Writing eq. (71) and (72) explicitly for the Kitaev hamiltonian (54) yields

$$\begin{aligned} [\hat{S}\,, \hat{H}] &= 2\Delta \sum_{n=1}^{N-1} \left(c_n c_{n+1} + c_n^\dagger c_{n+1}^\dagger \right) , \\ i\frac{d}{dt} \langle \hat{S} \rangle = \langle [\hat{S}\,, \hat{H}] \rangle &\neq 0 \quad \text{for} \quad \Delta = const. \neq 0 . \end{aligned} \tag{153}$$

Thus the average number of particles changes as a function of time, if Δ is nonzero. This is supposed in the Kitaev Model, which confirms the previous statement. The idea treated in this subsection is to extend the model in a way that the average number of particles in the wire remains constant. A model that accomplishes this can be used to describe an isolated wire without substrate.

As a first extension of the Kitaev Model the pairing amplitudes are allowed to vary along the wire. Each of them is equipped with a dependence on the sites it couples, $\Delta \to \Delta_{n,n+1}$. This results in a new hamiltonian,

$$\hat{H} = -\mu \sum_{n=1}^{N} c_n^\dagger c_n - \sum_{n=1}^{N-1} \left(t c_n^\dagger c_{n+1} + \Delta_{n,n+1} c_n c_{n+1} + h.c. \right) . \tag{154}$$

The hamiltonian (154) is also inserted in eq. (72), yielding eq. (155):

$$
\begin{aligned}
[\hat{S}\,, \hat{H}] &= 2\sum_{n=1}^{N-1}\left(\Delta_{n,n+1}c_n c_{n+1} + \Delta^*_{n,n+1}c_n^\dagger c_{n+1}^\dagger\right) \\
i\frac{d}{dt}\langle\hat{S}\rangle = \langle[\hat{S}\,, \hat{H}]\rangle = 0 \quad &\text{for} \quad \Delta_{n,n+1} = \; V\langle c_n^\dagger c_{n+1}^\dagger\rangle \\
&\text{implying} \quad \Delta^*_{n,n+1} = -V\langle c_n c_{n+1}\rangle
\end{aligned}
\tag{155}
$$

Thus the average number of particles is conserved, if the pairing amplitudes are chosen proportional to the expectation values $\Delta_{n,n+1} \propto \langle c_n^\dagger c_{n+1}^\dagger\rangle$. Through this relation they depend on the density operator of the system and therefore, in general, also on time. This is a particular case of a general theorem by Baym and Kadanoff, according to which an approximation must be self-consistent, in order to be conserving, see [28]. The hamiltonian (154) with the amplitudes (155) can be used to describe an isolated wire.

These equations also show, where the origin of the Kitaev Model is rooted. It can be derived from an interacting hamiltonian with interaction V by applying a mean field approximation. Due to the coupling of the wire to a substrate, particle exchanges take place that allow to fix $\Delta_{n,n+1}(t) = \Delta$ to a constant value. The particular value of Δ depends on the choice of the substrate. By varying the substrate's parameters it can, in principle, be tuned to any desired value.

In order to describe a wire without substrate, the pairing amplitudes have to be determined according to eq. (155) and cannot be kept fixed. Inserting the hamiltonian with these amplitudes, (154) and (155), into the Lindblad equation yields a differential equation which is nonlinear. As a consequence the time evolution of expectation values cannot be obtained by diagonalizing the Liouvillian, eq. (96), and using eq. (128), which is not valid in this case. Neither valid is eq. (138) to determine a steady state without explicitly calculating the time evolution. In order to determine the dynamics of the system and eventually a steady state, the set of equations (129) has to be integrated. $\Delta_{n,n+1}$ are contained in the matrix $\mathcal{A}$, see eq. (130) and (69), and they depend on the solution $\boldsymbol{\eta}$, see eq. (119) and (155), which makes the equations (129) also nonlinear. They have to be solved selfconsistently, e.g. with an appropriate Runge-Kutta scheme.

Fig. 23 shows the solution for a system of $N = 5$ sites with $V = -1$, $t = -0.5$ and $\mu = -0.2$. These parameters drive an ordinary Kitaev wire in the topological phase. The leads have been modeled using $N_B = 10$ bath sites with a logarithmic energy spacing representing a constant

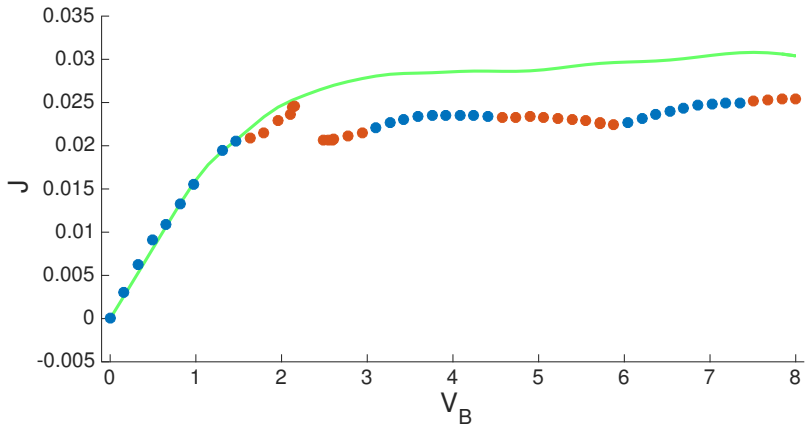

Figure 23: Average current vs. voltage after transient for $N = 5$, $V = -1$, $t = -0.5$ and $\mu = -0.2$. Collection of solutions to different initial conditions, classified, according to their type, in different colors. The average current along the wire is now conserved.

hybridization $\Gamma = 10^{-2}$ on $[-10, 10]$.
It turns out that after a transient a quasi-stationary state is reached, where the observables are either constant or periodic in time. The solutions can be divided into three types, marked by different colors corresponding to the colors in fig. 23:

- Type I: $\Delta_{n,n+1}(t) = 0, \quad J = const.$
  This is the trivial case. $\Delta_{n,n+1} = 0$ is always a solution, since it reduces the model to the ordinary tight binding model without superconductivity. The current is constant and identical for all bonds in this case, obeying Kirchhoff's point rule. Its value matches the steady state current determined from eq. (138).

- Type II: $\Delta_{n,n+1}(t)$ oscillate with one single frequency, $\quad J = const.$
  All $\Delta_{n,n+1}$ oscillate with the same frequency, but different amplitudes, according to $\Delta_{n,n+1}(t) = |\Delta_{n,n+1}| e^{ivt}$. They are zero on average and their absolute value is constant in time. They yield a current which is also constant in time and identical for all bonds. Thus Kirchhoff's point rule is also fulfilled in this case. This type of solution is displayed in fig. 24.

- Type III: $\Delta_{n,n+1}(t)$ oscillate with multiple frequencies, $\quad J$ oscillates
  The $\Delta_{n,n+1}$ oscillate with multiple frequencies, different amplitudes and are zero on average. The bond currents also oscillate with one ore more frequencies and different amplitudes. Their average value is the same for all bonds. Due to the time dependence of charge, Kirchhoff's point rule does not apply at a particular time, but it applies on average. However, at any time the continuity equation is valid, as it should be. Fig. 25 shows an example for this type of solution.

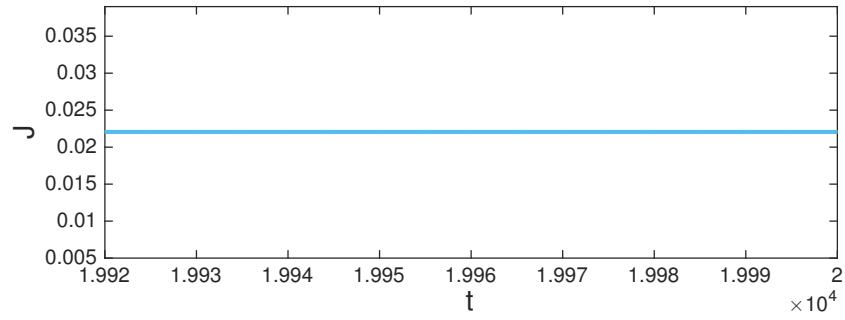

(a) Bond current.

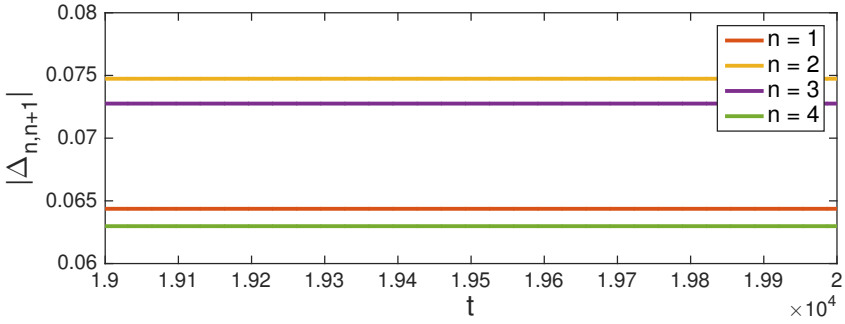

(b) Pairing amplitudes.

Figure 24: Type II solution at $V_B = 3.1$. The parameters are the same as in fig. 23. Fig. 24(a) shows the bond current in dependence of time after the transient and (b) the absolute values of the corresponding pairing amplitudes. Since they are oscillating with a single frequency, the absolute values are constant in time.

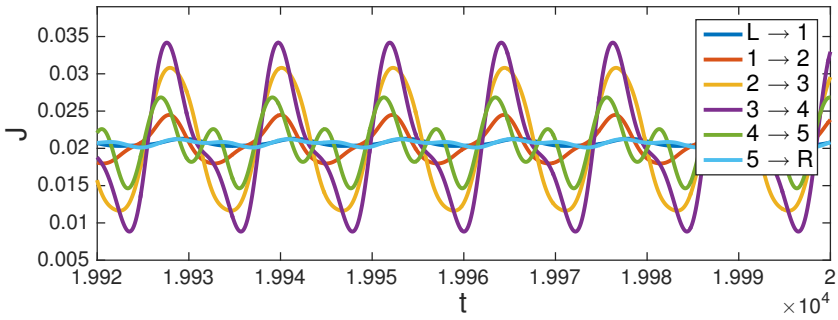

(a) Bond currents.

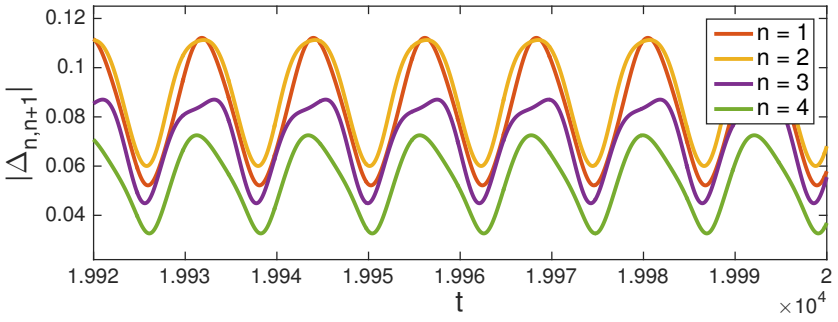

(b) Pairing amplitudes.

Figure 25: Type III solution at $V_B = 2.6$. The parameters are the same as in fig. 23. Fig. 25(a) shows the bond currents in dependence of time after the transient and (b) the absolute values of the corresponding pairing amplitudes. Both are oscillating with multiple frequencies. L and R denote the left and right lead and $n = 1 \ldots 5$ the wire sites. Integrating the current over a number of periods yields the same result for all bonds. Thus the charge and the number of particles are conserved on average, as required. The bond currents fulfill the continuity equation, as it should be.

An analogous appearance of three types of solutions has also been obsered in the superconducting system studied in [29].
In fig. 23 the average current after the transient is plotted for different bias voltages. The results have been obtained from different initial conditions. The solutions of type II and III seem to be assigned to certain voltage regions. I did not manage to get a solution of type II for a voltage, where a type III solution has been found previously, and vice versa. Generally, all nontrivial results in the quasi-stationary state have been identical, except for one case, where I managed to get two type III solutions at the same voltage. For $2.2 < V_B < 2.4$ and $V_B = 1.1$ it was not possible to get nontrivial solutions at all. The type III solutions at $V_B < 2.2$ do not seem to have overcome the transient, they are not stable.
Due to the necessity of a selfconsistent solution and the time dependence, the studied system is chosen much smaller than the systems treated before. The simulation time until the quasi-stationary state is reached increases with increasing system size, compare sec. 5.1. Therefore the time dependence is a problem. This problem did not arise in case of a linear Liouvillian, because the steady state could be calculated directly, using eq. (138).
A further investigation of this model is necessary, in order to clarify its behavior definitely. Furthermore a larger system should be investigated to limit finite size effects. This has not been done in the framework of this thesis.

6 Conclusions and outlook

Conclusions: There has been recently a widespread interest in topological states of matter and in Majorana fermions. The Su-Schrieffer-Heeger Model, eq. (41), and the Kitaev Model, eq. (54), are the simplest models, where a topological phase is realized. In this phase zero-energy edge states arise. In the case of the Kitaev Model, these states are described by Majorana fermions. Within this thesis I was primarily interested in the Kitaev Model and used the Su-Schrieffer-Heeger Model as a reference. The latter does not contain any anomalous BCS couplings and is therefore easier to understand.
The results for the Kitaev wire in the trivial, i.e. non-topological, phase and at the critical point are as expected. The current-voltage curves are consistent with the spectral functions, see fig. 19(c)-(f), and the results have the same structure as the ones for the Su-Schrieffer-Heeger wire, fig. 13(c)-(f). The current starts to flow from a threshold voltage corresponding to the size of the bulk gap, which is finite in the trivial phase and zero at the critical point.
In the topological phase, in contrast, the current flowing onto the Kitaev wire, fig. 19(a), at first glance does not seem to match with the spectral function, fig. 19(b). Despite the presence of a bulk gap, see fig. 19(b) and 18, it rises from zero voltage. It appears, as if the edge states would carry a current along the wire, which is not plausible, because these states are highly localized at the boundaries. This behavior is not exhibited by the Su-Schrieffer-Heeger wire, whose results are consistent, see fig. 13(a), (b) and 14.
The key to this peculiar behavior is that the Kitaev hamiltonian does not conserve the total number of particles in the wire, see eq. (153). Therefore, in contrast to the Su-Schrieffer-Heeger hamiltonian, it does not describe an isolated wire, but a wire connected to a substrate, and electrons can tunnel between the two systems. As a consequence, the current along the wire leaks, when it is driven out of equilibrium. With this knowledge the simulation results in the topological phase can be arranged in a consistent picture: The sub-gap current in fig. 19(a) is indeed carried by edge states, but it does not flow *along* the wire, as previously assumed, but tunnels into the substrate at one edge and reappears in the wire at the other edge, see fig. 20, in accordance with the bulk gap, see fig. 18.
The property of the Kitaev hamiltonian, not to conserve the particle number in the wire, is generic to BCS-like hamiltonians and is related to the presence of anomalous pairing amplitudes, see eq. (153). Pairing BCS terms, which generically break particle conservation, originate from a mean-field approximation of an interacting model. While this original model conserves particle number, it is the approximation that breaks this conservation. However, it has been shown in a pioneering work by L.P. Kadanoff and G. Baym [28] that conserving approximations can be achieved, provided they are self-consistent. Also the Kitaev hamiltonian can be self-consistently derived from an interacting hamiltonian, namely by a mean-field approximation, but only if a substrate is taken into account. This substrate allows to fix the resulting pairing amplitudes to a time-independent value. As a consequence the particle number in the overall system *wire + substrate* is conserved, but not the particle number in the wire alone. In order to describe an isolated wire with a Kitaev-like hamiltonian, the pairing amplitudes resulting from the mean-field approximation cannot be assumed time-independent anymore. In general, the self-consistent calculation will produce time-dependent pairing terms in the nonequilibrium case. This time dependence is crucial, if one wants to have superconductivity *and* conservation laws in the derived model.
Such a time-dependent extension of the Kitaev Model is investigated in this thesis in sec. 5.6. After the transient a quasi-stationary state is reached, where all observables are either constant or periodic in time. In the quasi-steady state three types of solutions can be distinguished. They all have in common that the total number of particles in the wire is conserved and that the bond

currents obey the continuity equation, as it should be. The results for the time-dependent model cannot be compared directly to the presented results for the Kitaev Model, because the system is too small. The main issue in the calculation is the time dependence associated with the self-consistent solution. If it were possible to determine the quasi-stationary state directly, larger systems could be studied. Since no strategy has been found to do this yet, the self-consistence problem has to be solved at each time step. The time until a quasi-steady state is reached increases with increasing system size.
In order to study the transport properties of edge states also with the Su-Schrieffer-Heeger Model, a two-dimensional array of weakly coupled wires has been constructed, see fig. 16. The voltage has been applied perpendicular to the wire axis, in a direction, where the edge states of adjacent wires overlap, see fig. 17(e). Due to their spatial extension, these states contribute to the current across the system, see fig. 17(a) and (b). In the topological phase this current, fig. 17(a), has the same structure as the current flowing onto the Kitaev wire, fig. 19(a), confirming the result that the sub-gap current in the latter is carried by edge states.

Outlook: For further calculations a better fitting scheme should be developed, such that the number of bath sites in the leads can be reduced without compromising accuracy. This would allow to calculate larger systems. A procedure to do this has been introduced in [30, 10].
For the time dependent extension of the Kitaev Model a more efficient calculation scheme is desirable. In order to compare the results to the ordinary Kitaev Model, the number of sites has to be increased significantly. Furthermore the spectral function in the quasi-steady state has to be calculated and it should be investigated, whether edge states arise in this model. It has to be clarified, which types of solutions and how many of them can arise in dependence of the bias voltage.
In addition to the presented systems, a two-dimensional array of Kitaev wires should be studied, analog to the one in fig. 16. A step in this direction has already been made and current voltage characteristics have been obtained. Below a certain threshold voltage the current flowing into the system rises weakly with a nearly constant slope and it does not exhibit a double-plateau structure as fig. 17(a). Due to numerical problems with the spectral function, the reason for this behavior has not yet been identified.
In the future also the effect of electron-electron interactions shall be investigated, as it is currently done for other systems in our working group, see e.g. [10, 31].

7 Appendix

7.1 Symmetry relations

A generalized noninteracting system, which is a system including superconducting anomalous couplings, exhibits for all indices $k, j \in [1, N]$ the following symmetry relations:

$$\begin{aligned} \boldsymbol{\beta} &= i \begin{pmatrix} \boldsymbol{\Omega} & 2\boldsymbol{\Upsilon}^{(+)} \\ 2\boldsymbol{\Upsilon}^{(-)} & -\boldsymbol{\Omega}^{\intercal} \end{pmatrix} \\ -\boldsymbol{\beta}^{\intercal} &= i \begin{pmatrix} -\boldsymbol{\Omega}^{\intercal} & 2\boldsymbol{\Upsilon}^{(-)} \\ 2\boldsymbol{\Upsilon}^{(+)} & \boldsymbol{\Omega} \end{pmatrix} \end{aligned} \quad \Rightarrow \quad \begin{aligned} \beta_{k,j} &= -\beta_{j+N,k+N} \\ \beta_{k,j+N} &= -\beta_{j,k+N} \\ \beta_{k+N,j} &= -\beta_{j+N,k} \\ \beta_{k+N,j+N} &= -\beta_{j,k} \end{aligned} \tag{156}$$

$$\begin{aligned} \boldsymbol{\alpha}^{\dagger} &= \begin{pmatrix} \frac{1}{2}(\boldsymbol{h} + i\boldsymbol{\Lambda}) & \boldsymbol{a}^{\dagger} \\ \boldsymbol{a} & -\frac{1}{2}(\boldsymbol{h} - i\boldsymbol{\Lambda})^{\intercal} \end{pmatrix} \\ -\boldsymbol{\alpha}^{\intercal} &= \begin{pmatrix} -\frac{1}{2}(\boldsymbol{h} - i\boldsymbol{\Lambda})^{\intercal} & \boldsymbol{a} \\ \boldsymbol{a}^{\dagger} & \frac{1}{2}(\boldsymbol{h} + i\boldsymbol{\Lambda}) \end{pmatrix} \end{aligned} \quad \Rightarrow \quad \begin{aligned} (\boldsymbol{\alpha}^{\dagger})_{k,j} &= -\alpha_{j+N,k+N} \\ (\boldsymbol{\alpha}^{\dagger})_{k,j+N} &= -\alpha_{j,k+N} \\ (\boldsymbol{\alpha}^{\dagger})_{k+N,j} &= -\alpha_{j+N,k} \\ (\boldsymbol{\alpha}^{\dagger})_{k+N,j+N} &= -\alpha_{j,k} \end{aligned}$$

This follows from a comparison of (96) with the general structure (102). The skew symmetry of $\boldsymbol{a}$, $\boldsymbol{\Upsilon}^{(+)}$ and $\boldsymbol{\Upsilon}^{(-)}$ and the hermiticity of $\boldsymbol{h}$ and $\boldsymbol{\Lambda}$ have been used to obtain this result.

7.2 K - relations

In order to determine the time evolution and the steady state of a system through diagonalization, the commutators of the Liouvillian with the quasiparticle creation and annihilation operators, $\bar{f}_n$ and f_m, have to be calculated. For a generalized noninteracting system the following sums arise thereby,

$$\begin{aligned} \overline{S} &:= \sum_{i=1}^{4N} \overline{K}_{ni} \lambda_i f_i \,, \\ S &:= \sum_{i=1}^{4N} K_{mi} \lambda_i \bar{f}_i \,. \end{aligned}$$

$\overline{K}_{ni}$ and K_{mi} denote the anticommutators defined in eq. (117). The evaluation of these sums yields a very useful set of equations, which I called K - relations,

$$\begin{aligned} \sum_{i=1}^{4N} \overline{K}_{ni} \lambda_i f_i &= -\lambda_n \bar{f}_n \\ \sum_{i=1}^{4N} K_{mi} \lambda_i \bar{f}_i &= -\lambda_m f_m \end{aligned} \quad \text{or} \quad \begin{aligned} \overline{\boldsymbol{K}} \boldsymbol{D} \boldsymbol{f} &= -\boldsymbol{D} \bar{\boldsymbol{f}} \,, \\ \boldsymbol{K} \boldsymbol{D} \bar{\boldsymbol{f}} &= -\boldsymbol{D} \boldsymbol{f} \,. \end{aligned} \tag{157}$$

As a little side note, they show immediately that $\overline{\boldsymbol{K}} = \boldsymbol{K}^{-1}$. Furthermore $\overline{\boldsymbol{K}} \neq \boldsymbol{K}^{\dagger}$, since $\boldsymbol{f}$ and $\bar{\boldsymbol{f}}$ are not linked to each other by hermitian conjugation, which results of the Liouvillian not being hermitian.

The validity of the K - relations is demonstrated in the following. It is a long calculation using the eigenvalue equations (106), (107) and (110) and the symmetry relations (156) of the Liouvillian. Due to the block structure of $\boldsymbol{K}$ and $\overline{\boldsymbol{K}}$ the cases $i/n/m \in [1, 2N]$ and $i/n/m \in [2N+1, 4N]$ are treated separately.

Calculation for $\overline{K}$

First of all, the sum $\overline{S}$ is split into two contributions with respect to the summation index i,

$$\overline{S} = \overbrace{\sum_{i=1}^{2N} \overline{K}_{ni} \lambda_i f_i}^{=: \overline{S}_1} + \overbrace{\sum_{i=2N+1}^{4N} \overline{K}_{ni} \lambda_i f_i}^{=: \overline{S}_2} . \tag{158}$$

A further distinction of cases is made concerning the second index n. Then the definitions of $\overline{\boldsymbol{K}}$ and $\boldsymbol{f}$, eq. (117) and (115), can be filled in to evaluate $\overline{S}_1$ and $\overline{S}_2$.

1.) $n \in [1, 2N]$

Since $\overline{\boldsymbol{K}} = \boldsymbol{0}$ in the upper left sector, the first summand vanishes,

$$\overline{S}_1 = 0 . \tag{159}$$

The second summand is determined by

$$\begin{aligned} \overline{S}_2 = \sum_{j,k=1}^{N} \sum_{i=2N+1}^{4N} \Big\{ & \left(\boldsymbol{u}^{-1\dagger}\right)_{k+N,\, i-2N} \lambda_i \left(\boldsymbol{u}^{\dagger}\right)_{i-2N,\, j+N} u_{k,n} A_j^{\dagger} \\ & + \left(\boldsymbol{u}^{-1\dagger}\right)_{k,\, i-2N} \lambda_i \left(\boldsymbol{u}^{\dagger}\right)_{i-2N,\, j+N} u_{k+N,\, n} A_j^{\dagger} \\ & + \left(\boldsymbol{u}^{-1\dagger}\right)_{k+N,\, i-2N} \lambda_i \left(\boldsymbol{u}^{\dagger}\right)_{i-2N,\, j} u_{k,n} B_j^{\dagger} \\ & + \left(\boldsymbol{u}^{-1\dagger}\right)_{k,\, i-2N} \lambda_i \left(\boldsymbol{u}^{\dagger}\right)_{i-2N,\, j} u_{k+N,\, n} B_j^{\dagger} \Big\} . \end{aligned}$$

Executing the sum over i and thereby using the eigenvalue equation (107) yields

$$\begin{aligned} \overline{S}_2 = \sum_{j,k=1}^{N} \Big\{ & \left[\left(\boldsymbol{\alpha}^{\dagger}\right)_{k+N,\, j+N} u_{k,n} + \left(\boldsymbol{\alpha}^{\dagger}\right)_{k,\, j+N} u_{k+N,\, n} \right] A_j^{\dagger} \\ & + \left[\left(\boldsymbol{\alpha}^{\dagger}\right)_{k+N,\, j} u_{k,n} + \left(\boldsymbol{\alpha}^{\dagger}\right)_{k,\, j} u_{k+N,\, n} \right] B_j^{\dagger} \Big\} . \end{aligned}$$

Now the symmetries of $\boldsymbol{\alpha}$ are used to express sectors of $\boldsymbol{\alpha}^{\dagger}$ through sectors of $-\boldsymbol{\alpha}^{\intercal}$, eq. (156),

$$\overline{S}_2 = -\sum_{j=1}^{N} \sum_{k=1}^{2N} \left[\alpha_{j,k} u_{k,n} A_j^{\dagger} + \alpha_{j+N,\, k} u_{k,n} B_j^{\dagger} \right] ,$$

where the sum over k now runs up to $2N$. Filling in the other eigenvalue equation (106) yields

$$\begin{aligned}\overline{S}_2 &= -\lambda_n \sum_{j=1}^{N} \left[u_{j,n} A_j^\dagger + u_{j+N,n} B_j^\dagger \right] \\ &= -\lambda_n \bar{f}_n \, .\end{aligned} \tag{160}$$

The result for the case $n \in [1, 2N]$ is obtained by combining eq. (159) and (160) to (158) and it is identical to eq. (157),

$$\begin{aligned}\overline{S} &= \overline{S}_1 + \overline{S}_2 \\ &= -\lambda_n \bar{f}_n \, .\end{aligned}$$

2.) $n \in [2N+1, 4N]$

In this case the first summand yields

$$\begin{aligned}\overline{S}_1 = \sum_{j,k=1}^{N} \sum_{i=1}^{2N} \Big\{ & u_{k+N,i}\, \lambda_i \left(\boldsymbol{u}^{-1}\right)_{i,j} \left(\boldsymbol{u}^{-1\dagger}\right)_{k,n-2N} A_j \\ & + u_{k,i}\, \lambda_i \left(\boldsymbol{u}^{-1}\right)_{i,j} \left(\boldsymbol{u}^{-1\dagger}\right)_{k+N,n-2N} A_j \\ & + u_{k+N,i}\, \lambda_i \left(\boldsymbol{u}^{-1}\right)_{i,\,j+N} \left(\boldsymbol{u}^{-1\dagger}\right)_{k,n-2N} B_j \\ & + u_{k,i}\, \lambda_i \left(\boldsymbol{u}^{-1}\right)_{i,\,j+N} \left(\boldsymbol{u}^{-1\dagger}\right)_{k+N,n-2N} B_j \\ & - u_{k+N,i}\, \lambda_i \left(\boldsymbol{u}^{-1}\boldsymbol{u}^{(c)}\boldsymbol{u}^{\dagger}\right)_{i,\,j+N} \left(\boldsymbol{u}^{-1\dagger}\right)_{k,n-2N} A_j^\dagger \\ & - u_{k,i}\, \lambda_i \left(\boldsymbol{u}^{-1}\boldsymbol{u}^{(c)}\boldsymbol{u}^{\dagger}\right)_{i,\,j+N} \left(\boldsymbol{u}^{-1\dagger}\right)_{k+N,n-2N} A_j^\dagger \\ & - u_{k+N,i}\, \lambda_i \left(\boldsymbol{u}^{-1}\boldsymbol{u}^{(c)}\boldsymbol{u}^{\dagger}\right)_{i,j} \left(\boldsymbol{u}^{-1\dagger}\right)_{k,n-2N} B_j^\dagger \\ & - u_{k,i}\, \lambda_i \left(\boldsymbol{u}^{-1}\boldsymbol{u}^{(c)}\boldsymbol{u}^{\dagger}\right)_{i,j} \left(\boldsymbol{u}^{-1\dagger}\right)_{k+N,n-2N} B_j^\dagger \Big\} \, .\end{aligned}$$

The sum over i can again be executed with the help of eq. (106),

$$\begin{aligned}\overline{S}_1 = \sum_{j,k=1}^{N} \Big\{ & \left[\alpha_{k+N,\,j} \left(\boldsymbol{u}^{-1\dagger}\right)_{k,n-2N} + \alpha_{k,j} \left(\boldsymbol{u}^{-1\dagger}\right)_{k+N,n-2N} \right] A_j \\ & + \left[\alpha_{k+N,\,j+N} \left(\boldsymbol{u}^{-1\dagger}\right)_{k,n-2N} + \alpha_{k,\,j+N} \left(\boldsymbol{u}^{-1\dagger}\right)_{k+N,n-2N} \right] B_j \Big\} =: \overline{S}_{11} \\ & - \Big[\left(\boldsymbol{\alpha}\boldsymbol{u}^{(c)}\boldsymbol{u}^{\dagger}\right)_{k+N,\,j+N} \left(\boldsymbol{u}^{-1\dagger}\right)_{k,n-2N} + \left(\boldsymbol{\alpha}\boldsymbol{u}^{(c)}\boldsymbol{u}^{\dagger}\right)_{k,\,j+N} \left(\boldsymbol{u}^{-1\dagger}\right)_{k+N,n-2N} \Big] A_j^\dagger \\ & - \Big[\left(\boldsymbol{\alpha}\boldsymbol{u}^{(c)}\boldsymbol{u}^{\dagger}\right)_{k+N,\,j} \left(\boldsymbol{u}^{-1\dagger}\right)_{k,n-2N} + \left(\boldsymbol{\alpha}\boldsymbol{u}^{(c)}\boldsymbol{u}^{\dagger}\right)_{k,j} \left(\boldsymbol{u}^{-1\dagger}\right)_{k+N,n-2N} \Big] B_j^\dagger \Big\} =: \overline{S}_{12}\end{aligned} \tag{161}$$

Applying the symmetry relations of $\boldsymbol{\alpha}$, eq. (156), to the first part results in

$$\overline{S}_{11} = -\sum_{j=1}^{N} \sum_{k=1}^{2N} \left[\left(\boldsymbol{\alpha}^\dagger\right)_{j+N,\,k} \left(\boldsymbol{u}^{-1\dagger}\right)_{k,n-2N} A_j + \left(\boldsymbol{\alpha}^\dagger\right)_{j,\,k} \left(\boldsymbol{u}^{-1\dagger}\right)_{k,n-2N} B_j \right] .$$

Then the other eigenvalue equation, eq. (107), is plugged in, yielding

$$\overline{S}_{11} = -\lambda_n \sum_{j=1}^{N} \left[\left(\boldsymbol{u}^{-1\dagger}\right)_{j+N,\,n-2N} A_j + \left(\boldsymbol{u}^{-1\dagger}\right)_{j,\,n-2N} B_j \right]. \tag{162}$$

The summand $\overline{S}_2$ is also made up of two parts,

$$\begin{aligned}
\overline{S}_2 = \sum_{j,k=1}^{N} \sum_{i=2N+1}^{4N} \Bigg\{ & \left. \begin{aligned} & u^{(c)}_{k+N,\,i-2N}\, \lambda_i \left(\boldsymbol{u}^{\dagger}\right)_{i-2N,\,j+N} \left(\boldsymbol{u}^{-1\dagger}\right)_{k,\,n-2N} A^{\dagger}_j \\ & + u^{(c)}_{k,\,i-2N}\, \lambda_i \left(\boldsymbol{u}^{\dagger}\right)_{i-2N,\,j+N} \left(\boldsymbol{u}^{-1\dagger}\right)_{k+N,\,n-2N} A^{\dagger}_j \\ & + u^{(c)}_{k+N,\,i-2N}\, \lambda_i \left(\boldsymbol{u}^{\dagger}\right)_{i-2N,\,j} \left(\boldsymbol{u}^{-1\dagger}\right)_{k,\,n-2N} B^{\dagger}_j \\ & + u^{(c)}_{k,\,i-2N}\, \lambda_i \left(\boldsymbol{u}^{\dagger}\right)_{i-2N,\,j} \left(\boldsymbol{u}^{-1\dagger}\right)_{k+N,\,n-2N} B^{\dagger}_j \end{aligned} \right\} =: \overline{S}_{21} \\
& \left. \begin{aligned} & + \left(\boldsymbol{u}^{-1\dagger}\right)_{k+N,\,i-2N} \lambda_i \left(\boldsymbol{u}^{\dagger}\right)_{i-2N,\,j+N} u^{(c)}_{k,\,n-2N} A^{\dagger}_j \\ & + \left(\boldsymbol{u}^{-1\dagger}\right)_{k,\,i-2N} \lambda_i \left(\boldsymbol{u}^{\dagger}\right)_{i-2N,\,j+N} u^{(c)}_{k+N,\,n-2N} A^{\dagger}_j \\ & + \left(\boldsymbol{u}^{-1\dagger}\right)_{k+N,\,i-2N} \lambda_i \left(\boldsymbol{u}^{\dagger}\right)_{i-2N,\,j} u^{(c)}_{k,\,n-2N} B^{\dagger}_j \\ & + \left(\boldsymbol{u}^{-1\dagger}\right)_{k,\,i-2N} \lambda_i \left(\boldsymbol{u}^{\dagger}\right)_{i-2N,\,j} u^{(c)}_{k+N,\,n-2N} B^{\dagger}_j \Bigg\} \end{aligned} \right\} =: \overline{S}_{22}
\end{aligned} \tag{163}$$

Eq. (107) is applied to the second part,

$$\begin{aligned}
\overline{S}_{22} = \sum_{j,k=1}^{N} \Bigg\{ & \left[\left(\boldsymbol{\alpha}^{\dagger}\right)_{k+N,\,j+N} u^{(c)}_{k,\,n-2N} + \left(\boldsymbol{\alpha}^{\dagger}\right)_{k,\,j+N} u^{(c)}_{k+N,\,n-2N} \right] A^{\dagger}_j \\
& + \left[\left(\boldsymbol{\alpha}^{\dagger}\right)_{k+N,\,j} u^{(c)}_{k,\,n-2N} + \left(\boldsymbol{\alpha}^{\dagger}\right)_{k,\,j} u^{(c)}_{k+N,\,n-2N} \right] B^{\dagger}_j \Bigg\},
\end{aligned}$$

and then the symmetry relations (156),

$$\begin{aligned}
\overline{S}_{22} &= -\sum_{j=1}^{N} \sum_{k=1}^{2N} \left[\alpha_{j,k}\, u^{(c)}_{k,\,n-2N} A^{\dagger}_j + \alpha_{j+N,\,k}\, u^{(c)}_{k,\,n-2N} B^{\dagger}_j \right] \\
&= -\sum_{j=1}^{N} \left[\left(\boldsymbol{\alpha}\boldsymbol{u}^{(c)}\right)_{j,\,n-2N} A^{\dagger}_j + \left(\boldsymbol{\alpha}\boldsymbol{u}^{(c)}\right)_{j+N,\,n-2N} B^{\dagger}_j \right].
\end{aligned} \tag{164}$$

Combining the so far unconsidered parts in eq. (161) and (163) yields

$$\begin{aligned}
\overline{S}_{12} + \overline{S}_{21} = \sum_{j,k=1}^{N} \Bigg\{ & \left(\boldsymbol{u}^{(c)}\boldsymbol{D}^{\dagger}\boldsymbol{u}^{\dagger} - \boldsymbol{\alpha}\boldsymbol{u}^{(c)}\boldsymbol{u}^{\dagger}\right)_{k+N,\,j+N} \left(\boldsymbol{u}^{-1\dagger}\right)_{k,\,n-2N} A^{\dagger}_j \\
& + \left(\boldsymbol{u}^{(c)}\boldsymbol{D}^{\dagger}\boldsymbol{u}^{\dagger} - \boldsymbol{\alpha}\boldsymbol{u}^{(c)}\boldsymbol{u}^{\dagger}\right)_{k,\,j+N} \left(\boldsymbol{u}^{-1\dagger}\right)_{k+N,\,n-2N} A^{\dagger}_j \\
& + \left(\boldsymbol{u}^{(c)}\boldsymbol{D}^{\dagger}\boldsymbol{u}^{\dagger} - \boldsymbol{\alpha}\boldsymbol{u}^{(c)}\boldsymbol{u}^{\dagger}\right)_{k+N,\,j} \left(\boldsymbol{u}^{-1\dagger}\right)_{k,\,n-2N} B^{\dagger}_j \\
& + \left(\boldsymbol{u}^{(c)}\boldsymbol{D}^{\dagger}\boldsymbol{u}^{\dagger} - \boldsymbol{\alpha}\boldsymbol{u}^{(c)}\boldsymbol{u}^{\dagger}\right)_{k,\,j} \left(\boldsymbol{u}^{-1\dagger}\right)_{k+N,\,n-2N} B^{\dagger}_j \Bigg\}.
\end{aligned}$$

Now eq. (110) can be inserted,

$$\overline{S}_{12} + \overline{S}_{21} = \sum_{j,k=1}^{N} \left\{ \left[\beta_{k+N,\,j+N} \left(\boldsymbol{u}^{-1^\dagger} \right)_{k,\,n-2N} + \beta_{k,\,j+N} \left(\boldsymbol{u}^{-1^\dagger} \right)_{k+N,\,n-2N} \right] A_j^\dagger + \left[\beta_{k+N,\,j} \left(\boldsymbol{u}^{-1^\dagger} \right)_{k,\,n-2N} + \beta_{k,j} \left(\boldsymbol{u}^{-1^\dagger} \right)_{k+N,\,n-2N} \right] B_j^\dagger \right\} .$$

The symmetry of $\boldsymbol{\beta}$ is used to replace sectors of $\boldsymbol{\beta}$ with sectors of $-\boldsymbol{\beta}^\intercal$, eq. (156),

$$\overline{S}_{12} + \overline{S}_{21} = -\sum_{j=1}^{N} \left[\left(\boldsymbol{\beta u}^{-1^\dagger} \right)_{j,\,n-2N} A_j^\dagger + \left(\boldsymbol{\beta u}^{-1^\dagger} \right)_{j+N,\,n-2N} B_j^\dagger \right] . \tag{165}$$

The summation of eq. (164) and (165) yields

$$\overline{S}_{12} + \overline{S}_{21} + \overline{S}_{22} = -\sum_{j=1}^{N} \left[\left(\boldsymbol{\beta u}^{-1^\dagger} + \boldsymbol{\alpha u}^{(c)} \right)_{j,\,n-2N} A_j^\dagger + \left(\boldsymbol{\beta u}^{-1^\dagger} + \boldsymbol{\alpha u}^{(c)} \right)_{j+N,\,n-2N} B_j^\dagger \right] .$$

Making use of eq. (110) again, results in

$$\overline{S}_{12} + \overline{S}_{21} + \overline{S}_{22} = -\lambda_n \sum_{j=1}^{N} \left[u^{(c)}_{j,\,n-2N} A_j^\dagger + u^{(c)}_{j+N,\,n-2N} B_j^\dagger \right] . \tag{166}$$

The combination of eq. (162) and (166) to (158) yields

$$\begin{aligned} \overline{S} &= \overline{S}_{11} + \overline{S}_{12} + \overline{S}_{21} + \overline{S}_{22} \\ &= -\lambda_n \sum_{j=1}^{N} \left[\left(\boldsymbol{u}^{-1^\dagger} \right)_{j+N,\,n-2N} A_j + \left(\boldsymbol{u}^{-1^\dagger} \right)_{j,\,n-2N} B_j + u^{(c)}_{j,\,n-2N} A_j^\dagger + u^{(c)}_{j+N,\,n-2N} B_j^\dagger \right] \\ &= -\lambda_n \bar{f}_n , \end{aligned}$$

which is also identical to eq. (157). Thus it has been shown that the first K - relation is valid for any possible index n.

Calculation for $\boldsymbol{K}$

Analog to the previous calculations for $\overline{\boldsymbol{K}}$, the sum S is split with respect to i,

$$S = \overbrace{\sum_{i=1}^{2N} K_{mi} \lambda_i \bar{f}_i}^{=:\,S_1} + \overbrace{\sum_{i=2N+1}^{4N} K_{mi} \lambda_i \bar{f}_i}^{=:\,S_2} . \tag{167}$$

and then with respect to m, in order to allow for the insertion of the definitions of $\boldsymbol{K}$ and $\bar{\boldsymbol{f}}$, eq. (117) and (116). Then S_1 and S_2 can be evaluated.

1.) $m \in [1, 2N]$

The first summand S_1 yields

$$\begin{aligned} S_1 = -\sum_{j,k=1}^{N} \sum_{i=1}^{2N} \Big\{ & \left(\boldsymbol{u}^{-1}\boldsymbol{u}^{(c)}\boldsymbol{u}^{\dagger}\right)_{m,k} u_{j,i}\, \lambda_i \left(\boldsymbol{u}^{-1}\right)_{i,k+N} A_j^{\dagger} \\ & + \left(\boldsymbol{u}^{-1}\boldsymbol{u}^{(c)}\boldsymbol{u}^{\dagger}\right)_{m,k+N} u_{j,i}\, \lambda_i \left(\boldsymbol{u}^{-1}\right)_{i,k} A_j^{\dagger} \\ & + \left(\boldsymbol{u}^{-1}\boldsymbol{u}^{(c)}\boldsymbol{u}^{\dagger}\right)_{m,k} u_{j+N,i}\, \lambda_i \left(\boldsymbol{u}^{-1}\right)_{i,k+N} B_j^{\dagger} \\ & + \left(\boldsymbol{u}^{-1}\boldsymbol{u}^{(c)}\boldsymbol{u}^{\dagger}\right)_{m,k+N} u_{j+N,i}\, \lambda_i \left(\boldsymbol{u}^{-1}\right)_{i,k} B_j^{\dagger} \\ & + \left(\boldsymbol{u}^{-1}\right)_{m,k} u_{j,i}\, \lambda_i \left(\boldsymbol{u}^{-1}\boldsymbol{u}^{(c)}\boldsymbol{u}^{\dagger}\right)_{i,k+N} A_j^{\dagger} \\ & + \left(\boldsymbol{u}^{-1}\right)_{m,k+N} u_{j,i}\, \lambda_i \left(\boldsymbol{u}^{-1}\boldsymbol{u}^{(c)}\boldsymbol{u}^{\dagger}\right)_{i,k} A_j^{\dagger} \\ & + \left(\boldsymbol{u}^{-1}\right)_{m,k} u_{j+N,i}\, \lambda_i \left(\boldsymbol{u}^{-1}\boldsymbol{u}^{(c)}\boldsymbol{u}^{\dagger}\right)_{i,k+N} B_j^{\dagger} \\ & + \left(\boldsymbol{u}^{-1}\right)_{m,k+N} u_{j+N,i}\, \lambda_i \left(\boldsymbol{u}^{-1}\boldsymbol{u}^{(c)}\boldsymbol{u}^{\dagger}\right)_{i,k} B_j^{\dagger} \Big\} . \end{aligned}$$

Applying the eigenvalue equation (106) to S_1 results in

$$\begin{aligned} S_1 = -\sum_{j,k=1}^{N} \Bigg\{ & \left[\left(\boldsymbol{u}^{-1}\boldsymbol{u}^{(c)}\boldsymbol{u}^{\dagger}\right)_{m,k} \alpha_{j,k+N} + \left(\boldsymbol{u}^{-1}\boldsymbol{u}^{(c)}\boldsymbol{u}^{\dagger}\right)_{m,k+N} \alpha_{j,k} \right] A_j^{\dagger} \\ & + \left[\left(\boldsymbol{u}^{-1}\boldsymbol{u}^{(c)}\boldsymbol{u}^{\dagger}\right)_{m,k} \alpha_{j+N,k+N} + \left(\boldsymbol{u}^{-1}\boldsymbol{u}^{(c)}\boldsymbol{u}^{\dagger}\right)_{m,k+N} \alpha_{j+N,k} \right] B_j^{\dagger} \Bigg\} =: S_{11} \\ & + \Bigg\{ \left[\left(\boldsymbol{u}^{-1}\right)_{m,k} \left(\boldsymbol{\alpha}\boldsymbol{u}^{(c)}\boldsymbol{u}^{\dagger}\right)_{j,k+N} + \left(\boldsymbol{u}^{-1}\right)_{m,k+N} \left(\boldsymbol{\alpha}\boldsymbol{u}^{(c)}\boldsymbol{u}^{\dagger}\right)_{j,k} \right] A_j^{\dagger} \\ & + \left[\left(\boldsymbol{u}^{-1}\right)_{m,k} \left(\boldsymbol{\alpha}\boldsymbol{u}^{(c)}\boldsymbol{u}^{\dagger}\right)_{j+N,k+N} + \left(\boldsymbol{u}^{-1}\right)_{m,k+N} \left(\boldsymbol{\alpha}\boldsymbol{u}^{(c)}\boldsymbol{u}^{\dagger}\right)_{j+N,k} \right] B_j^{\dagger} \Bigg\} =: S_{12} \end{aligned} \tag{168}$$

Then the symmetries of $\boldsymbol{\alpha}$, eq. (156), are exploited to rewrite the first part,

$$\begin{aligned} S_{11} &= \sum_{j=1}^{N} \sum_{k=1}^{2N} \left[\left(\boldsymbol{u}^{-1}\boldsymbol{u}^{(c)}\boldsymbol{u}^{\dagger}\right)_{m,k} \left(\boldsymbol{\alpha}^{\dagger}\right)_{k,j+N} A_j^{\dagger} + \left(\boldsymbol{u}^{-1}\boldsymbol{u}^{(c)}\boldsymbol{u}^{\dagger}\right)_{m,k} \left(\boldsymbol{\alpha}^{\dagger}\right)_{k,j} B_j^{\dagger} \right] \\ &= \sum_{j=1}^{N} \left[\left(\boldsymbol{u}^{-1}\boldsymbol{u}^{(c)}\boldsymbol{u}^{\dagger}\boldsymbol{\alpha}^{\dagger}\right)_{m,j+N} A_j^{\dagger} + \left(\boldsymbol{u}^{-1}\boldsymbol{u}^{(c)}\boldsymbol{u}^{\dagger}\boldsymbol{\alpha}^{\dagger}\right)_{m,j} B_j^{\dagger} \right] . \end{aligned}$$

With the help of the eigenvalue eq. (107), followed by (110) and then (106) the coefficient matrix $\boldsymbol{u}^{-1}\boldsymbol{u}^{(c)}\boldsymbol{u}^{\dagger}\boldsymbol{\alpha}^{\dagger}$ is rewritten as

$$\begin{aligned} \boldsymbol{u}^{-1}\boldsymbol{u}^{(c)}\boldsymbol{u}^{\dagger}\boldsymbol{\alpha}^{\dagger} &= \boldsymbol{u}^{-1}\boldsymbol{u}^{(c)}\boldsymbol{D}^{\dagger}\boldsymbol{u}^{\dagger} \\ &= \boldsymbol{u}^{-1}\left(\boldsymbol{\alpha}\boldsymbol{u}^{(c)}\boldsymbol{u}^{\dagger} + \boldsymbol{\beta}\right) \\ &= \boldsymbol{u}^{-1}\boldsymbol{\alpha}\boldsymbol{u}^{(c)}\boldsymbol{u}^{\dagger} + \boldsymbol{u}^{-1}\boldsymbol{\beta} \\ &= \boldsymbol{D}\boldsymbol{u}^{-1}\boldsymbol{u}^{(c)}\boldsymbol{u}^{\dagger} + \boldsymbol{u}^{-1}\boldsymbol{\beta} . \end{aligned}$$

Inserting this result in the expression for S_{11} yields

$$\begin{aligned} S_{11} = \lambda_m \sum_{j=1}^{N} \Big[& \left(\boldsymbol{u}^{-1}\boldsymbol{u}^{(c)}\boldsymbol{u}^{\dagger}\right)_{m,\,j+N} A_j^{\dagger} + \left(\boldsymbol{u}^{-1}\boldsymbol{u}^{(c)}\boldsymbol{u}^{\dagger}\right)_{m,j} B_j^{\dagger} \\ & + \left(\boldsymbol{u}^{-1}\boldsymbol{\beta}\right)_{m,\,j+N} A_j^{\dagger} + \left(\boldsymbol{u}^{-1}\boldsymbol{\beta}\right)_{m,j} B_j^{\dagger} \Big]. \end{aligned} \tag{169}$$

The second summand has the following structure:

$$\begin{aligned} S_2 = \sum_{j,k=1}^{N} \sum_{i=2N+1}^{4N} \Big\{ & \left(\boldsymbol{u}^{-1}\right)_{m,k} \left(\boldsymbol{u}^{-1\dagger}\right)_{j+N,\,i-2N} \lambda_i \left(\boldsymbol{u}^{\dagger}\right)_{i-2N,\,k+N} A_j \\ & + \left(\boldsymbol{u}^{-1}\right)_{m,\,k+N} \left(\boldsymbol{u}^{-1\dagger}\right)_{j+N,\,i-2N} \lambda_i \left(\boldsymbol{u}^{\dagger}\right)_{i-2N,\,k} A_j \\ & + \left(\boldsymbol{u}^{-1}\right)_{m,k} \left(\boldsymbol{u}^{-1\dagger}\right)_{j,\,i-2N} \lambda_i \left(\boldsymbol{u}^{\dagger}\right)_{i-2N,\,k+N} B_j \\ & + \left(\boldsymbol{u}^{-1}\right)_{m,k+N} \left(\boldsymbol{u}^{-1\dagger}\right)_{j,\,i-2N} \lambda_i \left(\boldsymbol{u}^{\dagger}\right)_{i-2N,\,k} B_j \Big\} =: S_{21} \\ & + \left(\boldsymbol{u}^{-1}\right)_{m,k} u^{(c)}_{j,\,i-2N} \lambda_i \left(\boldsymbol{u}^{\dagger}\right)_{i-2N,\,k+N} A_j^{\dagger} \\ & + \left(\boldsymbol{u}^{-1}\right)_{m,\,k+N} u^{(c)}_{j,\,i-2N} \lambda_i \left(\boldsymbol{u}^{\dagger}\right)_{i-2N,\,k} A_j^{\dagger} \\ & + \left(\boldsymbol{u}^{-1}\right)_{m,k} u^{(c)}_{j+N,\,i-2N} \lambda_i \left(\boldsymbol{u}^{\dagger}\right)_{i-2N,\,k+N} B_j^{\dagger} \\ & + \left(\boldsymbol{u}^{-1}\right)_{m,\,k+N} u^{(c)}_{j+N,\,i-2N} \lambda_i \left(\boldsymbol{u}^{\dagger}\right)_{i-2N,\,k} B_j^{\dagger} \Big\} =: S_{22} \end{aligned} \tag{170}$$

In the first part eq. (107) is exploited,

$$\begin{aligned} S_{21} = \sum_{j,k=1}^{N} \Big\{ & \Big[\left(\boldsymbol{u}^{-1}\right)_{m,k} \left(\boldsymbol{\alpha}^{\dagger}\right)_{j+N,\,k+N} + \left(\boldsymbol{u}^{-1}\right)_{m,\,k+N} \left(\boldsymbol{\alpha}^{\dagger}\right)_{j+N,\,k} \Big] A_j \\ & + \Big[\left(\boldsymbol{u}^{-1}\right)_{m,k} \left(\boldsymbol{\alpha}^{\dagger}\right)_{j,\,k+N} + \left(\boldsymbol{u}^{-1}\right)_{m,k+N} \left(\boldsymbol{\alpha}^{\dagger}\right)_{j,k} \Big] B_j \Big\}, \end{aligned}$$

followed by the symmetries of $\boldsymbol{\alpha}$, eq. (156),

$$S_{21} = -\sum_{j=1}^{N} \sum_{k=1}^{2N} \Big[\left(\boldsymbol{u}^{-1}\right)_{m,k} \alpha_{k,\,j} A_j + \left(\boldsymbol{u}^{-1}\right)_{m,k} \alpha_{k,\,j+N} B_j \Big].$$

Using eq. (106) yields

$$S_{21} = -\lambda_m \sum_{j=1}^{N} \Big[\left(\boldsymbol{u}^{-1}\right)_{m,j} A_j + \left(\boldsymbol{u}^{-1}\right)_{m,\,j+N} B_j \Big]. \tag{171}$$

Combining the so far unconsidered parts in eq. (168) and (170) yields

$$\begin{aligned} S_{12}+S_{22} = \sum_{j,k=1}^{N} \Big\{ & \left(\boldsymbol{u}^{-1}\right)_{m,k} \left(\boldsymbol{u}^{(c)}\boldsymbol{D}^{\dagger}\boldsymbol{u}^{\dagger} - \boldsymbol{\alpha}\boldsymbol{u}^{(c)}\boldsymbol{u}^{\dagger}\right)_{j,\,k+N} A_j^{\dagger} \\ & + \left(\boldsymbol{u}^{-1}\right)_{m,\,k+N} \left(\boldsymbol{u}^{(c)}\boldsymbol{D}^{\dagger}\boldsymbol{u}^{\dagger} - \boldsymbol{\alpha}\boldsymbol{u}^{(c)}\boldsymbol{u}^{\dagger}\right)_{j,k} A_j^{\dagger} \\ & + \left(\boldsymbol{u}^{-1}\right)_{m,k} \left(\boldsymbol{u}^{(c)}\boldsymbol{D}^{\dagger}\boldsymbol{u}^{\dagger} - \boldsymbol{\alpha}\boldsymbol{u}^{(c)}\boldsymbol{u}^{\dagger}\right)_{j+N,\,k+N} B_j^{\dagger} \\ & + \left(\boldsymbol{u}^{-1}\right)_{m,\,k+N} \left(\boldsymbol{u}^{(c)}\boldsymbol{D}^{\dagger}\boldsymbol{u}^{\dagger} - \boldsymbol{\alpha}\boldsymbol{u}^{(c)}\boldsymbol{u}^{\dagger}\right)_{j+N,\,k} B_j^{\dagger} \Big\} . \end{aligned}$$

Then eq. (110) is used again,

$$\begin{aligned} S_{12}+S_{22} = \sum_{j,k=1}^{N} \Big\{ & \left[\left(\boldsymbol{u}^{-1}\right)_{m,k} \beta_{j,\,k+N} + \left(\boldsymbol{u}^{-1}\right)_{m,\,k+N} \beta_{j,k} \right] A_j^{\dagger} \\ & + \left[\left(\boldsymbol{u}^{-1}\right)_{m,k} \beta_{j+N,\,k+N} + \left(\boldsymbol{u}^{-1}\right)_{m,\,k+N} \beta_{j+N,\,k} \right] B_j^{\dagger} \Big\} . \end{aligned}$$

followed by the symmetries of $\boldsymbol{\beta}$, eq. (156),

$$\begin{aligned} S_{12}+S_{22} &= -\sum_{j=1}^{N} \sum_{k=1}^{2N} \left[\left(\boldsymbol{u}^{-1}\right)_{m,k} \beta_{k,\,j+N} A_j^{\dagger} + \left(\boldsymbol{u}^{-1}\right)_{m,k} \beta_{k,j} B_j^{\dagger} \right] \\ &= -\sum_{j=1}^{N} \left[\left(\boldsymbol{u}^{-1}\boldsymbol{\beta}\right)_{m,\,j+N} A_j^{\dagger} + \left(\boldsymbol{u}^{-1}\boldsymbol{\beta}\right)_{m,j} B_j^{\dagger} \right] . \end{aligned} \tag{172}$$

The sum of eq. (169) and (172) yields

$$S_{11}+S_{12}+S_{22} = \lambda_m \sum_{j=1}^{N} \left[\left(\boldsymbol{u}^{-1}\boldsymbol{u}^{(c)}\boldsymbol{u}^{\dagger}\right)_{m,\,j+N} A_j^{\dagger} + \left(\boldsymbol{u}^{-1}\boldsymbol{u}^{(c)}\boldsymbol{u}^{\dagger}\right)_{m,j} B_j^{\dagger} \right] . \tag{173}$$

The result is obtained by adding together eq. (171) and (173) to (167) and yields eq. (157),

$$\begin{aligned} S &= S_{11}+S_{12}+S_{21}+S_{22} \\ &= -\lambda_m \sum_{j=1}^{N} \left[\left(\boldsymbol{u}^{-1}\right)_{m,j} A_j + \left(\boldsymbol{u}^{-1}\right)_{m,\,j+N} B_j - \left(\boldsymbol{u}^{-1}\boldsymbol{u}^{(c)}\boldsymbol{u}^{\dagger}\right)_{m,\,j+N} A_j^{\dagger} - \left(\boldsymbol{u}^{-1}\boldsymbol{u}^{(c)}\boldsymbol{u}^{\dagger}\right)_{m,j} B_j^{\dagger} \right] \\ &= -\lambda_m f_m . \end{aligned}$$

2.) $m \in [2N+1, 4N]$

The first summand S_1 is given by

$$\begin{aligned} S_1 = \sum_{j,k=1}^{N} \sum_{i=1}^{2N} \Big\{ & \left(\boldsymbol{u}^\dagger\right)_{m-2N,\,k} u_{j,i}\, \lambda_i \left(\boldsymbol{u}^{-1}\right)_{i,\,k+N} A_j^\dagger \\ & + \left(\boldsymbol{u}^\dagger\right)_{m-2N,\,k+N} u_{j,i}\, \lambda_i \left(\boldsymbol{u}^{-1}\right)_{i,k} A_j^\dagger \\ & + \left(\boldsymbol{u}^\dagger\right)_{m-2N,\,k} u_{j+N,\,i}\, \lambda_i \left(\boldsymbol{u}^{-1}\right)_{i,\,k+N} B_j^\dagger \\ & + \left(\boldsymbol{u}^\dagger\right)_{m-2N,\,k+N} u_{j+N,\,i}\, \lambda_i \left(\boldsymbol{u}^{-1}\right)_{i,k} B_j^\dagger \Big\} . \end{aligned}$$

The sum over i is again executed by inserting the eigenvalue equation (106),

$$\begin{aligned} S_1 = \sum_{j,k=1}^{N} \Big\{ & \left[\left(\boldsymbol{u}^\dagger\right)_{m-2N,\,k} \alpha_{j,\,k+N} + \left(\boldsymbol{u}^\dagger\right)_{m-2N,\,k+N} \alpha_{j,k} \right] A_j^\dagger \\ & + \left[\left(\boldsymbol{u}^\dagger\right)_{m-2N,\,k} \alpha_{j+N,\,k+N} + \left(\boldsymbol{u}^\dagger\right)_{m-2N,\,k+N} \alpha_{j+N,\,k} \right] B_j^\dagger \Big\} . \end{aligned}$$

Now, the symmetries of $\boldsymbol{\alpha}$ are exploited again, eq. (156),

$$\begin{aligned} S_1 &= -\sum_{j=1}^{N} \sum_{k=1}^{2N} \left[\left(\boldsymbol{u}^\dagger\right)_{m-2N,\,k} \left(\boldsymbol{\alpha}^\dagger\right)_{k,\,j+N} A_j^\dagger + \left(\boldsymbol{u}^\dagger\right)_{m-2N,\,k} \left(\boldsymbol{\alpha}^\dagger\right)_{k,\,j} B_j^\dagger \right] \\ &= -\sum_{j=1}^{N} \left[\left(\boldsymbol{u}^\dagger \boldsymbol{\alpha}^\dagger\right)_{m-2N,\,j+N} A_j^\dagger + \left(\boldsymbol{u}^\dagger \boldsymbol{\alpha}^\dagger\right)_{m-2N,\,j} B_j^\dagger \right] \end{aligned}$$

Using eq. (107) yields,

$$\begin{aligned} S_1 &= -\lambda_m \sum_{j=1}^{N} \left[\left(\boldsymbol{u}^\dagger\right)_{m-2N,\,j+N} A_j^\dagger + \left(\boldsymbol{u}^\dagger\right)_{m-2N,\,j} B_j^\dagger \right] \\ &= -\lambda_m f_m \end{aligned} \tag{174}$$

The second summand is zero, since $\boldsymbol{K} = \boldsymbol{0}$ in the lower right sector,

$$S_2 = 0 . \tag{175}$$

The result for $m \in [2N+1, 4N]$ is obtained by combining eq. (174) with (175) to (167) and confirms eq. (157), as does the result for $m \in [1, 2N]$,

$$\begin{aligned} S &= S_1 + S_2 \\ &= -\lambda_m f_m . \end{aligned} \tag{176}$$

Thus the validity of both K - relations has been demonstrated.

7.3 Commutator of f and f' - operators with the Liouvillian

In this subsection the commutators of the quasiparticle operators f_n, $\bar{f}_n$, f'_n and $\bar{f}'_n$ with the Liouvillian are calculated for the normal and the generalized noninteracting system. The result is used to determine the dynamics and the steady state, sec. 4.2.1 and 4.3.
First, the Liouvillian is expressed through the f - operators, eq. (101). In the second and third row their anticommutation relations (114) or (117) are inserted and for the generalized system also the K - relations (157) are used. This yields:

$$\begin{aligned}
\left(\hat{L} - C\mathbb{1}\right)\bar{f}_n &= \sum_{i=1}^{2\kappa N} \lambda_i \bar{f}_i f_i \bar{f}_n & \left(\hat{L} - C\mathbb{1}\right) f_n &= \sum_{i=1}^{2\kappa N} \lambda_i \bar{f}_i f_i f_n \\
&= \lambda_n \bar{f}_n - \sum_{i=1}^{2\kappa N} \lambda_i \bar{f}_i \bar{f}_n f_i & &= -(\kappa - 1)\,\lambda_n f_n - \sum_{i=1}^{2\kappa N} \lambda_i \bar{f}_i f_n f_i \\
&= \kappa\lambda_n \bar{f}_n + \bar{f}_n \left(\hat{L} - C\mathbb{1}\right) & &= -\kappa\lambda_n f_n + f_n \left(\hat{L} - C\mathbb{1}\right) \\
\Rightarrow \left[\hat{L}, \bar{f}_n\right] &= \kappa\lambda_n \bar{f}_n & \Rightarrow \left[\hat{L}, f_n\right] &= -\kappa\lambda_n f_n
\end{aligned} \tag{177}$$

As before, $\kappa = 1$ for the normal system and $\kappa = 2$ for the generalized one. The commutators with the f' - operators can be directly derived from this result, by inserting their definition, see eq. (132).

$$\begin{aligned}
\left[\hat{L}, \bar{f}'_n\right] &= \begin{cases} \left[\hat{L}, \bar{f}_n\right] = \kappa\lambda_n \bar{f}_n\,, & \text{for } \Im\lambda_n < 0 \\ \left[\hat{L}, f_n\right] = -\kappa\lambda_n f_n\,, & \text{for } \Im\lambda_n > 0 \end{cases} & \left[\hat{L}, f'_n\right] &= \begin{cases} \left[\hat{L}, f_n\right] = -\kappa\lambda_n f_n\,, & \text{for } \Im\lambda_n < 0 \\ \left[\hat{L}, \bar{f}_n\right] = \kappa\lambda_n \bar{f}_n\,, & \text{for } \Im\lambda_n > 0 \end{cases} \\
&= \kappa\lambda'_n \bar{f}'_n & &= -\kappa\lambda'_n f'_n
\end{aligned} \tag{178}$$

Products of $\bar{f}'$ - operators

Now the result from eq. (178) will be generalized for products of $\bar{f}'$ - operators. This can be achieved by mathematical induction. The induction hypothesis is

$$\hat{L} \prod_{i=1}^{P} \bar{f}'_{n_i} = \kappa \left[\sum_{i=1}^{P} \lambda'_{n_i}\right] \prod_{i=1}^{P} \bar{f}'_{n_i} + \prod_{i=1}^{P} \bar{f}'_{n_i} \hat{L}\,, \tag{179}$$

where $\boldsymbol{n} = \{n_1, \ldots, n_P\}$ is a sequence of different indices from $\{1, \ldots, 2\kappa N\}$. From eq. (178) follows that the hypothesis is fulfilled for $P = 1$,

$$\hat{L}\bar{f}'_{n_1} = \kappa\lambda'_{n_1} \bar{f}'_{n_1} + \bar{f}'_{n_1} \hat{L}\,, \tag{180}$$

which makes $P = 1$ the induction basis.

The inductive step can be performed as follows,

$$\begin{aligned}
\hat{L}\prod_{i=1}^{P+1}\bar{f}'_{n_i} &= \hat{L}\prod_{i=1}^{P}\bar{f}'_{n_i}\bar{f}'_{n_{P+1}} \\
&= \kappa\left[\sum_{i=1}^{P}\lambda'_{n_i}\right]\prod_{i=1}^{P}\bar{f}'_{n_i}\bar{f}'_{n_{P+1}} + \prod_{i=1}^{P}\bar{f}'_{n_i}\hat{L}\bar{f}'_{n_{P+1}} \\
&= \kappa\left[\sum_{i=1}^{P}\lambda'_{n_i}\right]\prod_{i=1}^{P}\bar{f}'_{n_i}\bar{f}'_{n_{P+1}} + \prod_{i=1}^{P}\bar{f}'_{n_i}\left(\kappa\lambda'_{n_{P+1}}\bar{f}'_{n_{P+1}} + \bar{f}'_{n_{P+1}}\hat{L}\right) \\
&= \kappa\left[\sum_{i=1}^{P}\lambda'_{n_i}\right]\prod_{i=1}^{P+1}\bar{f}'_{n_i} + \kappa\lambda'_{n_{P+1}}\prod_{i=1}^{P+1}\bar{f}'_{n_i} + \prod_{i=1}^{P+1}\bar{f}'_{n_i}\hat{L} \\
&= \kappa\left[\sum_{i=1}^{P+1}\lambda'_{n_i}\right]\prod_{i=1}^{P+1}\bar{f}'_{n_i} + \prod_{i=1}^{P+1}\bar{f}'_{n_i}\hat{L}\,.
\end{aligned} \tag{181}$$

The hypothesis has been inserted in the second line for P particles and again in the third line for a single particle. The calculation gives exactly the hypothesis for $P+1$ instead of P. Therefore the validity of eq. (179) has been demonstrated.

7.4 Proof of $C' = 0$

In order to proof that the steady state is the f' - vacuum, it has to be shown that the constant associated with the Liouvillian in the f' - basis satisfies $C' = 0$, sec. 4.3.
C' is calculated from the constant C in the f - basis, which is modified by the eigenvalues of the Liouvillian, according to

$$C' = C + \sum_{n|\Im\lambda_n>0}\lambda_n = 0\,, \tag{182}$$

see eq. (133). The eigenvalues can be determined by diagonalizing the coefficient matrix of the Liouvillian $\boldsymbol{L}''$. For both, the normal and the generalized system, $\boldsymbol{L}''$ has the following structure,

$$\boldsymbol{L}'' = \begin{pmatrix}\boldsymbol{\alpha} & \boldsymbol{\beta}\\ \mathbf{0} & \boldsymbol{\alpha}^\dagger\end{pmatrix}. \tag{183}$$

The condition for determining its eigenvalues reads

$$\begin{aligned}
\det\left(\boldsymbol{L}'' - \lambda\mathbb{1}\right) &= \det\begin{pmatrix}\boldsymbol{\alpha} - \lambda\mathbb{1} & \boldsymbol{\beta}\\ \mathbf{0} & \boldsymbol{\alpha}^\dagger - \lambda\mathbb{1}\end{pmatrix} \\
&= \det\left(\boldsymbol{\alpha} - \lambda\mathbb{1}\right)\,\det\left(\boldsymbol{\alpha}^\dagger - \lambda\mathbb{1}\right) \\
&= 0\,.
\end{aligned} \tag{184}$$

The second row follows for a block upper (or lower) triangular matrix by using the Laplace formula for determinants. The eigenvalues of $\boldsymbol{L}''$ are thus given by the union of the eigenvalues of $\boldsymbol{\alpha}$ and those of $\boldsymbol{\alpha}^\dagger$, which are complex conjugated to each other, $\lambda^{(\alpha)}$ and $\lambda^{(\alpha)*}$. To determine the eigenvalues of the whole matrix, it is sufficient to calculate those of $\boldsymbol{\alpha}$ only. Therefore $\boldsymbol{\alpha}$ is

rewritten as the sum of two hermitian matrices, $\boldsymbol{\alpha}_1$ and $\boldsymbol{\alpha}_2$, according to

$$\begin{aligned} \boldsymbol{\alpha} &= \boldsymbol{\alpha}_1 + i\boldsymbol{\alpha}_2 \,, \\ \boldsymbol{\alpha}_1 &= \tfrac{1}{2}\left(\boldsymbol{\alpha} + \boldsymbol{\alpha}^\dagger\right) \,, \\ \boldsymbol{\alpha}_2 &= \tfrac{1}{2i}\left(\boldsymbol{\alpha} - \boldsymbol{\alpha}^\dagger\right) \,. \end{aligned} \tag{185}$$

If $\boldsymbol{\alpha}$ is given in this form, a theorem by A. Hirsch [32, 33] says that the real and imaginary part of its eigenvalues are bounded by the real eigenvalues of $\boldsymbol{\alpha}_1$ and $\boldsymbol{\alpha}_2$, respectively,

$$\begin{aligned} \Re \,\mathrm{ev}\,(\boldsymbol{\alpha}) &\in [\min \mathrm{ev}\,(\boldsymbol{\alpha}_1)\,, \max \mathrm{ev}\,(\boldsymbol{\alpha}_1)] \,, \\ \Im \,\mathrm{ev}\,(\boldsymbol{\alpha}) &\in [\min \mathrm{ev}\,(\boldsymbol{\alpha}_2)\,, \max \mathrm{ev}\,(\boldsymbol{\alpha}_2)] \,, \end{aligned} \tag{186}$$

where ev $(\cdot)$ denotes the eigenvalues of $(\cdot)$. This theorem can also be looked up in [34].

Normal system

The discussed quantities for the normal system follow by comparison of eq. (93) with (183),

$$\begin{aligned} \boldsymbol{\alpha} &= \boldsymbol{h} - i\,\boldsymbol{\Lambda} \,, \quad \boldsymbol{\alpha}_1 = \boldsymbol{h} \,, \quad \boldsymbol{\alpha}_2 = -\boldsymbol{\Lambda} \,, \\ \boldsymbol{\alpha}^\dagger &= \boldsymbol{h} + i\,\boldsymbol{\Lambda} \,. \end{aligned} \tag{187}$$

$\boldsymbol{\Lambda}$ is positive semidefinite, $\boldsymbol{v}^\dagger \boldsymbol{\Lambda} \boldsymbol{v} = \boldsymbol{v}^\dagger \boldsymbol{\Gamma}^{(+)} \boldsymbol{v} + \boldsymbol{v}^\dagger \boldsymbol{\Gamma}^{(-)\intercal} \boldsymbol{v} \geq 0 \;\; \forall \boldsymbol{v}$, because $\boldsymbol{\Gamma}^{(+)}$ and $\boldsymbol{\Gamma}^{(-)}$ are positive semidefinite, eq. (74), (75) and (80). This means that all ev $(\boldsymbol{\Lambda}) \geq 0$ and all ev $(\boldsymbol{\alpha}_2) \leq 0$. From the theorem by A. Hirsch, expressed in eq. (186), follows $\Im$ ev $(\boldsymbol{\alpha}) \leq 0$. Thus, all eigenvalues of $\boldsymbol{L''}$ with negative imaginary part belong to $\boldsymbol{\alpha}$ and all with positive imaginary part to $\boldsymbol{\alpha}^\dagger$. Therefore,

$$\sum_{n|\Im\lambda_n>0} \lambda_n = \mathrm{tr}\,\{\boldsymbol{\alpha}^\dagger\} = \mathrm{tr}\,\{\boldsymbol{h} + i\,\boldsymbol{\Lambda}\} \,. \tag{188}$$

The constant C was given by eq. (85),

$$C = -\,\mathrm{tr}\,\{\boldsymbol{h} + i\,\boldsymbol{\Lambda}\} \,, \tag{189}$$

Now C' can be determined from (182),

$$C' = -\,\mathrm{tr}\,\{\boldsymbol{h} + i\,\boldsymbol{\Lambda}\} + \mathrm{tr}\,\{\boldsymbol{h} + i\,\boldsymbol{\Lambda}\} = 0 \,. \tag{190}$$

Generalized system

In this case the discussed quantities are achieved by comparison of eq. (96) with (183),

$$\begin{aligned} \boldsymbol{\alpha} &= \begin{pmatrix} \frac{1}{2}\left(\boldsymbol{h} - i\,\boldsymbol{\Lambda}\right) & \boldsymbol{a}^\dagger \\ \boldsymbol{a} & -\frac{1}{2}\left(\boldsymbol{h} + i\,\boldsymbol{\Lambda}\right)^\intercal \end{pmatrix} \,, \quad \boldsymbol{\alpha}_1 = \tfrac{1}{2}\begin{pmatrix} \boldsymbol{h} & 2\boldsymbol{a}^\dagger \\ 2\boldsymbol{a} & -\boldsymbol{h}^\intercal \end{pmatrix} \,, \quad \boldsymbol{\alpha}_2 = -\tfrac{1}{2}\begin{pmatrix} \boldsymbol{\Lambda} & \boldsymbol{0} \\ \boldsymbol{0} & \boldsymbol{\Lambda}^\intercal \end{pmatrix} \,, \\ \boldsymbol{\alpha}^\dagger &= \begin{pmatrix} \frac{1}{2}\left(\boldsymbol{h} + i\,\boldsymbol{\Lambda}\right) & \boldsymbol{a}^\dagger \\ \boldsymbol{a} & -\frac{1}{2}\left(\boldsymbol{h} - i\,\boldsymbol{\Lambda}\right)^\intercal \end{pmatrix} \,. \end{aligned} \tag{191}$$

Since $\boldsymbol{\alpha}_2$ is block diagonal, its eigenvalues are equivalent to the union of the eigenvalues of the two diagonal blocks. As discussed above, $\boldsymbol{\Lambda}$ has positive eigenvalues only. Due to the minus

sign, all ev $(\boldsymbol{\alpha}_2) \leq 0$. From the theorem by A. Hirsch again follows with eq. (186) that all $\Im$ ev $(\boldsymbol{\alpha}) \leq 0$. Therefore one gets the same result as above, that $\boldsymbol{\alpha}$ is exclusively responsible for the eigenvalues in $\boldsymbol{L}''$ with negative imaginary part.

$$\sum_{n|\Im\lambda_n>0} \lambda_n = \text{tr } \{\boldsymbol{\alpha}^\dagger\} = \tfrac{1}{2} \text{ tr } \{\boldsymbol{h} + i\,\boldsymbol{\Lambda}\} - \tfrac{1}{2} \text{ tr } \{\boldsymbol{h} - i\,\boldsymbol{\Lambda}\} = i \text{ tr } \{\boldsymbol{\Lambda}\} \tag{192}$$

The linearity of the trace has been used and that tr $\{\boldsymbol{M}^\intercal\}$ = tr $\{\boldsymbol{M}\}$ for a matrix $\boldsymbol{M}$. The former constant C was given by eq. (88),

$$C = -i \text{ tr } \{\boldsymbol{\Lambda}\}\,, \tag{193}$$

Inserting this in eq. (182) yields the new constant,

$$C' = -i \text{ tr } \{\boldsymbol{\Lambda}\} + i \text{ tr } \{\boldsymbol{\Lambda}\} = 0\,. \tag{194}$$

If, in addition to $C' = 0$, states with one or more f' particles decay to zero with increasing time, the steady state is equivalent to the f' vacuum, $|0_{f'}\rangle$. This is shown in sec. 4.3 and 7.5.

7.5 Decay of states with one or more f' particles

In order to proof that the steady state is the f' vacuum, it is essential to show that no state with one or more f' particles survives in the long time limit $t \to \infty$. This is done in the following. A state that results from the application of an operator to the f' vacuum evolves in time as

$$\begin{aligned} i\frac{d}{dt}\hat{O}\,|0_{f'}\rangle &= \hat{L}\hat{O}\,|0_{f'}\rangle \\ &= \left[\hat{L}\,,\hat{O}\right]|0_{f'}\rangle\ . \end{aligned} \tag{195}$$

The second row is valid, because $\hat{L}\,|0_{f'}\rangle = 0$. This follows from the f' representation of $\hat{L}$, eq. (133), with $C' = 0$, see subsec. 7.4. For a state hosting one or more f' particles eq. (195) becomes

$$i\frac{d}{dt}\,|\psi\rangle = \lambda_\psi\,|\psi\rangle\ , \qquad \begin{aligned} |\psi\rangle &= \prod_{i=1}^{P} \bar{f}'_{n_i}\,|0_{f'}\rangle\ , \\ \lambda_\psi &= \kappa \sum_{i=1}^{P} \lambda'_{n_i}\ , \end{aligned} \tag{196}$$

where $\boldsymbol{n} = \{n_1, \ldots, n_P\}$ is a sequence of different indices from $\{1, \ldots, 2\kappa N\}$. P is the number of f' particles in $|\psi\rangle$. This result is obtained from eq. (195), using the previously evaluated commutator, eq. (179). Eq. (196) is easily integrated,

$$\begin{aligned} |\psi\rangle_t &= \exp\left[-i\lambda_\psi t\right]|\psi\rangle_0 \\ &= \exp\left[-i\,\Re\lambda_\psi t\right]\exp\left[\Im\lambda_\psi t\right]|\psi\rangle_0 \\ &\underset{t\to\infty}{\to} 0\,. \end{aligned} \tag{197}$$

The amplitude goes exponentially to zero for $t \to \infty$, because $\Im\lambda_\psi < 0$, since per definition $\Im\lambda'_{n_i} < 0$. This exponential decay also holds for linear combinations of states $|\psi\rangle$, since the differential equation is linear and homogeneous. (In sec 7.5 it has been assumed that the Liouville matrix has constant coefficients.)

References

[1] K. v. Klitzing, G. Dorda, and M. Pepper, "New Method for High-Accuracy Determination of the Fine-Structure Constant Based on Quantized Hall Resistance," *Phys. Rev. Lett.* **45** (1980) 494–497.

[2] D. J. Thouless, M. Kohmoto, M. P. Nightingale, and M. den Nijs, "Quantized Hall Conductance in a Two-Dimensional Periodic Potential," *Phys. Rev. Lett.* **49** (1982) 405–408.

[3] C. L. Kane and E. J. Mele, "Quantum Spin Hall Effect in Graphene," *Phys. Rev. Lett.* **95** (2005) 226801.

[4] M. König, S. Wiedmann, C. Brüne, A. Roth, H. Buhmann, L. W. Molenkamp, X.-L. Qi, and S.-C. Zhang, "Quantum Spin Hall Insulator State in HgTe Quantum Wells," *Science* **318** (2007) 766–770.

[5] H. Zhang, C.-X. Liu, X.-L. Qi, X. Dai, Z. Fang, and S.-C. Zhang, "Topological insulators in Bi_2Se_3, Bi_2Te_3 and Sb_2Te_3 with a single Dirac cone on the surface," *Nat. Phys.* **5** (2009) 438–442.

[6] E. Majorana, "Teoria simmetrica dell'elettrone e del positrone," *Il Nuovo Cimento (1924-1942)* **14** (1937) 171–184.

[7] A. Stern, "Non-Abelian states of matter," *Nature* **464** (2010) 187–193.

[8] H.-P. Breuer and F. Petruccione, *The Theory of Open Quantum Systems*. Oxford University Press, 2002.

[9] A. A. Dzhioev and D. S. Kosov, "Super-fermion representation of quantum kinetic equations for the electron transport problem," *J. Chem. Phys.* **134** (2011) 044121.

[10] A. Dorda, M. Nuss, W. von der Linden, and E. Arrigoni, "Auxiliary master equation approach to non-equilibrium correlated impurities," *Phys. Rev. B* **89** (2014) 165105.

[11] W. P. Su, J. R. Schrieffer, and A. J. Heeger, "Solitons in polyacetylene," *Phys. Rev. Lett.* **42** (1979) 1698–1701.

[12] S.-Q. Shen, *Topological Insulators: Dirac Equation in Condensed Matters*, vol. 174 of *Springer Series in Solid-State Sciences*. Springer-Verlag Berlin Heidelberg, 2012.

[13] M. Franz and L. Molenkamp, *Topological Insulators*, vol. 6 of *Contemporary Concepts of Condensed Matter Science*. Elsevier Science, 2013.

[14] A. Bernevig and T. Neupert, "Topological Superconductors and Category Theory," *ArXiv e-prints* (2015) , arXiv:1506.05805 [cond-mat.str-el].

[15] J. K. Asbóth, L. Oroszlány, and A. Pályi, "A Short Course on Topological Insulators:

Band-structure topology and edge states in one and two dimensions," *ArXiv e-prints* (2015) , arXiv:1509.02295 [cond-mat.mes-hall].

[16] J. Alicea, "New directions in the pursuit of Majorana fermions in solid state systems," *Reports on Progress in Physics* **75** (2012) 076501.

[17] A. Y. Kitaev, "Unpaired Majorana fermions in quantum wires," *Physics-Uspekhi* **44** (2001) 131.

[18] S. Huber, "Topological quantum numbers in condensed matter systems," (2015) . https://cmt-qo.phys.ethz.ch/wp-content/uploads/teaching/tqn/lectures/05.pdf.

[19] F. Wilczek, "Majorana returns," *Nature Physics* **5** (2009) 614–618.

[20] M. Leijnse and K. Flensberg, "Introduction to topological superconductivity and Majorana fermions," *Semiconductor Science and Technology* **27** (2012) 124003.

[21] Y. Oreg, G. Refael, and F. von Oppen, "Helical Liquids and Majorana Bound States in Quantum Wires," *Phys. Rev. Lett.* **105** (2010) 177002.

[22] R. M. Lutchyn, J. D. Sau, and S. Das Sarma, "Majorana Fermions and a Topological Phase Transition in Semiconductor-Superconductor Heterostructures," *Phys. Rev. Lett.* **105** (2010) 077001.

[23] P. G. de Gennes, "Boundary effects in superconductors," *Rev. Mod. Phys.* **36** (1964) 225–237.

[24] Y.-J. Doh, J. A. van Dam, A. L. Roest, E. P. A. M. Bakkers, L. P. Kouwenhoven, and S. De Franceschi, "Tunable supercurrent through semiconductor nanowires," *Science* **309** (2005) 272–275.

[25] J. A. van Dam, Y. V. Nazarov, E. P. A. M. Bakkers, S. De Franceschi, and L. P. Kouwenhoven, "Supercurrent reversal in quantum dots," *Nature* **442** (2006) 667–670.

[26] P. San-Jose, J. L. Lado, R. Aguado, F. Guinea, and J. Fernández-Rossier, "Majorana Zero Modes in Graphene," *Phys. Rev. X* **5** (2015) 041042.

[27] D. Roy, C. J. Bolech, and N. Shah, "Majorana fermions in a topological superconducting wire out of equilibrium: Exact microscopic transport analysis of a *p*-wave open chain coupled to normal leads," *Phys. Rev. B* **86** (2012) 094503.

[28] G. Baym and L. P. Kadanoff, "Conservation laws and correlation functions," *Phys. Rev.* **124** (1961) 287–299.

[29] E. A. Yuzbashyan, M. Dzero, V. Gurarie, and M. S. Foster, "Quantum quench phase diagrams of an *s*-wave BCS-BEC condensate," *Phys. Rev. A* **91** (2015) 033628.

[30] E. Arrigoni, M. Knap, and W. von der Linden, "Nonequilibrium Dynamical Mean-Field

Theory: An Auxiliary Quantum Master Equation Approach," *Phys. Rev. Lett.* **110** (2013) 086403.

[31] A. Dorda, M. Ganahl, H. G. Evertz, W. von der Linden, and E. Arrigoni, "Auxiliary master equation approach within matrix product states: Spectral properties of the nonequilibrium Anderson impurity model," *Phys. Rev. B* **92** (2015) 125145.

[32] A. Hirsch, "Sur les racines d'une équation fondamentale," *Acta Math.* **25** (1902) 367–370.

[33] O. Toeplitz, "Das algebraische Analogon zu einem Satze von Fejér," *Mathematische Zeitschrift* **2** (1918) 187–197.

[34] M. Deuring and G. Köthe, *Enzyklopädie der Mathematischen Wissenschaften mit Einschluss Ihrer Anwendungen: Band I: Algebra und Zahlentheorie*. Vieweg+Teubner Verlag, 2013.